Picosecond Spin Seebeck Effect in Magnetic Insulators

UNIVERSITY OF CAMBRIDGE

Farhan Nur Kholid

Downing College

This dissertation is submitted for the degree of Doctor of Philosophy

October, 2020

Declaration

I hereby declare that this dissertation is the result of my own work and includes nothing which is the outcome of work done in collaboration except as declared in the acknowledgement and specified in the text. It is not substantially the same as any work that has already been submitted before for any degree or other qualification at the University of Cambridge or any other institution. Moreover, it does not exceed the prescribed word limit of 60,000 words including abstract and appendices.

Farhan Nur Kholid

October 2020

Acknowledgement

I would like to express my utmost gratitude to the people whom without them this work would not be possible.

I would like to first thank my PhD supervisor, Chiara Ciccarelli. I am thankful for the opportunity of being your first PhD student. It was invaluable experience to get involved in starting-up a new lab. The technical and transferable skills that I have gained will benefit me for years to come. Thank you for trusting me on many occasions whether about the THz setup building or the spintronics projects. I am extremely grateful for your mentorship and support on my research and future careers. I would like to offer special thanks to Dominik Hamara. It was a great pleasure to work with you in the last 3 years. I am thankful to you for being an amazing team player. I really appreciate the comfortable and peaceful life in the lab. And thank you for proofreading this thesis. I wish you all the best for your final year.

I feel privileged to receive immense support from the staffs in Cavendish Laboratory. I am greatly indebted to Roger Beadle and Tom Sharp for their contributions in many aspects of setting up the lab, from assembling the optical table, cryostat support, the enclosure box to vacuum pumps. It has also been a great pleasure to have a chat in with you. Construction of a cryostat lifting system has been made possible by Cavendish workshop staffs, Gary Large, Chris Burling, Ollie Noris. They created the optimised design and fabricated the custom-made components to meet specific requirements of our cryostat. Procuring the optical lab components required numerous purchases, and Kapitza Hub staffs, Egle Bunkute, Jennie Nelson, and William Mortimer, have made the process straightforward and have always been helpful to my inquiries. I would like to thank Adam Brown, Cheng Liu, Alan Turner, Huw Prytherch and Jack Graham for continuous support for maintaining the lab.

I thank all collaborators who have made this work possible. Colleagues in Radboud University Nijmegen, Prof. Dr. Alexey Kimel, Guanqiao Li, Dr. Rostislav Mikhaylovskiy, Dr. Sergei Semin, and Toni Tonnen, were very welcoming and provided thorough training during my 4-months visit to learn about THz spectroscopy. I would like to thank Dr. Davide Bossini from T.U. Dortmund for numerous discussions about the materials that I studied and thoughtful feedback on the picosecond

Abstract

The spin Seebeck effect (SSE) refers to spin current generation in a magnetic insulator/non-magnetic metal heterostructure due to a thermal gradient and most SSE experiments typically use an electric current as heat source. This study uses Terahertz (THz) time-domain emission spectroscopy where a femtosecond laser induces a thermal gradient that lasts for only a few picoseconds and the SSE signal manifests as broadband THz electric field radiation. The ultra-fast laser excitation and detection technique enable focusing the analysis on the interfacial contributions of the SSE, minimising contributions from the bulk magnet which dominate instead in the electronic measurements.

The first part of the thesis (Chapter 3) discusses the steps and calibration procedures involved in building the THz emission spectroscopy setup. We describe the process of optimising the setup sensitivity, aiming at reaching the same performance allowed in the THz setups present in other groups, and discuss potential improvements.

The second part of this thesis describes measurements of the picosecond SSE in different magnetic states: ferrimagnetic, antiferromagnetic, and paramagnetic. Probing the picosecond SSE in well-studied ferrimagnetic YIG at low temperatures (Chapter 4) points out key differences with respect to previous electrical measurements done at low frequency. Comparing two antiferromagnets from the same magnetic class but with very different values of the antiferromagnetic resonance frequencies (Chapter 5 and Chapter 6) provides insights on the role of magnon energy dispersion in determining the efficiency of interfacial spin transport. Measuring the picosecond SSE in an antiferromagnet with magnetic transition temperature at 117 K allows a comparison of the spin emission in the ordered and paramagnetic phase (Chapter 6). Finally, we observe extremely strong SSE signals from the antiferromagnets despite the low field-induced magnetic moment and we attribute this to strong interfacial exchange coupling and high-frequency spin susceptibility.

iv

Contents

Chapter 1

Introduction

Electrons as spin carriers provide means to connect magnetism with electronics. The earliest works date back in the 1970s where the tunneling of a spin-polarised current was observed in Fe-Ge-Co junctions [1]. Breakthroughs were accomplished in the 1980s with the demonstration of a spin current injection across a ferromagnetic metal(FM)/non-magnetic metal (NM) interface [2], and the subsequent discovery of the giant magnetoresistance (GMR) [3]. The discovery of GMR lead to an unprecedented leap forward in memory technologies, allowing the development of magnetic read heads that exceeded by several orders of magnitude in sensitivity the previous readout based on anisotropic magnetoresistance [4–6]. This technological application-oriented research field was named spintronics.

Since the discovery of GMR, magnetic multilayers have been the playground for a multitude of exciting studies. Among these are highly sensitive tunneling magnetoresistance [7–12], interlayer exchange coupling [13–16], and spin-transfer torque [17,18]. The key technological selling point of spintronics lies in its potentials in creating non-volatile magnetic data storage that is more energy friendly and operates faster [19]. In a magnetic bit, binary data is usually represented by opposite magnetisation directions. The core mission of spintronic research revolves around understanding the fundamental physics of the interactions between electrons and spins, and how this can be used to control and read a magnetic state electrically.

The early magnetic memory devices used Oersted fields for magnetisation switching [20,21]. However, the stray magnetic fields can influence the neighbouring magnetic bits if they are too close, imposing a limit for device miniaturisation [19]. A different approach emerged in the late 1990s based on predictions by Slonczewski

[22] and Berger [23] of magnetisation switching by spin-polarised electric currents. Electrons can exert torques to a magnetic layer when flowing inside it if the current is spin-polarised orthogonal with respect to the magnetisation direction. Depending on the electric current density and the geometry, the torque can result in magnetisation switching [24, 25], or self-sustained magnetic oscillations [26]. A spin transfer torque (STT) device requires a magnetic layer, often called a fixed layer, that polarises the applied unpolarised electric current before entering the magnetic memory layer, or free layer. Both Oersted-field and STT-based magnetic memories have been successfully commercialised with the latest 1 GB MRAM by Everspin technologies.

Two decades ago, it was predicted [27, 28] and experimentally demonstrated that a pure spin current [29, 30], the flow of angular momentum without an associated flow of charge, can be generated in non-magnetic semiconductors or metals. This effect, named spin-Hall effect (SHE), occurs when spin-orbit scatterings deflect electrons in two opposing directions depending on their spin direction, which results in a tangential pure spin current [31]. The spin accumulation at the boundary can flow and exert a spin torque to an adjacent ferromagnet. The reciprocal effect, the inverse SHE (ISHE) converts a pure spin current into an electrical signal. The same spin-orbit scatterings acting on a flow of angular momentum result in a flow of electron charges in the transverse direction [32]. Soon after these discoveries, SHE and ISHE have become established tools for generation and detection of spin currents. SHE-based spin-torque devices would offer significant improvements including the absence of charge flow in the ferromagnet [33, 34], prolonging devices lifetime and allowing design simplification. ISHE has enabled obtaining electric current signal from a pure spin current and assisted the advancement of research pertinent to spin current generation [35, 36].

There are other means of spin current injection that do not require applying an electric current, which opened the way to the use of ferromagnetic insulators (FI). Spin pumping describes the coherent generation of a pure spin current due to microwave excitations [37–40]. As the magnetic field component of the microwave electromagnetic field resonantly drives spin precession in a ferromagnet, a spin current flows to an adjacent NM as the consequence of angular momentum conservation [38]. An incoherent spin current can also be generated by a thermal gradient and is referred to as spin Seebeck effect [41].

The majority of research in spintronics has focused to date on studies

carried in GHz frequency range, as the timescales of ferromagnetic magnetisation switching (in the nanoseconds) were considered as the main factor limiting the speed [19]. The stronger interactions, such as the exchange interactions and spin-orbit interactions, occur however at much faster time scales down to 10^{-15} - 10^{-12} s and the development of femtosecond lasers has enabled studying spin effects at timescales comparable with those fundamental interactions [42]. The central question is whether using light pulses can excite dynamics and magnetisation switching surpassing the GHz range. In this respect, there have been growing interests in using antiferromagnets to replace ferromagnets [43]. Antiferromagnets have much faster magnetic resonances in the THz range [44–47], are insensitive to stray fields, and are abundant in nature [48]. And yet, traditionally antiferromagnets have only been used to harden the coercivity or pin a ferromagnet via the exchange bias [49]. Femtosecond spectroscopy techniques allow now studying these materials with sufficient time resolution to resolve their spin dynamics [48].

The pioneering work on femtosecond magnetism emerged in 1996, showing that a femtosecond near-infrared pulse can induce demagnetisation in Nickel in less than 1 ps [50]. Numerous experiments on various laser-induced magnetic phenomena were subsequently reported, for example the observations of spin reorientation [51], all-optical magnetic switching [52–55], optical excitation of antiferromagnetic precession modes [56–58], and modification of exchange interactions [59, 60]. Aside from spin-spin interaction, ultrafast magnetism is explained with the energy and angular momentum transfer between electrons, phonons, and magnons [50, 61]. It is also essential to incorporate the resulting spin current that follows from the rapid demagnetisation of a metallic ferromagnet [62, 63].

Terahertz time-domain spectroscopy is among the ideal techniques for probing ultrafast spintronic transports, spin-orbit interactions, and antiferromagnetic resonance modes. Many THz spintronics experiments in the last decade use common magnetic structures in GHz spintronic studies but measure in faster time scales, for example the GMR [64] and anomalous-Hall effects [65]. The magnetic field component of an intense THz pulse can resonantly excite magnetic resonance modes in compensated antiferromagnets [58, 66] and canted-antiferromagnetic orthoferrites [67–69]. Spin current generation via ultrafast spin (dependent) Seebeck effect + ISHE have also been recently demonstrated in typical FM/NM [70, 71] and insulating ferrimagnet YIG/Pt [72] at room temperature and higher, respectively.

This PhD thesis aims to expand the understanding of the spin Seebeck effect (SSE) by performing THz emission experiments at low temperature and for various magnetic orderings: ferrimagnetic, antiferromagnetic, and paramagnetic. The ultrafast excitation and detection enable us to restrict the phenomenology to interface contribution differently from previous DC studies where bulk effects play an important role [73, 74].

Chapter 2 provides a background on the relevant physics, including the fundamentals of terahertz spectroscopy, ultrafast optical excitations in materials, interactions between electrons, phonons, and magnons, spintronics, and theoretical models of the spin Seebeck effects. In Chapter 3, we describe the designing and building of our THz time domain spectroscopy set-up. In Chapter 4, we present measurements of the picosecond SSE in YIG/Pt, showing a significant difference with respect to previous electrical studies. Chapter 5 shows measurements of the picosecond SSE in antiferromagnetic $KNiF_3$/Pt. In Chapter 6, measurements of the picosecond SSE in antiferromagnetic $KCoF_3$/Pt displays stark differences with respect to $KNiF_3$/Pt, which allows us to point to antiferromagnetic magnon dispersion.

Chapter 2

Background

This chapter provides the fundamental concepts relevant to the experimental studies presented in this thesis. Section 2.1 briefly deals with the basics of femtosecond laser pulses and THz spectroscopy, which include coherent excitation of THz emission in dielectrics as well as its inverse mechanism useful for THz time-domain detection. It is followed by descriptions of ultrafast optical excitations in metals and the subsequent energy relaxations, which involve the interplay between itinerant electron, lattice, and spin systems. Section 2.5 outlines the fundamentals of the spin Hall effects, the key mechanisms enabling probing spin currents via Terahertz emission spectroscopy. At the end of the chapter we describe the macroscopic model of magnetism and spintronics, covering mathematical treatments of macroscopic magnetisation dynamics in bulk ferromagnets and antiferromagnets, spin pumping and spin Seebeck effect.

2.1 Terahertz spectroscopy fundamentals

Femtosecond laser A laser is a device that emits coherent light due to a process called stimulated emission. The device mainly consists of a gain medium inside a cavity. An external energy source (voltage source or another laser) is applied to the gain medium such that one of its electronic states is excited. These electrons can spontaneously decay back to the lower energy state and emit photons, and this process is called spontaneous emission [75]. When these photons bounce back within the cavity and are absorbed by the gain medium, they can trigger stimulated photon emission that is coherent with the initial photons. If the gain medium is in a

population inversion state where the population of excited electrons is higher than the ground state electrons, a net number of emitted photons is achieved [76].

To generate ultrashort light pulses, the gain medium must have broad gain bandwidth and the cavity must be sufficiently long [77]. For instance, a common femtosecond laser uses a Ti-doped sapphire crystal as the gain medium, which has a bandwidth of 128 THz between 770 nm and 830 nm, and the cavity length is typically of the order of tens of cm. This long cavity allows multiple resonant modes with spacing of $\Delta v = c/2L$, L is the cavity length. Therefore, within the gain bandwidth, there are hundred thousand modes allowed. If all these modes have fixed phases between each other, or are coherent, their superposition in time domain results in a burst of light with a pulse width Δt that depends on the number of modes N allowed in the gain bandwidth, $\Delta t = \frac{0.441}{N\Delta v}$. Such a state is called mode-locking, and can be achieved by using an electro-optic modulator (active mode-locking) or using passive means such as saturable absorber or Kerr lens [77]. These methods selectively enhance the modes relevant for the light pulse while rejecting the weak modes.

2nd **order electric polarisation** Nonlinear optics is pertinent to nonlinear responses of the electric polarisation or bound charges of a matter to the electric field component of light.

$$\mathbf{P} = \varepsilon_0 \left[\chi^{(1)}\mathbf{E} + \chi^{(2)}_{ij}\mathbf{E_i}\mathbf{E_j} + \chi^{(3)}_{klm}\mathbf{E_k}\mathbf{E_l}\mathbf{E_m} + ... \right] \tag{2.1}$$

$\mathbf{P}$ is the electric polarisation, E_a is the electric field with polarisation along the a axis of the material, $\chi^{(n)}$ is the nth order of electric susceptibility. A plethora of nonlinear phenomena emerge from the higher order effects, which are significant only with intense electric field sources typically achieved by laser pulses. This section focuses on the 2nd order effects.

$$\mathbf{P} = \varepsilon_0 \chi^{(2)}_{ij}(\omega_1, \omega_2)\mathbf{E_i}(\omega_1)\,\mathbf{E_j}(\omega_2) \tag{2.2}$$

In this order, there are a number of nonlinear optics that can emerge depending on the permutations of the input frequencies [78]. For example, two electric fields with frequency ω_1 and ω_2 can result in an output with frequency of $\omega_1 + \omega_2$ or $\omega_1 - \omega_2$, and these two processes are called summation and difference
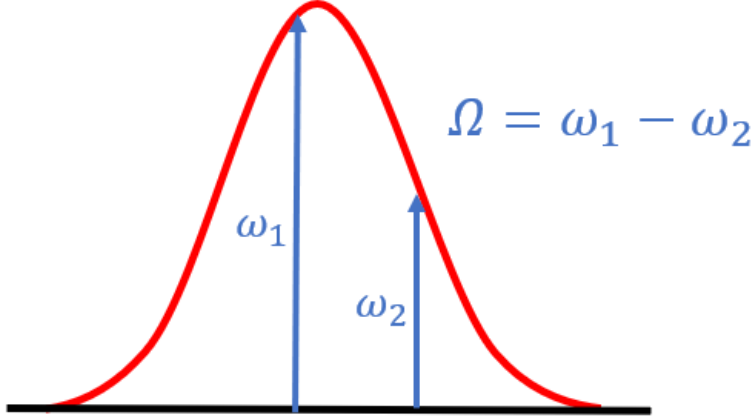
Figure 2.1: An illustration of difference frequency generation within a femtosecond pulse which results in a broadband Terahertz pulse

frequency generation, SFG and DFG, respectively. $\omega_1 = \omega_2$ means that the input can be a single laser pulse and the output frequency is doubled from the input frequency; therefore, the process is named as second harmonic generation (SHG). Whereas the DFG now has zero frequency, and is often named as optical rectification.

2.1.1 Optical rectification

The intense and varying electric field magnitude of femtosecond pulses enable 2nd order optical rectification that results in a dynamical response of the bound charges. In time-domain, the process can be intuitively understood as the asymmetric response of bound charges to two opposing polarities of electric field oscillations, leading to non-zero bound charges rectifying the oscillating electric field [79]. For an intense laser pulse input, the rapid change of the electric-field magnitude leads to a dynamic bound charges response that correlates with the envelope function of the laser pulse. As a consequence of Maxwell's equations, an electric field pulse is emitted.

$$\frac{\partial^2 \mathbf{E_{THz}}}{\partial x^2} - \frac{n^2}{c^2}\frac{\partial^2 \mathbf{E_{THz}}}{\partial t^2} = \mu_0 \frac{\partial^2 \mathbf{P_{OR}}}{\partial t^2} \tag{2.3}$$

$$\mathbf{P_{OR}} = \varepsilon_0 \int_{\omega_0 - \Delta\omega/2}^{\omega_0 + \Delta\omega/2} \chi_{ij}^{(2)}(-\Omega; \omega + \Omega; -\omega) \, \mathbf{E_i}(\omega)\mathbf{E_j}^*(\omega + \Omega)d\omega \tag{2.4}$$

n is the refractive index, c is the speed of light, μ_0 is the permeability constant [80]. In frequency domain, a 50 fs pulse has a bandwidth of 20 THz. All possible permutations of DFG that can be satisfied within this laser bandwidth contribute to a broadband THz electric field emission. The mechanism above is interchangeably referred to as 2nd order intra-pulse DFG or optical rectification.

For a dielectric crystal to emit a strong THz pulse via optical rectification, it must possess bulk inversion asymmetry, for example, Zinc-blende structure crystals such as ZnTe, and GaP, or BBO. However, there are more criteria than the non-zero $\chi^{(2)}$. The THz generation needs to be accumulated throughout the thickness of the crystal and hence the THz emission should ideally constructively interfere at any point within the crystal. The condition is fulfilled if the THz propagation velocity matches with the group velocity of the laser pulse, which is called phase matching [78].

$$\Delta k(\Omega) = k(\Omega) + k(\omega_0) - k(\omega_0 + \Omega) \approx k(\Omega) - \Omega\frac{dk}{d\omega} = \frac{\Omega}{c}[n(\Omega) - n_g(\omega_0)] \qquad (2.5)$$

k is the wave vector for a particular frequency, Ω is the THz emission frequency, ω_0 is the central frequency of the femtosecond optical pulse, c is the speed of light, n is the refractive index, n_g is the group refractive index of the optical pulse. Δk describes the phase mismatch between the optical pump pulse and the THz pulse. In most cases, only one optical wavelength satisfies this condition. Moreover, velocity dispersion always occurs in the THz range and hence the process is not equally efficient across the THz spectrum. Another sources of efficiency reduction are higher order photon absorption processes (i.e. two-photon or three-photon absorption) which can be significant for femtosecond optical pulses with the extremely high peak power $\sim 10^{12}$ W/cm^2 [81]. Lastly, the generated THz can be absorbed by the phonon modes of the crystal itself, which limits the THz bandwidth [81].

2.1.2 Electro-optic sampling

Exactly the same $\chi^{(2)}$ term is the underlying mechanism for detecting a THz electric field pulse in a time-resolved manner, a technique called electro-optic sampling [82]. In this case, the inputs are the THz pulse and a so-called probe optical pulse that is weak enough to not induce the intra-pulse nonlinear effects. The THz pulse
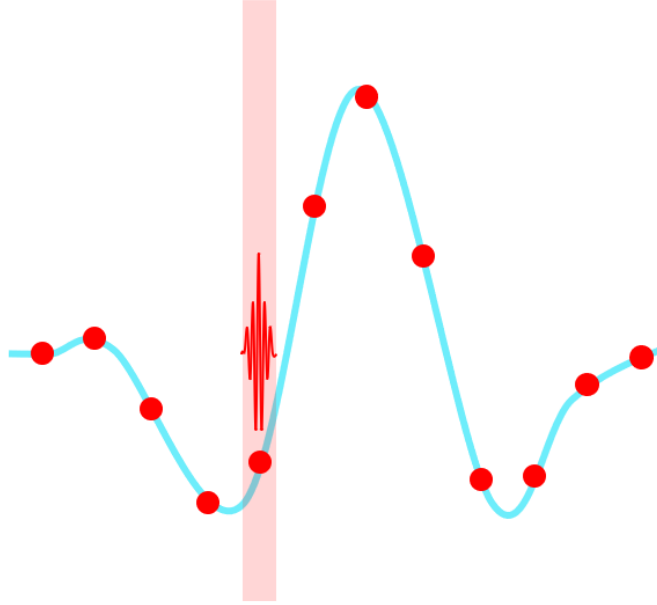
Figure 2.2: An illustration using electro-optic sampling to map a time-domain profile of a THz pulse (blue) by acquiring reading at different time delays with a optical probe pulse (red bullets)

induces a transient birefringence to the electro-optic crystal depending on the THz polarisation. The optical probe pulse transmitting through the crystal obtains an additional phase which renders, for example, the previously linearly polarised probe elliptical. An ellipsometry technique is then used to extract the sampled THz pulse from the probe, which will be covered in the next chapter.

Note that the THz pulse is distorted during the sampling process and during free-space propagation prior to the sampling. In low THz range, diffraction is significant as the beam spot size (<10 mm) and optics aperture used are comparable with the long THz wavelengths (1 THz = 0.3 mm). Kuzel et al. [83] calculated the THz wave distortion by the optics by considering diverging Gaussian wave approximation

$$E(f, z) = E_0(f)\frac{w_0}{w(z)} \exp(-i[kz - \arctan(\frac{z}{z_0})])$$

(2.6)

$$w(z) = w_0\sqrt{1 + (\frac{z}{z_0})^2}, \quad zo = \frac{\pi w_0^2}{c}f$$

(2.7)

E_0 is the electric field amplitude emitting from the source, f is the frequency, w_0

is the original THz beam waist size at the source, $w(z)$ is the diverged beam waist size after propagating for a distance z from the source. z_0 contains THz frequency term which gives the frequency-dependent beam waist size variation as the THz broadband pulse propagates. The spatial properties of the THz pulse i.e. effective focal length and beam waist size are altered when propagating through or reflected by focusing optics. Moreover, if the optics aperture sizes are smaller than the THz beam diameter, the beam loses its outer portion which contains its lower frequency spectrum. The cut-off frequency is

$$f_m = \frac{cL}{\pi w_0^2}[(2w_0/A)^2 - 1]^{1/2} \tag{2.8}$$

where L is the distance between the THz source and the focusing optic, A is the optic diameter.

On the other hand, the higher frequency spectrum is distorted during the sampling inside the nonlinear crystal. There exist optical phonon modes which strongly absorb in the low THz range. The phonon dips also vary the THz refraction index which induces the frequency-dependent phase mismatch. The $\chi^{(2)}$ also varies at frequencies close to the phonon modes. A combination of the factors above undervalues the actual THz electric pulse read by the electro-optic sampling and is summarised in the so called response function below [82].

$$S(\tau) = \frac{\pi \varepsilon_0}{c} \int_{-\infty}^{+\infty} E_{THz}(\Omega) f(\Omega) \exp(-i\Omega\tau) d\Omega \tag{2.9}$$

$$f(\Omega) = \frac{\omega^2}{|k'(\omega)|} \exp(-2\alpha(\omega)l)\chi^{(2)}(-\Omega; \omega + \Omega; -\omega) \left[\frac{\exp(i\Delta kl) - 1}{i\Delta k}\right] A_{opt} \tag{2.10}$$

$$A_{opt} = \int_{-\infty}^{+\infty} E_{opt}^*(\omega - \omega_0) E_{opt}(\omega - \Omega - \omega_0) d\omega \tag{2.11}$$

$\alpha(\omega)$ is the optical absorption of the probe pulse inside the crystal, the terms in the [ ] bracket describe the phase mismatch, and the integral A_{opt} is the autocorrelation function.

2.2 Femtosecond laser excitations in metals

When metals are hit by a femtosecond laser pulse, energy is initially deposited in the free electrons as photon-electron interaction is characterised by the fastest timescales. In a classical picture, the electric field components of the laser pulse accelerate and energise electrons, and the electron response time is immediate provided that the frequency of the laser pulse is still below the plasma frequency of the metal. The above description applies to intra-band transitions. In inter-band transitions, there is a variety of processes involved in exciting electrons from the valence band to the conduction band, for instance single and multi-photon absorption, and avalanche acceleration of valence electrons [84]. The high intensity laser pulse quickly renders the electron system to a highly non-equilibrium state, while the lattice system is still cold.

2.2.1 Electron-electron interaction

The non-equilibrium laser-excited, or hot, electrons subsequently transfer their energies to cold electrons via electron-electron scattering. The rate of energy transfer can be estimated by considering a simplified classical model of Coulomb interactions between electrons [84].

$$v_{ee} \approx n_e \sigma_e v_e \propto \frac{e^4 a_B^{-3}}{m_e^2 v_e^3} \tag{2.12}$$

v_{ee} is the electron-electron scattering rate, $n_e \propto a_B^{-3}$ is the electron number density, a_B is the Bohr radius, $\sigma_e \propto e^4/\varepsilon_e^2$ is the Coulomb scattering cross-section, ε_e is the permittivity, $v_e \propto e^2/\hbar$ is the electron velocity. Equation 2.12 gives an estimate of the order of $10^{16} s^{-1}$. More sophisticated models consider screening effects of the electron gas and the exchange interaction [84]. Such a fast rate means that after multiple scatterings, the electron system quickly reaches equilibrium. It has been shown that the equilibration process takes 50-100 fs in metals [85, 86]. At this state, the electron system can be described by Fermi-Dirac energy distribution with an elevated effective temperature.

$$f_{FD}(\epsilon) = [\exp\left((\epsilon - \epsilon_F)/k_B T\right) + 1]^{-1} \tag{2.13}$$

ϵ is the electron energy, ϵ_F is the Fermi level, k_B is the Boltzmann distribution, T is the temperature. For the excited electron system, effective electron temperature T_e is higher than the sample (or phonon) temperature.

2.2.2 Electron-phonon interaction

Electrons interact with the phonon system via the deformation potential induced by lattice vibrations. The energy transfer rate was first calculated for electrons close to the Fermi level by treating the electron system as having a higher effective temperature than the lattice system, in the condition that electrons follow a Fermi-Dirac distribution. The energy transfer rate reads [87]

$$\frac{\partial E_e}{\partial t}|_{e-ph} = -G_{e-ph}(T_e - T_{ph}), \quad G_{e-ph} = \frac{\pi^2 m_e v_s^2 n_e}{6T_e \tau(T_e)} \tag{2.14}$$

T_e is the effective electron temperature, T_{ph} is the phonon temperature, m_e is the effective electron mass, v_s the sound propagation speed n_e is the electron number density, τ is the scattering time which is dependent on T_e.

The above expression is only valid for low electron excitations. For femtosecond laser pulse excitations where a much broader electron energy range is involved, the electron density of states has to be included. Wang et al. [88] analysed the electron-phonon energy transfer rate by considering the electron-phonon scattering probability matrix and electron-phonon spectral density function, and obtained an expression

$$G_{e-ph} = \frac{\pi \hbar k_B \lambda < \omega^2 >}{g(\epsilon_F)} \int_{\infty}^{\infty} g^2(\epsilon) \frac{\partial f}{\partial \epsilon} d\epsilon \tag{2.15}$$

k_B is the Boltzmann constant, λ is the electron-phonon mass enhancement parameter, $< \omega^2 >$ is defined as the second moment of of the phonon spectrum, $g(\epsilon)$ is the electron density of states, f is the electron Fermi distribution function. The electron-phonon coupling dependence on T_e varies greatly for different metals due to their band structures [89]. For noble metals Au, Ag, Cu, the coupling is enhanced for the broadened electron spectrum $T_e > 10^3$ K due to excited deep d-band electrons. On the other hand, in Ni and Pt where the Fermi-levels are already at the edge of the high-density d-band state, the coupling reduces for extremely high electron temperatures

2.2.3 Electron-spin interaction

In ferromagnetic metals, electron-spin interaction has been extensively studied after the observation of ultrafast demagnetisation. A femtosecond pulse laser can quench magnetisation in less than 1 ps [50], in contrast to the common understanding that magnetic dynamics fall in GHz range. Models of electron-spin interaction have been developed by considering, for instance, Elliott-Yafet type electron-phonon scattering [90], Elliott-Yafet-like electron-electron scattering [91], and direct magnon emission due to non-equilibrium electrons [92]. The most accepted one, Elliott-Yafet type scattering refers to the asymmetry of spin-flip probabilities of electrons induced by phonons in the presence of spin-orbit interaction (SOI) [61]. In a system with SOI, the spin is not a conserved quantity. Any scattering events that lead to a change of electron momentum modify the admixture of electron spin-up and spin-down wave functions. The model successfully reproduces the discrepancy of timescale of demagnetisation in 3d metals (0.1-0.3 ps) and 5d metals (>10 ps) [61]. In 3d metals, the majority of spin angular momentum is carried by itinerant electrons and hence the effect of the spin-flip scattering to the macroscopic magnetisation is immediate. On the other hand, the localised 4f electrons carry most of the spin angular momentum in 5d metals, and therefore the demagnetisation requires additional energy transfer between the itinerant 5d electrons to the localised 4f electrons.

2.3 Three temperature model

A so-called three temperature model can phenomenologically describe concurrent energy transfer between electron, phonon, and spin systems [50]. The model assigns an effective temperature to each sub-system. The implication of this is that each system reaches equilibrium internally within the time resolution considered. The model consists of three time-dependent equations of energy for each system, with the absorbed laser energy term appearing in the electron energy dynamics part. For each interaction between two systems, a coupling term quantifies the rate of energy transfer.

$$C_e \frac{dT_e}{dt} = -G_{e-ph}(T_e - T_{ph}) - G_{e-s}(T_e - T_s) + P(t) \qquad (2.16)$$

$$C_{ph} \frac{dT_{ph}}{dt} = -G_{e-ph}(T_{ph} - T_e) - G_{ph-s}(T_{ph} - T_s) \qquad (2.17)$$
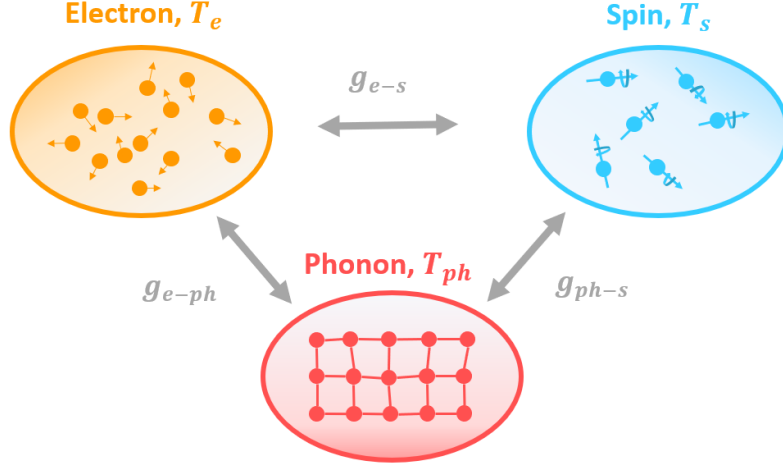
Figure 2.3: An illustration of three temperature model which treats electrons, spins, and phonons as separate systems with an internal temperature

$$C_s \frac{dT_s}{dt} = -G_{e-s}(T_s - T_e) - G_{ph-s}(T_s - T_{ph}) \tag{2.18}$$

C_i is the heat capacity of the i system, G_{i-j} quantifies the coupling between two systems, $P(t)$ is the absorbed laser power heating the electron system. Note that the phenomenological model above only provides the effective quantitative values for each interaction without offering an explanation on how the interaction works. Moreover, the model can only be applied for time resolution >100 fs i.e. after the electron system reaches equilibrium upon excitation. The theory then fails to describe the time-evolution of the electron temperature during the 50 fs pulse excitation as the concept of temperature breaks down [42]. Nevertheless, this model has decent success in extracting the electron-phonon scattering time from time-resolved transient reflectance measurements [93, 94], and electron-spin relaxation time from time-resolved magneto optical Kerr effects [50].

2.4 Femtosecond laser excitations in insulators

2.4.1 Coherent excitations

Here, several optical excitation channels that may be relevant in magnetic dielectrics studied in this thesis are briefly outlined. As explained earlier, insulators can interact with electromagnetic radiation via bound charges [Section 2.1]. The higher degrees of dielectric tensor can also explain the couplings between the electric field and
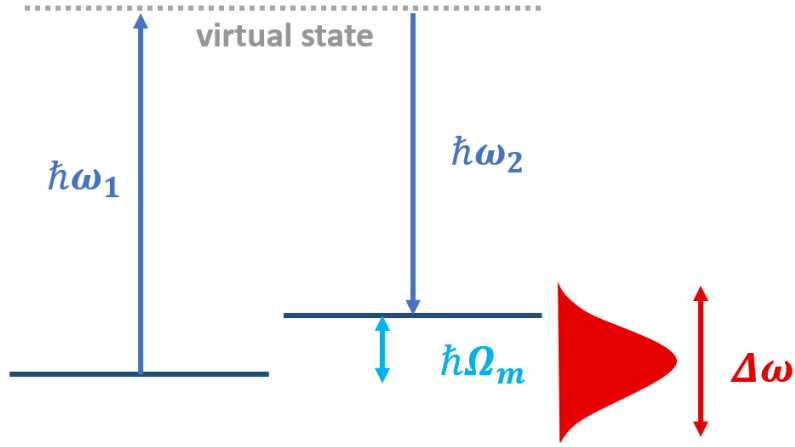
Figure 2.4: A schematic illustration of impulsive stimulated Raman scattering, where an inelastic scattering assisted by a virtual state can induce modes in THz frequencies. If the two ground states have different spin state, the scattering excites a magnon

magnetic ordering. The ensemble of these effects is referred to as opto-magnetism or inverse magneto-optical effects; they share the same symmetry and origins with magneto-optical effects i.e. Faraday effect, and Cotton-Mouton effect, but instead the electric field perturbations modify magnetic ordering [42]. Pershan et al. first described the coupling in terms of a thermodynamics potential [95]

$$\Phi = \alpha_{ijk} E_i(\omega) E_j(\omega)^* M_k(0) \tag{2.19}$$

where α_{ijk} is the magneto-optical susceptibility, E is the optical electric field, M is the static magnetisation.

The equation suggests that for a system with a non-zero magneto-optical susceptibility tensor component, electric field perturbations can be perceived as an effective magnetic field.

$$H_k = -\frac{\partial \Phi}{\partial M_k} = \alpha_{ijk} E_i(\omega) E_j(\omega)^* \tag{2.20}$$

The coordinate indices determine the combination electric field polarisation that can excite spins i.e. if the tensor component i=j is non-zero, linearly polarised light induces magnetic dynamics, in other words inverse Cotton Mouton effects. For excitations in antiferromagnets, the relevant thermodynamic potentials instead depend on the antiferromagnetic Néel vector L [95].

$$\Phi = \alpha_{ijkl}E_i(\omega)E_j(\omega)^*L_k \tag{2.21}$$

The microscopic origin of laser pulse excitations of opto-magnetism can be described in terms of impulsive stimulated Raman scattering (ISRS) [96]. Consider a laser pulse with central wavelength ω and bandwidth $\delta\omega$ exciting an electron from a ground state to a virtual state. The electron can subsequently relax to another ground state that has slightly higher energy and opposing spin state. This spin-flip inelastic scattering therefore excites coherent magnons in the system, and the output laser pulse has slightly lower energy [42]. The entire process is stimulated if the two frequencies are within the laser pulse bandwidth. The spin-orbit coupling plays an essential role in inducing the spin-splitting of the ground state [97].

2.4.2 Dissipative excitations

In optically absorbing insulators, the laser pulses excite the electron population in a higher electronic state and subsequent non-radiative relaxation transfers energy to phonons via electron-phonon coupling. The lattice heat can induce phase transition changing the crystal symmetry or simply inducing thermal expansion [42]. The phonons also transfer heat to magnons with two distinct time scales: ~ 1 ps and >100 ps. The fast magnon-phonon coupling occurs when lattice vibrations induce a transient change of exchange coupling as the overlap of the electron wave-function is modified [98]. The much slower relaxation channel is the coupling between lattice vibrations modes and spin wave modes [74]. In dielectrics with strong spin-orbit interactions i.e. $KCoF_3$, the magnon-phonon interaction is amplified. The coupling between modulated crystal field and unquenched orbital momentum of $Co_2{}^+$ results in relatively fast magnon-phonon interaction of ~ 2 ps [99].

2.5 Spin Hall effects

Spin Hall effects (SHE) refer to a set of relativistic spin-orbit phenomena that generate transverse spin currents out of a longitudinal electric current [27,31]. The name is coined for its resemblance with the ordinary Hall effect, where a transverse applied magnetic field induces a Lorentz force which separates trajectories of electrons and holes. SHE shares a similar origin with the anomalous Hall effects (AHE) [31]. AHE occurs in magnets which have population imbalance between majority and minority
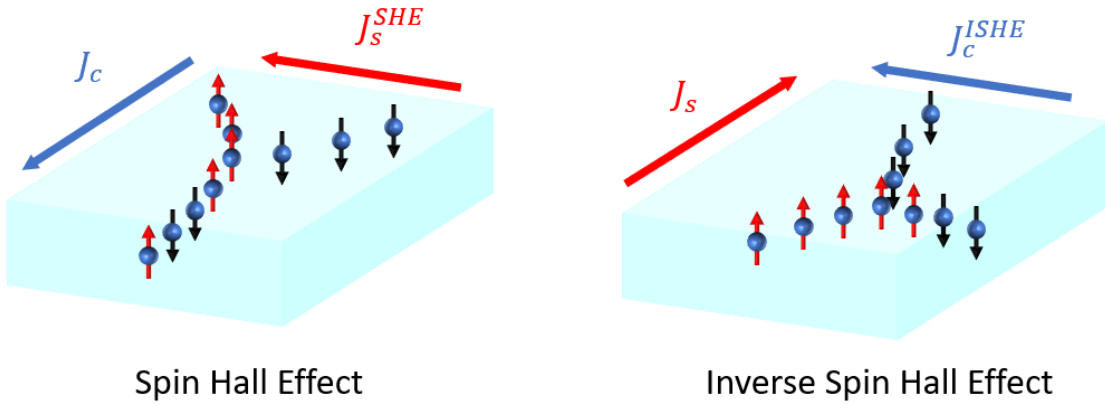
Figure 2.5: A schematic illustration of spin Hall effects where spin-dependent scatterings induce a transverse pure spin current, as well as the inverse spin Hall effect

spins. In this case, spin-dependent propagation deflection gives rise to a non-zero net charge current. In the SHE, which is observed in non-magnetic metals and semiconductors, the resultant charge current is zero [100]. The reciprocal effect also exists, referred to as inverse spin Hall effect (ISHE), where a pure spin current is converted to a transverse charge current [32]. Figure 2.5 illustrates the SHE and ISHE. The spin-orbit forces acting on the itinerant spins in the SHE originate from multiple microscopic mechanisms: intrinsic, skew scattering, and side-jump contributions. Hence, the spin Hall conductivity of a system is a summation of all the mechanisms, intrinsic contribution σ_{int}, skew scattering σ_s, and side-jump contribution σ_{sj}.

$$\sigma_{SH} = \sigma_{int} + \sigma_s + \sigma_{sj} \tag{2.22}$$

Intrinsic mechanisms The intrinsic SHE arises from the spin-orbit coupled bands of a crystal in the absence of disorder, hence the name. When an electron travels in a solid, the crystal field is perceived by the electrons as an effective magnetic field due to the spin-orbit interaction (SOI). This force is similar to a Lorentz force, but instead it gives asymmetric deflection depending on the electron spin polarisation [31]. The magnitude of the intrinsic SHE can be accurately estimated because ab initio calculations enable accurate prediction of the spin-orbit-coupled electronic band structure of a crystal. Its crystal-field origin means that 5d transition metals tend to have large intrinsic spin Hall contribution, for instance in Ta, W, and Pt [101]. Large spin Hall conductivity occurs when the electronic bands connected

by the SOI are close to the Fermi level.

Skew scattering   Skew scattering contribution describes the spin-dependent scatterings in the presence of impurities [102,103]. Originally, it was thought to arise only in the case of impurities with strong SOI. However, impurities with weak SOI have been shown to contribute if the crystal possesses strong spin-orbit-coupled electronic bands [31]. The strength of skew-scattering contribution depends on the disorder potential strength and impurity density. Its dependence on Bloch transport lifetime τ makes the skew scattering the dominant term in nearly perfect crystals. The τ dependence also distinguishes it from τ -independent intrinsic contribution [31].

Side-jump contributions   Side-jump contributions are loosely defined as the remaining contributions to the SHE once intrinsic and skew scattering contributions are isolated [104]. In a semi-classical approach, the side-jump contribution is pictured as a spin-dependent coordinate displacement of the electron wave packet perpendicular with its propagation direction, rather than a deflection of the wavevector, in the presence of impurities. The transverse shift means that the process is elastic. Similar to the skew scattering contribution, the side-jump contributions can originate from non-SOC impurities in a system with strong SOI and from disorders with strong SOC [31]. In contrast to skew scattering, the side-jump contribution is independent on the impurities density and hence the Bloch transport lifetime τ [105]. This serves as a tool to experimentally distinguish the two extrinsic contributions, for instance by varying sample temperature which modifies the longitudinal resistivity.

2.5.1   Inverse spin Hall effect

The inverse spin Hall effect (ISHE) is the reciprocal effect where a pure spin current is converted to a transverse charge current. As seen in Figure 2.5, the cross product between the spin polarisation and the spin current direction means that when the direction of two spin currents carrying opposite spins are anti-parallel, the resulting transverse charge currents are parallel. The conversion efficiency is quantified via spin-Hall angle Θ_{SH} [35]

$$j_c = \Theta_{SH} \frac{e}{\hbar} j_s \qquad (2.23)$$

j_c is the induced charge current, j_s is the pure spin current, e is the electron charge, $\hbar$ is the Planck's constant. All SHE contributions mentioned above are collectively quantified by Θ_{SH}.

Since its first experimental demonstration in FM/NM bilayer system using a spin-pumping configuration, ISHE has become the standard tool for spin current detection. Pt, W, or beta-phase Ta layers of several nm thickness are the common spin detection layers due to a combination of large spin Hall angle, high longitudinal resistivity and short spin diffusion length, making them ideal to generate strong voltage signals [106]. The ISHE has allowed the discovery of the spin Seebeck effect and opening a new field of spin caloritronics [107].

2.6 Magnetisation dynamics

This section briefly introduces the formalisms of magnetisation dynamics in various magnetic orderings: ferromagnets, antiferromagnets, and ferrimagnets. The magnetic ordering is dictated by the exchange interaction, a quantum mechanical phenomenon where the interplay between Coulomb interaction and Pauli exclusion principles of the fermionic electrons give a preferential spin arrangement.

The exchange interaction is by far the strongest magnetic interaction, equivalent to the magnetic field of 1000 T [108]. In (anti)ferromagnets, the exchange aligns a pair of spins (anti)parallel relative to each other [109–111]. Ferrimagnets have their neighbouring spins antiparallel, but their difference in angular momentum magnitude gives a net magnetic moment [112]. There are also other interactions existing in magnets [113]. For instance, magnetocrystalline anisotropy originates from the influence of the crystal field locking spins in a particular crystallographic direction. The shape of the material induces stray fields which also provide a preferential direction, but the effect is minimal for bulk magnets. An external field adds a Zeeman energy term to the Hamiltonian of the system, or induces field-torque term to the magnetisation dynamics.

2.6.1 Ferromagnetic resonance

In ferromagnets, time-dependent magnetisation dynamics can be phenomenologically described by the Landau-Liftshitz-Gilbert (LLG) [114, 115] equation by treating collective spins as one macroscopic moment that undergoes precession under a

non-collinear magnetic field.

$$\frac{\partial \mathbf{m}}{\partial t} = \mu_0 \gamma \mathbf{m} \times \mathbf{H_{eff}} + \alpha \mathbf{m} \times \frac{\partial \mathbf{m}}{\partial t} \qquad (2.24)$$

where $\mathbf{m}$ is the time-dependent dimensionless magnetisation, μ_0 is the Bohr magneton, γ is the gyromagnetic ratio, $\mathbf{H_{eff}}$ is the effective magnetic field, α is a damping factor. The 1st term on the right-hand side describes the magnetic torque exerted by an external magnetic field, shape anisotropy, intrinsic magneto-crystalline anisotropy field, and any type of perturbations which result in an effective magnetic field that favors the precession of the magnetisation. On the other hand, the 2nd term induces a net torque towards an equilibrium axis and summarises all the relaxation processes reducing the precession angle.

Upon perturbation by an oscillating magnetic field perpendicular to the equilibrium axis, typically in the microwave range, there is a frequency where the ferromagnet strongly absorbs the electromagnetic energy, and this condition is referred to as ferromagnetic resonance [116]

$$f = \sqrt{\left(\frac{\mu_0 \gamma}{2\pi}\right)^2 H(H + M_{eff})} \qquad (2.25)$$

where H is the DC external field and M_{eff} is the effective magnetisation. Equation 2.25 called Kittel formula, assumes negligible shape and magnetocrystalline anisotropy. Ferromagnetic resonance, typically in GHz range, has been a powerful technique to extract intrinsic parameters of the magnet by observing the dependence of the resonance frequency on the external field [117, 118]

2.6.2 Ferromagnetic spin waves and magnons

Equation 2.25 corresponds to the lowest frequency mode of uniform magnetisation precession without any net spin propagation. For a very low non-zero wave-vector, the k-dependence ω is determined by the long-range magnetic dipole-dipole interactions and it is referred to as magnetostatic wave. At larger k values, exchange interaction is involved as the nonuniform dynamics lead to a non-colinear orientation between adjacent spins and such dynamics are called spin waves. In ferromagnets, the nonuniform exchange interaction $H_{ex\sim}$ takes the form of [113]

$$H_{ex\sim} = q\nabla^2 \mathbf{M} \qquad (2.26)$$

Where q is referred to as the nonuniform exchange constants or exchange stiffness. Equation 2.26 adds the effective oscillating field acting on the magnetisation in Equation 2.24, which modifies the expression of the resonant frequency

$$\omega = \sqrt{(\omega_H + \eta k^2)(\omega_H + \eta k^2 + \omega_M \sin^2 \Theta_K)} \tag{2.27}$$

$\eta = \gamma q M_0$, $\omega_H = \gamma H$, $\omega_M = \gamma 4\pi M_0$, $\sin^2 \Theta_k = \frac{k_x^2 + k_y^2}{k^2}$. When $\eta k^2 \gg \omega_M, \omega_H$ the frequency has quadratic dependence on k,

$$\omega \cong \omega_H + \eta k^2 + \frac{1}{2}\omega_M \sin^2 \Theta_k \tag{2.28}$$

The approximation can successfully replicate spin wave dispersion for simple ferromagnets. For more complex magnetic structures, such as yttrium iron garnet (YIG) where there exist multiple branches of magnetic dynamic modes [119], Equation 2.27 only applies for the lowest ferromagnetic mode.

Magnons are quasiparticles of magnetisation oscillations and waves with energy $\epsilon = \hbar\omega$ and momentum of $p = \hbar k$, and carry spin angular momentum of $S = 1$. The dependence of ω on k follows the dispersion function explained above depending on the magnetic structure. In coherent oscillations by external perturbations, the number of magnons is linearly proportional to the squared amplitude of oscillating magnetisation [113]. Magnons have a finite lifetime and propagation length, which describe the relaxation of spin dynamics to the lattice [120].

At $T > 0$, magnons are incoherently excited by thermal energy from the lattice. The thermal magnons spectrum follows the magnon dispersion function and obeys Bose-Einstein statistics

$$f_{BE} = [\exp(\epsilon/k_B T) - 1]^{-1} \tag{2.29}$$

The concept of thermal magnons was first developed to describe the influence of temperature on bulk magnetisation [121]. The reduction of the magnetisation is expressed in terms of the number of thermal magnons across the entire k-space using Equation 2.29 and spin wave approximation Equation 2.28.

$$M(0) - M(T) = \frac{\gamma\hbar}{2pi^2} \int_0^\infty \frac{k^2 dk}{\exp(\hbar\eta k^2/k_B T)^{-1}} \propto \eta^{-3/2} T^{3/2} \tag{2.30}$$

Equation 2.30 is approximately valid only at low temperatures, where thermally excited magnons have low k. At very high temperatures and/or more complex magnetic structures where k^2 spin wave dispersion is not satisfactory, the temperature exponent deviates from $3/2$.

Further development by Holstein and Primakoff [122] demonstrated the quantum mechanical description of magnetisation dynamics by introducing magnon creation and magnon annihilation term to the Hamiltonian as means of excitation. For the simplest case where only exchange interaction and Zeeman energy are considered, the energy dispersion reads

$$\epsilon(k) = \gamma \hbar H + 2S \sum_g [1 - \exp{(ikr_g)}] I_g \qquad (2.31)$$

In the limit of low k and simple cubic lattice, the ϵ shows quadratic dependence of k like the classical derivation of spin waves.

2.6.3 Antiferromagnetic resonance

The semi-classical approach treats simple antiferrromagnets as two sublattice magnetisations with opposing direction. In contrast with ferromagnets, exchange interaction is accessible even in uniform precession mode and enters into time-dependent magnetisation dynamics [113]

$$\frac{\partial \mathbf{M_i}}{\partial t} = -\gamma_i \mathbf{M_i} \times \mathbf{H_{ef(i)}} + A_i \qquad (2.32)$$

where $\mathbf{M_i}$ is the sublattice magnetisation ($i = 1, 2$), γ_i is the magneto-mechanical ratio which may not be equal for the two sublattices, A_i is the dissipative term, $\mathbf{H_{ef(i)}}$ is the effective magnetic field felt by each sublattice in which the exchange interaction and the magnetocrystalline anisotropy are involved. One can write the total energy as

$$U_{tot} = JM_1M_2 - H(M_1 + M_2) + K(\sin^2 \theta_1 + \sin^2 \theta_2) \qquad (2.33)$$

The first term is the exchange interaction where the exchange constant is negative for antiferromagnets $J \equiv -J_{12}$, the second term is the Zeeman energy, the last term is the magnetocrystalline anisotropy, and θ_i is the angle between the sublattice magnetisation and the anisotropy axis. The effective field can be obtained by
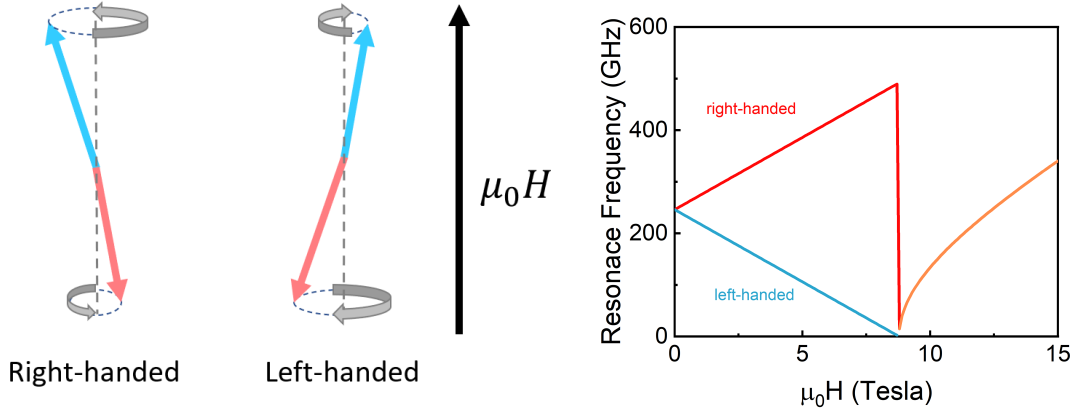
Figure 2.6: (left) an illustration of two easy-axis antiferromagnets in anti-parallel resonance modes with two opposing chirality and (right) the corresponding frequencies as function of applied external field. For a strong field $H_{SF} = \sqrt{2H_E H_a}$, the exchange and the anisotropy energy is overcome and the two sublattices undergo a 90^0 rotation

differentiating Equation 2.33

$$\mathbf{H_{ef1,2}} = -\frac{\partial U_{tot}}{\partial \mathbf{M_{1,2}}} = -J\mathbf{M_{2,1}} + H + \frac{K}{M_0^2}(\mathbf{M_{1,2}}\hat{z}) \qquad (2.34)$$

where M_0 is the equilibrium magnetisation of each sublattice. As seen later, the exchange term gives much stronger resonance frequencies in antiferromagnets. There are various types of antiferromagnets depending on the anisotropy (uniaxial, or biaxial), exchange interaction (isotropic and anisotropic), and spin configuration within one lattice unit. As the antiferromagnets studied in this thesis are $KCoF_3$ and $KNiF_3$, only Heisenberg uniaxial antiferromagnet is considered below.

In uniaxial antiferromagnets, depending on the relative orientation of the external magnetic field with the Néel vector there are 3 modes, antiparallel mode, canted mode, and saturation [113]. Antiparallel mode occurs at a low magnetic field collinear with the magnetic easy axis. The two sublattices undergo precession with opposite chirality and different opening angles [Figure 2.6]. A stronger external field leads to an unfavorable internal energy and the antiferromagnet minimises its energy by rotating its magnetic axis to be perpendicular with the field. This phenomenon is called spin-flop and occurs when $H_{ext} = H_{SF} \cong \sqrt{2H_E H_A}$, $H_E = JM_0$, $H_A = K/M_0$. In this configuration, the two sublattices are canted towards the field and a constant
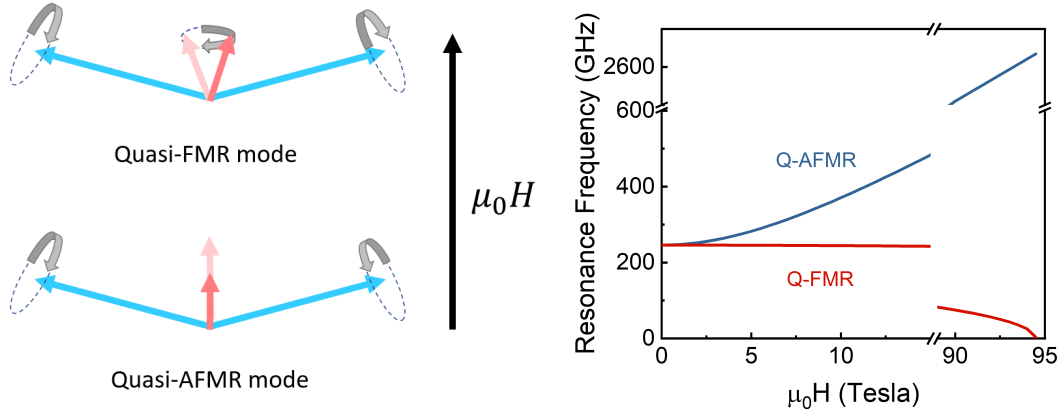
Figure 2.7: (left) Antiferromagnetic resonance modes when the external is applied perpendicular with the antiferromagnetic axis, resulting a quasi-FMR mode where the net moment precesses, or quasi-AFMR mode where the magnitude of the net moment oscillates, and (right) the corresponding frequency dependence of the field

net magnetic moment emerges. The canted mode has two sub-modes, often referred to as ferromagnetic mode and antiferromagnetic mode [Figure 2.7]. The former describes a ferromagnetic-like precession of the magnetic moment. In the latter, the net magnetic moment undergoes an oscillatory change in magnitude over time along its axis. These two-modes can also be achieved using a weak field perpendicular to the easy-axis although its frequency dependence on the field differs. At even stronger fields, typically above tens of Tesla, the two sublattices align with the field. The field dependence of all modes are summarised in Figure 2.6(b) and 2.7(b) using parameters obtained for MnF_2 [46]. At H=0, the AFMR is $\omega_{res} = \gamma\mu_0\sqrt{2H_E H_A}$, as H_E is of the order of 10^2 T and $H_A \sim 0.1$ T, antiferromagnetic resonance typically lies within the THz range.

2.6.4 Antiferromagnetic spin waves and magnons

Using a simplified approach by considering only the nearest neighbouring pairs, the dispersion of simple cubic antiferromagnets reads [113, 123]

$$\omega_{AF}(k) = \gamma\mu_0\sqrt{(H_E + H_A)^2 - H_E\gamma_k} \tag{2.35}$$

where γ_k describes the coordinate of neighbouring spins, for a cubic crystal γ_k is given by

$$\gamma_k = \frac{1}{3}(\cos(k_x a) + \cos(k_y a) + \cos(k_z a)) \tag{2.36}$$

Antiferromagnetic magnons carry two different spins S=1 and S=-1, intuitively described by two opposing chirality of precession. The two magnons have exact dispersion at zero field and hence at equilibrium, when the populations of the opposite chirality magnons are the same, no net spin population exists in the antiferromagnet. Applying an external field breaks the degeneracy by shifting the k=0 mode downward (upward) for spin up (down), as shown earlier in Figure 2.6(b). When the field is perpendicular to the Néel vector, a net magnetic moment is induced and the degeneracy is similarly lifted as in Figure 2.7(b).

2.6.5 Ferrimagnets

Mathematical treatment of ferrimagnets resembles antiferromagnets except that the magnetisation of the two sublattices differs in magnitude. Ferrimagnets have multiple modes: the lowest ferromagnetic mode and higher exchange modes. In the ferromagnetic mode, the two sublattices are always antiparallel and hence the exchange interaction is not involved. This results in low frequencies in the GHz range. Higher exchange modes have much higher frequencies typically in the infrared range. [119]

2.7 Spin transfer torque and spin pumping

Spin-polarised currents can exert torques when flowing inside a magnet and drive the magnetisation out of equilibrium. This effect is called spin-transfer torque and requires the polarisation of the spin current to be orthogonal to the magnetisation direction. A spin current can be induced by, for example, applying a non-polarised electric current into a ferromagnetic layer.

The reciprocal effect exists where coherent magnetisation oscillations inject a spin current to the adjacent layers as a consequence of the conservation of angular momentum, and this phenomenon is called spin pumping. The emission of the spin current results in a loss of angular momentum which manifests with an additional damping term in the LLG equation. The magnitude of the pumped spin
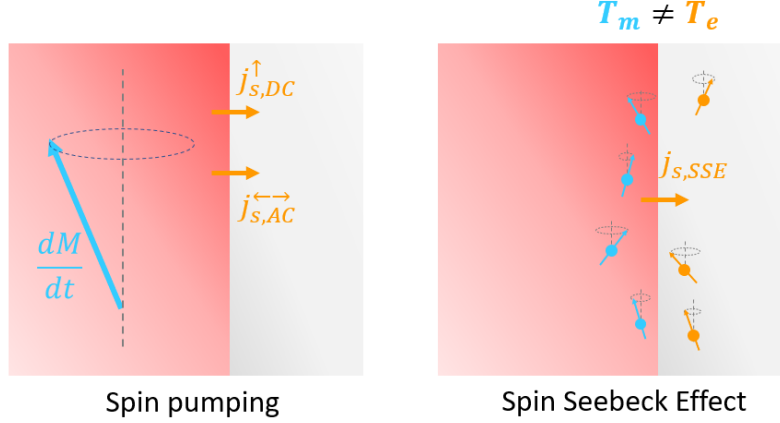
Figure 2.8: An illustration of (left) spin pumping and (right) spin Seebeck effect, where the former refers to a coherent precessional motion of collective spins inducing a net spin transfer across the interface while the latter can be considered as the incoherent counterpart which is induced by thermal fluctuations

current depends on the precession angle and spin mixing conductance $g_{\uparrow\downarrow}$ [38], a parameter describing the efficiency of the interfacial spin transport.

$$\mathbf{j_s} \propto g_{\uparrow\downarrow}\mathbf{M} \times \frac{d\mathbf{M}}{dt} \tag{2.37}$$

In the adjacent layer, typically a non-magnetic metal, the spin current consists of DC and AC components. The DC component is polarised along the equilibrium magnetisation direction $\mathbf{M_{eq}}$ and the AC spin current polarisation follows the oscillating magnetisation in a plane perpendicular to $\mathbf{M_{eq}}$. Spin pumping can also occur in antiferromagnets because the time-dependent magnetisation of the two sub-lattices do not cancel out and give a net oscillating moment [124]. The inverse spin Hall effect (ISHE) is used in spin pumping studies to convert the spin current into an electric signal.

2.8 Spin Seebeck effect

Spin caloritronics was discovered only a decade ago with the experimental work in NiFe/Pt by Uchida et al. [107] whereby applying Joule heating on a metallic Pt strip could harness spin current from NiFe, detected via the ISHE. Spin caloritronics encompasses all thermal effects that lead to spin current generation for any symmetries and material structures, as well as their reciprocal effects [36]. The nomenclature of

spin caloritronic effects are derived from the well-known thermoelectric-effects family, despite some of them having completely different origins. This section focuses mainly on providing a literature review on the spin(-dependent) Seebeck effect.

In the Seebeck effect, a temperature gradient in a metal generates electric current due to the thermal broadening of the Fermi-Dirac distribution, leading to electron diffusion [36]. The generated voltage is proportional to the temperature gradient ∇T

$$V_{SE} \propto S\nabla T \tag{2.38}$$

where S is the Seebeck coefficient summarising the role of electron energy distribution function and diffusion or conductance σ [36]

$$S_{SE} = -e\frac{\pi^2 k_B^2}{3e^2}T\frac{\partial}{\partial\epsilon}\ln\sigma(\epsilon)|_{\epsilon_f} \tag{2.39}$$

When the metal is ferromagnetic, all those parameters become spin dependent. The generated voltage then can be modelled as if the FM has two effective Seebeck coefficients for spin-up and spin-down carriers. The asymmetry in the two spin populations renders the electric current spin-polarised, hence the name spin-dependent Seebeck effect [125].

$$S_{SDSE} = (\sigma^\uparrow S^\uparrow + \sigma^\downarrow S^\downarrow)/(\sigma^\uparrow + \sigma^\downarrow) \tag{2.40}$$

where $\sigma^{\uparrow,\downarrow}(S^{\uparrow,\downarrow})$ is electron conductivity (Seebeck coefficient) for spin-up and spin-down, respectively. Earlier experiments classify the spin-dependent Seebeck effect into longitudinal or transverse depending on whether the electric current is longitudinal or transverse to the temperature gradient [126].

In ferromagnetic insulators (FI) where no itinerant electrons are present, spin current is carried by propagating magnons [120]. In this case it is referred to as spin Seebeck effect (SSE) to distinguish it from the electron carrier counterpart. The longitudinal spin Seebeck effect has been extensively studied in conjunction with magnonic spin transport [74,120,127–130]. Magnons can be excited by thermal spin fluctuation at T>0, and follow Bose-Einstein statistics [Equation 2.29]. The bulk temperature gradient induces an excess in the non-equilibrium magnon density δn_m, which drives the spin current j_s [120]

$$\delta n_m = \frac{1}{(2\pi)^3} \int d^3k (n_k - n_{k,0}) \tag{2.41}$$

$$\mathbf{j_s} = \frac{\hbar}{(2\pi)^3} \int d^3k \mathbf{v_k}(n_k - n_{k,0}) \tag{2.42}$$

n_k is the number of magnons, $n_{k,0}$ is the number of magnons in thermal equilibrium which follows Bose-Einstein distribution function, $\mathbf{v_k}$ is the magnon propagation velocity with wave vector k.

Two contributions can be distinguished that depend on the spatially dependent magnon number density

$$\mathbf{j_{s,\delta n_m}} = -\frac{\hbar}{(2\pi)^3} \int d^3k \tau_k \mathbf{v_k}(\mathbf{v_k}.\nabla \delta n_k(\mathbf{r})) \tag{2.43}$$

and the temperature gradient

$$\mathbf{j_{\nabla T}} = -\frac{\hbar}{(2\pi)^3} \int d^3k \tau_k \frac{\partial n_{k,0}}{\partial T} \mathbf{v_k}(\mathbf{v_k}.\nabla T) \tag{2.44}$$

where τ_k is the magnon relaxation time.

In steady-state condition, the magnons follow a diffusion equation. The thermal gradient contribution, often called as phonon drag [73], involves the magnon-phonon interaction in which the phonon current drags magnons, assuming that the magnon temperature follows the phonon temperature $T_m = T_p$. A non-magnetic metal with a large spin-Hall angle is used as a spin sink and converts the pure spin current into an electrical signal.

Magnon transport parameters, such as magnon lifetime and propagation length influence the magnitude of the bulk LSSE signal. For instance, the magnon propagation length l_m of YIG is in the order of μm [120], and therefore the influence of sample thickness on the magnitude of the LSSE signal is much stronger below l_m than above it. As temperature decreases l_m increases, enhancing the magnitude of the LSSE as more magnons arrive at the interface where they are converted into a charge signal via the ISHE [131]. Lowering temperature to <200 K, however, decreases the population of the thermally excited magnons [Equation 2.29] and the LSSE signal eventually goes to zero at T= 0 K [120, 131, 132].

Another contribution originates from the difference between the effective magnon temperature in FI and the electron temperature in the NM [73, 74, 133]. In

this case, interfacial exchange interaction mediates the angular momentum transfer between localised spins in YIG and the itinerant electrons. The thermally excited magnons in YIG transfer angular momentum to the adjacent Pt, and conversely the thermally excited electrons in Pt that are scattered at the interface excite magnons in YIG. In equilibrium condition, the spin currents in both directions cancel each other and the net spin accumulation is zero. When $T_e \neq T_m$, the two spin currents are not equal, resulting in a net spin accumulation that is proportional to $T_e - T_m$.

In a semiclassical approach, the model of the interfacial contributions to the SSE is constructed on the assumption that incoherent spin fluctuations, both in FI and NM, exert torques on each other. The spin fluctuations are described as Gaussian ensemble [73]

$$< h^i(t) >= 0 \tag{2.45}$$

$$< h^i(t)h^j(t) >= \frac{2k_B T \alpha}{\gamma a^3 M_0} \delta_{i,j} \delta(t - t^{'}) \tag{2.46}$$

h is defined as the noise magnetic field due to spin fluctuations at temperature T, a^3 is the cell volume of the magnet. And the FI and NM dynamics are described by the LLG equation

$$\frac{\partial \mathbf{M}}{\partial t} = [\gamma(\mathbf{H} + \mathbf{h_{FI}}) - \frac{J_{sd}}{\hbar}\mathbf{s}] \times \mathbf{M} + \frac{\alpha}{M_0}\mathbf{M} \times \frac{\partial \mathbf{M}}{\partial t} \tag{2.47}$$

and the Bloch equation, respectively.

$$\frac{\partial \mathbf{s}}{\partial t} = -\frac{1}{\tau_{sf}}\left[\mathbf{s} - s_0\frac{\mathbf{M}}{M_0}\right] - \frac{J_{sd}}{\hbar}\frac{\mathbf{M}}{M_0} \times \mathbf{s} + \mathbf{h_{NM}} \tag{2.48}$$

J_{sd} is the exchange interaction between itinerant electrons ('s') in NM and localised spins at FI side ('d'), $\mathbf{s}$ is the spin density in NM, $s_0 = \chi_{NM}J_{sd}$ is the local equilibrium spin density, χ_{NM} is the spin susceptibility in NM, τ_{sf} is the spin-flip scattering time. Their non-collinearity due to thermal fluctuations induce effective torques. The resulting spin current is

$$\mathbf{I_s} =< \frac{\partial s^z(t)}{\partial t} >= -G_s\left[< \left(\mathbf{m} \times \frac{\partial \mathbf{m}}{\partial t}\right)^z > - < \left(\mathbf{m} \times \frac{\partial \mathbf{m}}{\partial t}\right)^z >_{loc-eq}\right] \tag{2.49}$$

where $G_s \approx J_{sd}^2 \chi_{NM} \tau_{sf} / \hbar$. The first term on the right-hand side represents the spin pumping by thermal fluctuations while the second term is the spin backflow. The two thermal spin currents are equal and cancel each other if the $T_{FI} = T_{NM}$. Conversely, inducing temperature bias results in a net spin accumulation in the NM.

Alternatively, the interfacial SSE can be expressed using spin pumping formalism with the spin-mixing conductance term. Seifert et al. found the relation between spin mixing conductance and the interfacial J_{sd} exchange interaction as [72]

$$Reg^{\uparrow\downarrow} = \frac{4\pi | < \mathbf{S_{FI}} > |^2 J_{sd}^2 \chi_{NM} \tau_{sf}}{\hbar a^2} \tag{2.50}$$

where $| < \mathbf{S_{FI}} > |$ is the average spin moment in a unit cell in the FI.

In a quantum mechanical approach, the interfacial SSE is seen as the inelastic spin-flip scattering of electrons at the interface, which creates/annihilates magnons at the FI side. The scattering is governed by J_{sd} exchange term Hamiltonian [134, 135]

$$H_{int} = -J_{sd} \sum_i S_i^d \cdot s_i^s \tag{2.51}$$

$$H_{int} = -J_{sd}\sqrt{2S^d} \sum_{\mathbf{k},\mathbf{k'},\mathbf{q}} (a_{\mathbf{q}}^+ c_{\mathbf{k}\uparrow}^+ c_{\mathbf{k'}\downarrow} + H.c.) \tag{2.52}$$

S^d and s^s are the localised and itenerant spins in the magnetic insulator and in NM, respectively, $a_{\mathbf{q}}^+$ is the magnon creation operator, $c_{\mathbf{k}\uparrow}^+$ ($c_{\mathbf{k'}\downarrow}$) is the conduction electron creation (annihilation) operator. Again, the effective temperature asymmetry between electrons and magnons leads to a net spin accumulation.

The spontaneous magnetisation in ferromagnets/ferrimagnets provides the spin-dependent chemical potentials and hence asymmetric probabilities between spin up-down and spin down-up scattering events. Otherwise, an external field is needed to induce the spin asymmetry. In uniaxial antiferromagnets, when the magnetic field is parallel to the Néel vector $H||L$, the Zeeman splitting breaks the degeneracy between the two magnon dispersions carrying spin-up and spin-down angular momentum, respectively. The Hamiltonian of Zeeman-split antiferromagnets reads [136]

$$H = \sum_k \hbar(\omega_{\alpha k} \alpha_k^+ \alpha_k + \omega_{\beta k} \beta_k^+ \beta_k) \tag{2.53}$$

$\omega_{\alpha k}$, $\omega_{\beta k}$ is the magnon resonance frequency for the two modes, α_k^+, α_k, β_k^+, β_k are the magnon creation and annihilation operator.

Chapter 3

Building a THz Time-Domain Spectroscopy

This chapter covers design considerations, instruments employed, optimisations, and performance tests of the Terahertz time-domain spectroscopy (THz TDS) set-up in Chiara Ciccarelli's group, funded by the Winton programme for the physics of sustainability to approach the studies of spintronics at timescales of picoseconds. At THz frequencies exciting physics can be accessed, such as ultrafast magnetisation quenching, non-equilibrium interactions between electrons, phonons, and spins, and antiferromagnetic spintronics. The first part of my PhD involved building a THz TDS setup after spending four months period in the group of Prof. Alexey Kimel in Radboud University Nijmegen with the work-away scheme for training on this technique.

This chapter first outlines the core instruments in place, such as an amplified femtosecond laser, an optical parameter amplifier, a closed-cycle cryostat, an electromagnet and a lock-in amplifier. The considerations made while designing the setup include allowing access to two different experimental working stations, using one motorised linear stage to allow for two different types of measurements, employing noise suppression techniques and building an electro-optic sampling + balanced detector assembly. The latter parts of the chapter illustrate the signal stability and signal-to-noise ratio obtainable with this set-up by using a both a ZnTe crystal and a Co/Pt bilayer as THz emitters. The Co/Pt bilayer samples were fabricated by Jeon Kun-rok. An acknowledgement must go to the Cavendish workshop, especially Chris Burling, Gary Large, and Ollie Norris, and Dominik Hamara, who have as-

sisted for constructing the cryostat lifting system, and Roger Beadle and Tom Sharp that have designed and produced the enclosure for Nitrogen purging.

3.1 Description of the facilities

Solstice Ace The core component of our THz time-domain spectroscopy setup is the Solstice Ace, an amplified Ti:Sapphire femtosecond laser system which consists of a pulsed seed laser, a regenerative amplifier, a pulse stretcher and compressor. The seed laser is the Mai Tai mode-locked Ti:Sapphire oscillator operating at 42.4 MHz frequency, 800 nm central wavelength and 60 nm bandwidth. The seed pulse is initially stretched to reduce the peak power prior to amplification. A Pockel cell periodically selects the seed pulse entering the amplifier cavity, which consists of a Ti:Sapphire crystal placed inside a reflective cavity and pumped with a 4 W 532 nm continuous wave laser. The seed pulse triggers coherent emission from the pumped crystal that is identical with the seed laser spectrum but with much higher power. After several round trips the pulse gains several orders of magnitude of amplification and exits the cavity controlled by another Pockel cell. Lastly, the pulse is compressed back to the original pulse width. Our Solstice Ace output is 1.6 mJ per pulse with 5 kHz pulse repetition rate, 800 nm central wavelength and 35 fs pulse width.

TopasPrime The TopasPrime optical parametric amplifier allows us to change the central wavelength of the pulse in the range of 290-2600 nm. The system relies on higher order electro-optic effects, such as second harmonic generation, sum, and difference frequency generation, to generate the desired wavelengths. The typical energy conversion efficiency is 15-30% across the wavelength range.

Optical cryostat A closed-cycle optical cryostat from ARScryo (DE-204SFg) is employed to control the sample temperature down to 4 K. The closed-cycle cryostat has a built-in helium cooled compressor to cool the fridge at the top part. A small volume of helium gas is fed to conduct the cooling to the sample holder part. The fridge and the sample holder are not physically in contact to isolate the vibrations from the fridge. A coil heater is placed near the sample for a fine control of the temperature and can provide heating up to 450 K. The sample needs to be in vacuum (10^{-6} mbar). The optical aperture is 25 mm at the four sides, where fused

silica windows are used for their transparency at the visible and THz range without inducing any non-linear optical effects.

Electromagnet An electromagnet up to $\mu H = 0.85$ T is used to set the sample magnetisation direction. The relatively large gap needed between the two coils to fit the cryostat finger (30 mm width) hinders achieving a stronger field.

Lock-In amplifier A Zurich Instrument HF2LI double lock-in amplifier is used for signal processing in combination with an optical chopper and a balanced photodetector, which will be explained in Section 3.3. The instrument also has a built-in digital oscilloscope which is useful for initial alignment where direct inspection of the pulse hitting the photodiodes is needed.

3.2 THz emission/transmission beam steering design

The layout of our THz TDS lab is shown in Figure 3.1. The main idea is to combine THz emission and transmission by using the same delay line and allowing an easy swap between the two modes. Other considerations include an easy access to the cryostat and the detection assembly, laser sharing between our setup and Hannah Joyce's setup, an easy access to the TopasPrime output using the same delay line, while having sufficient space for the rather bulky electromagnet and the cryostat mechanical supports. The design also considers the possibility of modifying the setup to optical pump + THz probe experiment by adding an additional delay line.

Our setup uses the 800 nm direct output from the Solstice Ace as default, unless studies using other wavelengths are needed. The 8 W Solstice Ace direct output is split with a ratio of 66:33 for TopasPrime input and direct use, respectively. The $\sim$2.6 W 800 nm is further split 50:50 (Eksma) for our setup and Hannah Joyce's setup. The beam can be directed to an optical interferometric auto-correlator built by Dominik Hamara for pulse width inspection. Otherwise, the beam is directed to a beam sampler (Thorlabs BSF20-B) to separate the pump and probe beams with ratio of 99:1 [Figure 3.1]. As the pump beam is maintained to have a big diameter of 11 mm, 2-inch diameter silver coated mirrors (Thorlabs PF20-03-P01) are used. While for the probe beam travelling with a smaller diameter of 3 mm 1-inch diameter mirrors (Thorlabs PF10-03-P01) are used.

Figure 3.1: Illustration of the THz setup
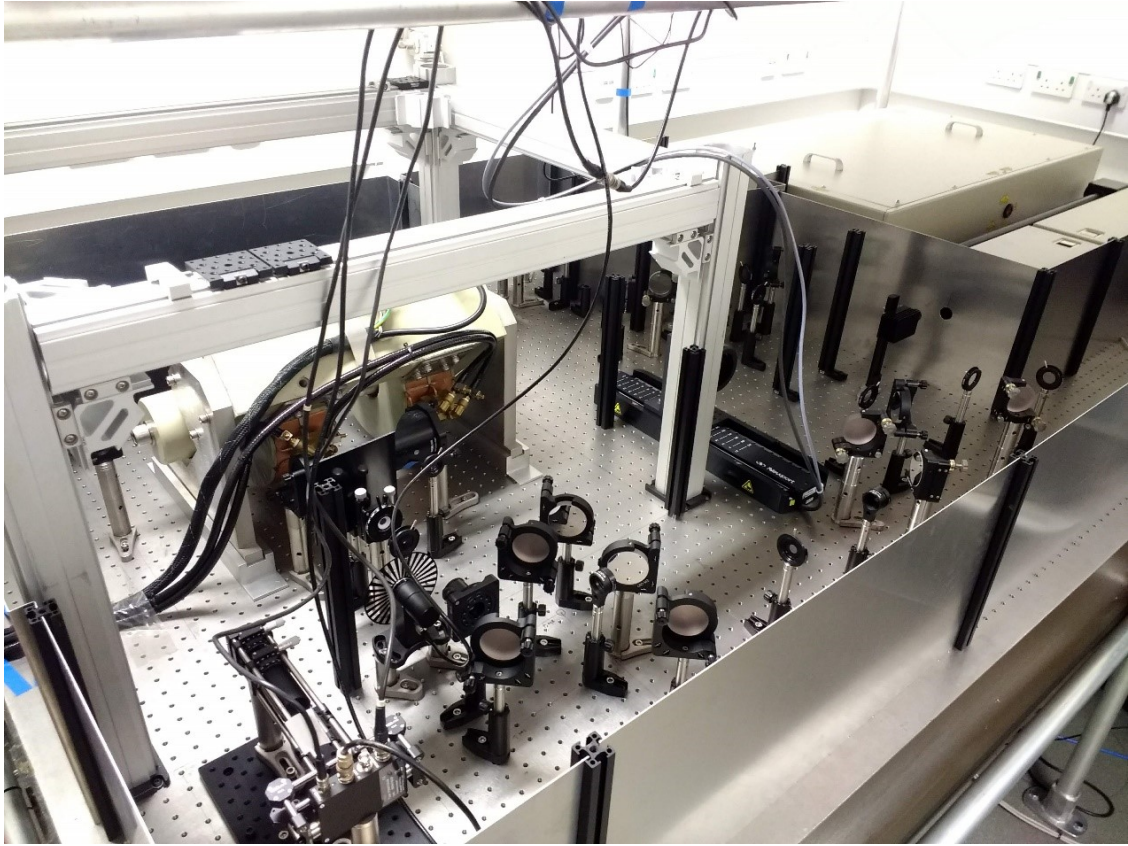
Figure 3.2: Photograph of the first version of the THz setup

3.2.1 Delay line

As mentioned earlier the beam is split into two parts, referred to as the pump and the probe, and their path lengths must be roughly equal, as required in pump-probe detection [137]. The pump beam is used to excite a THz electric field pulse from a sample or a THz emitter while the probe beam samples the THz signal in a time-resolved manner. This requires the THz beam and the probe beam to arrive at the detection assembly at the same time. For constructing time-domain data, the probe needs to sample different points of the THz time-domain waveform, and therefore the arrival of the probe and the THz must be systematically controlled. An automated delay line is hence employed.

The delay line consists of a silver-coated hollow retro-reflector (Laser Components OW-25-10E) and a motorised linear stage (Newport DL 325). The size of the retro-reflector is chosen to accommodate our laser spot size of ∼11 mm FWHM.
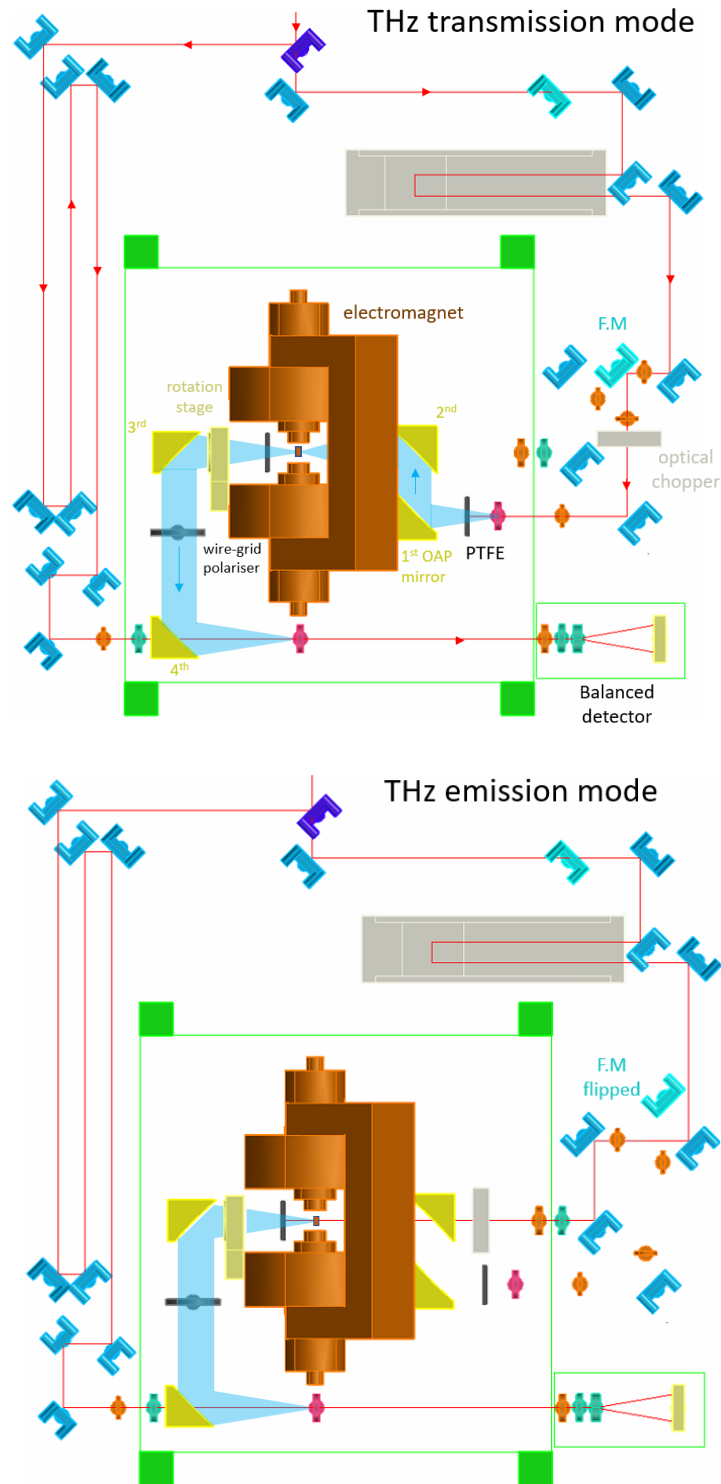
Figure 3.3: Beam trajectory in (top) THz transmission mode and (bottom) THz emission mode where flipping a mirror and a lens and moving the optical chopper are required
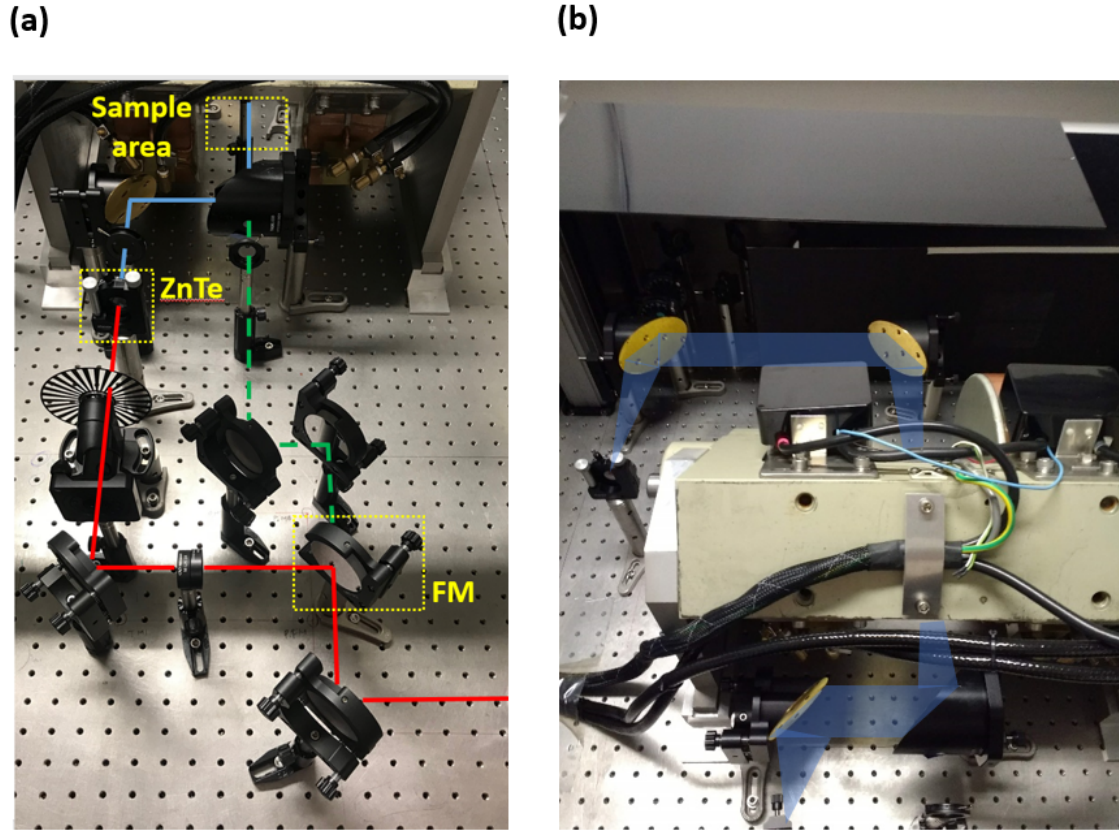
Figure 3.4: (a) Pump beam steering in THz transmission or THz emission setup (b) THz beam steering using 4 off-axis parabolic mirrors

Silver coating is chosen to cover the TopasPrime output range from visible wavelengths to mid-infrared. The linear stage has good movement stability (yaw of 50 μrad, pitch of 90 μrad) and sufficient minimum step resolution of 0.075 μm for an an optical delay line. The two mirrors placed before the retro-reflector ensure that the incoming beam is collinear to the linear stage, and hence linear movements of the retro-reflector should not substantially drift the beam pointing after the stage. However, the yaw and the pitch unavoidably contribute to beam pointing fluctuation. As the same linear stage is used as the delay line for the TOPAS-Prime output, the linear stage position on the optical table is carefully calculated for ensuring the path length of the beam travelling inside the TOPAS-Prime is roughly equal with the 2.6 W Solstice output.

3.2.2 Pump beam steering

Our THz-TDS setup allows switching from THz transmission to THz emission mode by just flipping a mirror (FM in Figure 3.4) and moving the optical chopper. In the THz transmission part, there is a two-mirror system for easy alignment of the pump beam hitting the ZnTe emitter. A linear polariser and a multiple-lens system are placed prior to the ZnTe emitter for tuning the beam diameter. The ZnTe emitter is placed roughly at the focal point of the 1st off-axis parabolic (OAP) mirror such that the 1st OAP collimates the emitted THz beam. The 2nd OAP mirror focuses the THz beam at the sample. The THz emission can be accessed by flipping the the flip mirror. In this mode, the pump beam is delivered to the sample point using a two-mirror system. There is a small hole in the 2nd OAP to allow the pump beam hitting the sample directly. Care should be taken to minimise the clipping at the 2nd OAP mirror by using focusing optics.

3.2.3 THz beam steering

A 4 OAP mirror configuration is employed in our THz setup. The 1st OAP mirror (Thorlabs MPD269-M01) focal length of 6 inch is chosen to minimise the size of the nitrogen purged enclosing area. Although ideally one should use the largest possible OAP mirror size as possible to maximise THz beam capturing, space constraint imposed by the electromagnet only allows us to use a 2-inch diameter. The distance between the 1st and the 2nd OAP mirror is limited by the size of the electromagnet. The THz beam should not be affected by the distance as the beam is collimated. The 2nd OAP mirror (Thorlabs MPD399HM01) has the biggest possible size (3-inch) with the longest focal point (9-inch) available in the market for 90° reflection, for better focusing and ensuring the distance between the sample and the 2nd OAP mirror is bigger than the electromagnet radius. The 3rd OAP mirror (Thorlabs MPD399-M01) also has 3-inch diameter and 9-inch focal length for symmetry purpose and giving enough space for a motorised rotation stage. The 4th OAP mirror (Thorlabs MPD399HM01) steers the THz beam, as well as allows the probe beam to pass through its hole, to the ZnTe detector crystal.
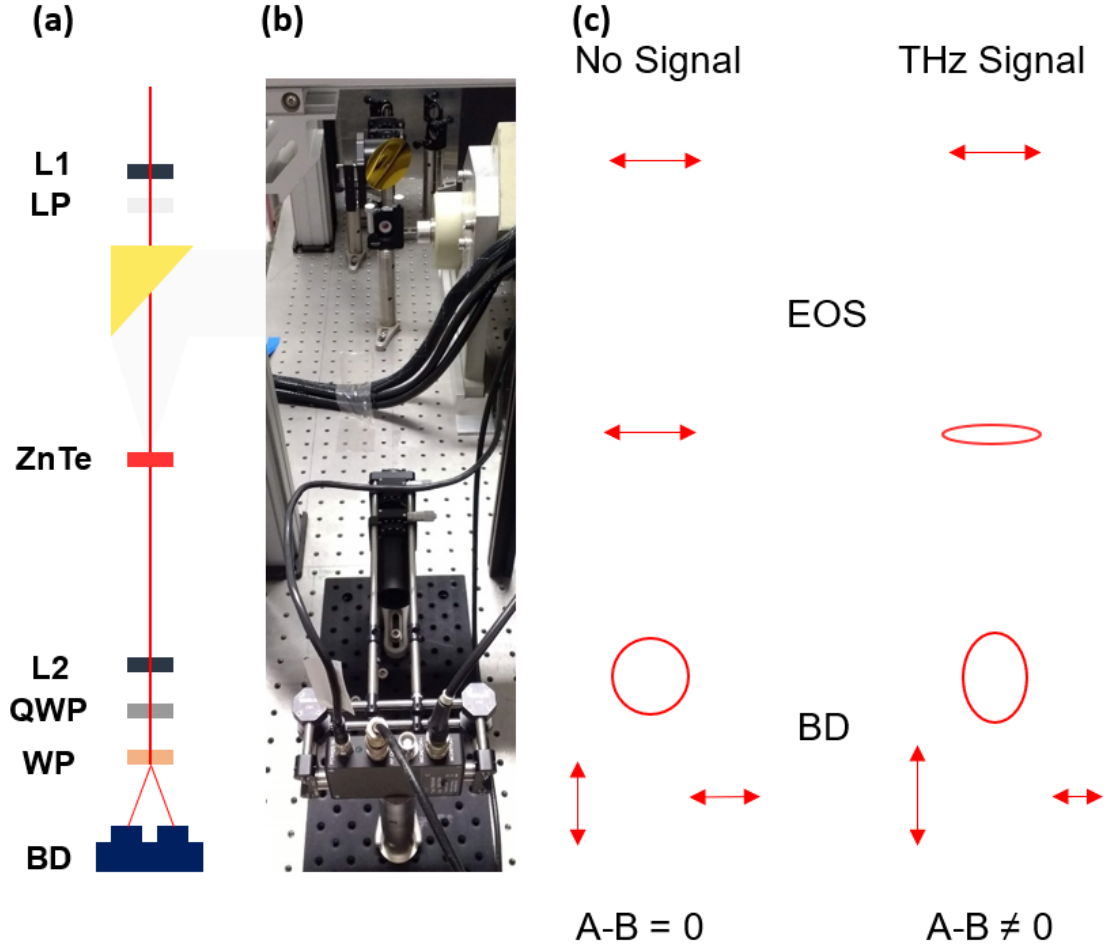
Figure 3.5: (a) Schematic illustration and (b) photograph of the electro-optic sampling + balanced detection assembly, (c) illustrations of balanced detection in detecting phase change in the probe beam

3.3 THz time-domain detection

3.3.1 Probe beam delivery and electro-optic sampling

Electro-optic sampling is used to probe the THz electric field with sub-picosecond time resolution [Sectoion 2.1.2]. The probe beam spatially overlaps with the THz beam by passing through the hole at the center of the 4th OAP mirror. Prior to reaching the 4th OAP mirror hole, the probe power is heavily attenuated by ND filters (Thorlabs NEK01) to <100 μW. The probe beam arriving at the ZnTe is polarised parallel with the optical table plane using a Glan-Thomson polariser (Thorlabs TH10M-B) and focused using an achromatic lens (Thorlabs AC254-400-B-
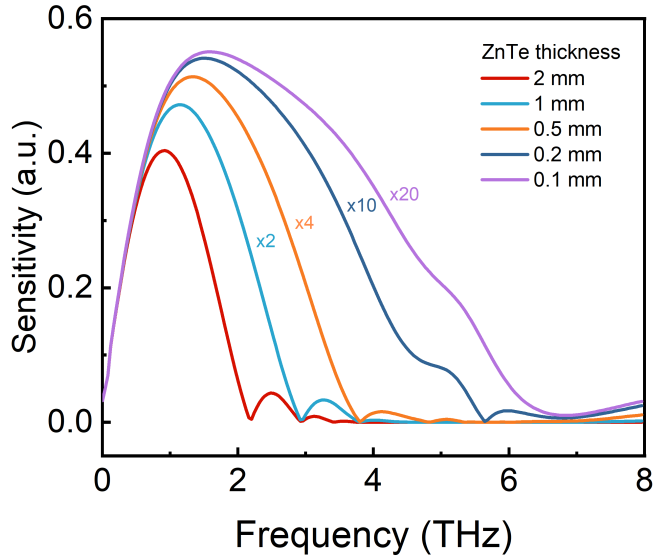
Figure 3.6: Calculated frequency spectrum of electro-optic sampling using ZnTe 1 mm

ML). Tight focusing with minimum astigmatism is important for ensuring the spatial overlap with the THz beam having roughly equal spot size across its wavelength spectrum. As explained in Section 2.1.2, when the probe mixes with the THz beam in the ZnTe detector crystal, the probe acquires an additional phase depending on the THz field magnitude and polarisation. The THz electric field can be deduced by probing the phase change when THz pulses exist (at 2.5 kHz) compared to raw probe beam (at 5 kHz repetition). This frequency difference is induced by an optical chopper, which will be explained in Section 3.5.

The ZnTe crystals used as the emitter and the detector are 1 mm thick, 10x10 mm from Eksma Optics. The choice of thickness is the trade-off between the strongest signal possible and decent bandwidth. A thicker ZnTe crystal induces stronger probe ellipticity for the same input [Figure 3.6 [138]]. On the other hand, the high frequency spectrum is more distorted for a thicker crystal due to the phase mismatch between the THz beam and the probe beam [Section 2.1.2].

3.3.2 Optical balanced detection assembly

To sensitively detect such small phase changes of the probe ($\ll 1^o$), balanced detection technique is used. The detection setup comprises of a lens (Thorlabs LA1172-

B-ML), a quarter wave plate (QWP) (Thorlabs AQWP05M-98), a Wollaston prism (Thorlabs WP10-B), and a balanced photodetector (Thorlabs PDB210A/M) consisting of two photodiodes with a summation and a subtraction (balanced) channel of the two readings [Figure 3.5]. The lens collimates the probe beam with its spot size roughly equal to the size of the photodiodes active area. In the case of no THz input, a quarter wave plate renders the probe beam circularly polarised. The Wollaston splits the probe beam into two beams with orthogonal polarisation; a circularly polarised probe gives two beams of equal magnitude which hit the left and right photodiodes. Therefore, the balanced channel of the photodetector subtracting the two photodiodes' signals reads a zero value.

When a THz pulse is present, the probe is instead elliptical prior to and after the QWP due the electro-optic sampling-induced phase shift. Consequently, the outgoing two beams from the Wollaston prism are not equal in magnitude anymore and the balanced channel reads a non-zero value. Planken et al. derived the expression of the intensity difference between the two beams ΔI

$$\Delta I(\alpha, \theta) = I_0 \frac{\omega n^3 r_{41}}{2c} E_{THz}(\cos \alpha \sin 2\theta + 2 \sin \alpha \cos 2\theta) \qquad (3.1)$$

I_o is the probe beam total intensity ω is the probe central frequency, n is the refractive index of ZnTe for probe wavelength, r_{41} is the electro-optic coefficient, c is the speed of light, E_{THz} is the THz electric field, d is the ZnTe thickness. α is the angle between E_{THz} polarisation and ZnTe (001) axis, and θ is the angle between probe beam polarisation and ZnTe (001) axis. Setting the chopper at 2.5 kHz on the pump path results in the lock-in amplifier selectively reading signal only from THz-induced probe phase change.

The design of the balanced detection dictates how sensitively we can detect the THz electric field. The QWP should be achromatic, with uniform phase retardation across the probe wavelength range. The Wollaston prism extinction ratio (ours is 100,000:1) should limit the smallest detectable polarisation change. The Thorlabs balanced photodetector was purchased after several considerations. First, industry-built balanced photodetectors are more reliable in getting two photodiodes having equal performance or sensitivity. Both photodiodes should give roughly the same voltage response for the same amount of light intensities so that the balanced or subtraction reading accurately represents the difference between the two split probe beams. Second, the Thorlabs photodiodes have big active areas, which pro-
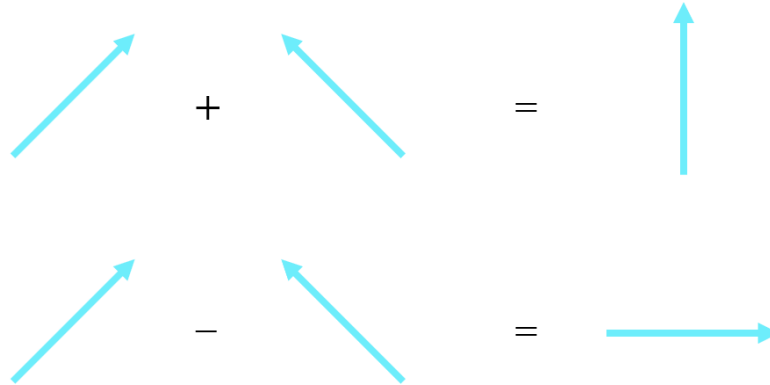
Figure 3.7: Illustration polarisation-resolved THz measurements, performed by acquiring THz signals when 1st wire grid polariser is $+45^o$ and -45° to the 2nd polariser. The blue arrows represent E_{THz} polarisation after the 1st wire-grid polariser. Summation gives a THz polarisation along the 2nd polariser, which is vertical, while subtraction gives the perpendicular component

vide a higher damage threshold, allowing us to use relatively high probe intensities and make alignment easier. The deciding factor is that it provides monitor channels that read each photodiode output. This allows us to get the ratio of polarisation changes $\frac{\Delta I}{I_o}$ accurately for each data point, which is then converted to a terahertz electric field E_{THz}.

3.4 Polarisation-resolved THz detection

Our setup needs to resolve the polarisation of the emitted THz pulse as many spintronics effects rely on symmetry analysis. At the same time, the THz beam polarisation reaching the detector crystal must be fixed at all time for an accurate conversion of the detected signals to time-domain THz electric field as shown by Equation 3.1. A pair of wire grid polarisers (Purewave PW010-025-100, PW010-025-50) is used for these purposes. Such polarisers are made of thin metallic wires of 10 μm diameter with spacing of 25 μm. E_{THz} with polarisation along the wires is absorbed, whereas the perpendicularly polarised E_{THz} are transmitted. Wire grid polarisers with such spacing and diameter have $> 90\%$ transmittance for $E_{THz}\perp$, while only allow 0.1% transmittance for $E_{THz}\|$ for <3 THz. The two polarisers, 50 mm and 100 mm in diameter, are placed closer to the sample holder and between the 3rd OAP mirror and the 4th OAP mirror, respectively. A motorised rotation stage (Standa 8MR190-2-28-MEn1) controls the orientation of the smaller polariser.

On the other hand, the 100 mm polariser is fixed to ensure that E_{THz} arriving at the detector is always polarised normal of the optical table.

Polarisation-resolved THz detection acquires data for both $+45°$ and $-45°$ orientation of the 1st polariser relative to the 2nd polariser. Summation of the two measurements gives the E_{THz} component that is vertical or normal with respect to the optical table, whereas the subtraction results in the horizontal or in plane polarisation. Figure 3.7 illustrates how the polarisation of E_{THz} is deduced.

3.5 Noise suppression techniques

Balanced detection technique Balanced detection is the key noise suppression technique since the earliest THz-TDS setups were invented. The main advantage of this technique is that it eliminates probe intensity fluctuation noise. As the detection is derived from subtracting two beams originated from the same laser source, the total intensity of the probe ideally does not affect the subtraction/balanced reading. This is especially advantageous for users of amplified femtosecond laser where the intensity fluctuation as large as 1% over 24 hours. The technique relies on two photodiodes and each of the transimpedance amplifiers being identical. Common Mode Rejection Ratio (CMRR) quantifies the performance of a balanced detector in cancelling noise that are common to the both channels. Thorlabs PDB210A/M has CMRR of 40-50 dB, which means that common noise is suppressed by a factor of 100-300. CMRR defines the noise suppression only up to the Wollaston prism. Any noise appearing between the Wollaston prism and the photodiodes needs to be taken care of. Among obvious sources we find are dusts that scatter one of the two beams, or strong beam drifting that causes beam clipping at the active areas of the photodetectors. To minimise this, the balanced detection assembly is enclosed to ensure clean environment. Moreover, all the assembly components are robustly secured in a cage system to prevent unwanted movements or relative vibrations during regular adjustments of the optics.

Chopper + lock-in amplifier Lock-in detection technique is used to reject any noise with a frequency different than the signal repetition rate. An optical chopper is used to selectively define the frequency of our signals. The chopper frequency reference is fed from the regenerative amplifier of the laser (5 kHz) and then it is halved. Ideally, the signal repetition rate should be as high as possible for faster

acquisitions with acceptable noise levels. However, Nyquist theorem constraints the signal repetition rate to be at most a half of the sampling frequency and hence 2.5 kHz. By doing this, the noise coming from the probe (5 kHz) is rejected. Using the lock-in amplifier with a time constant of 0.3 s reduces the noise bandwidth from 1 MHz (the photodetector bandwidth) to only ∼3 Hz.

Enclosures and beam blocks   Enclosures are placed to minimise the scattered light reaching the photodiodes. The most critical areas are near ZnTe emitters, near the optical chopper, and surrounding the balanced detector. ZnTe reflects a substantial fraction of the 800 nm pump pulse, and hence beam blocks should be in place to prevent the unwanted 2.5 kHz 800 nm beam from entering the detector. The chopper also scatters the 2.5 kHz beam. As the balanced detector assembly is close to the pump area, an enclosed chamber should isolate the assembly from the rest of the setup. Lastly, a 1 mm thick black PTFE is placed after the ZnTe emitter or after the sample to block the pump residue from propagating to the photodiodes. PTFE is chosen for its high THz transmittance of above 80% at frequencies <2 THz for such a thickness.

Nitrogen box   Water vapour in air absorbs and re-emits THz radiation [139]. This manifests with tails of strong noise in the time domain measurements or absorption dips in the frequency domain. Removing such noise requires an enclosed box surrounding the THz propagation path purged with Nitrogen gas, or pumped down to a lower pressure, to remove water vapour from the environment.

Averaging   Signal averaging reduces noises by a factor of $\sqrt{N}$ for N repetitions. The averaging technique is employed in our setup when the noise level is comparable to the signal. Without averaging, our detector has noise level of $\pm$ 1 μV. By averaging 25 measurements, the noise level can be reduced to as low as $\pm$ 0.2 μV. However, further increasing the number repetitions is likely to have a detrimental effect due to the longer time required by the measurements allowing more beam pointing fluctuations to be captured.

3.6 Data acquisition electronics and software

Here, lock-in amplifier and data acquisition parameters are briefly outlined. The Zurich Instruments HF2LI lock-in amplifier consists of two lock-in amplifiers, one reads the balanced channel and the other reads the monitor channel of one photo-diode. The lock-in amplifier receives 2.5 kHz frequency reference from the chopper (Thorlabs MC2000B-EC and MC1F30), and uses it as first harmonic for signal reading, and the second harmonic 5 kHz for tuning the balanced channel and reading one monitor channel. A LabVIEW user interface controls the movement of the linear stage and acquires the lock-in reading. The lock-in has input voltage limit of 2 V which hinders the use of high probe power. The lock-in time constant is set to 0.2-0.3 s. For the acquisition, the time delay between each data point is set to 0.5 - 1 s to stabilise the low pass filter of the lock-ins, as well as the retro-reflector after moving. The default linear stage step size used is 0.01 mm or equivalent to 66 fs time resolution. One can choose 0.005 - 0.008 mm for 33-53 fs resolution as the uncertainty of the stage is about 0.0005 mm. A movement range of about 1 mm or 6.67 ps is often sufficient in our time-domain measurements. However, if FFT analysis is needed, a longer scan is necessary as FFT resolution is inverse of time-domain range ($\delta f = 1/\delta t$). The recommended range would be > 25 ps for < 40 GHz frequency domain data.

3.7 The setup performance as of November 2019

In this section, the development steps of the setup and the performance as of November 2019 are outlined. The optical table layout was designed using AutoCAD for precise positioning of the optics and other components, as well as beam path length measurement. HeNe low power visible laser (632 nm) was employed for initial rough alignment for the basic optics (i.e. mirrors and lenses). The visible laser was placed at the closest possible point and collinear with the Solstice Ace output. We then used the Solstice output for finer alignment using a safety goggle and a beam viewing card for guidance. We first aligned the THz transmission path for its stronger signal. The 800 nm pump beam was used to predict the THz beam propagation as the THz emission from 2nd order optical rectification follows the pump trajectory. Appendix A discusses in detail the entire process of the initial alignment.

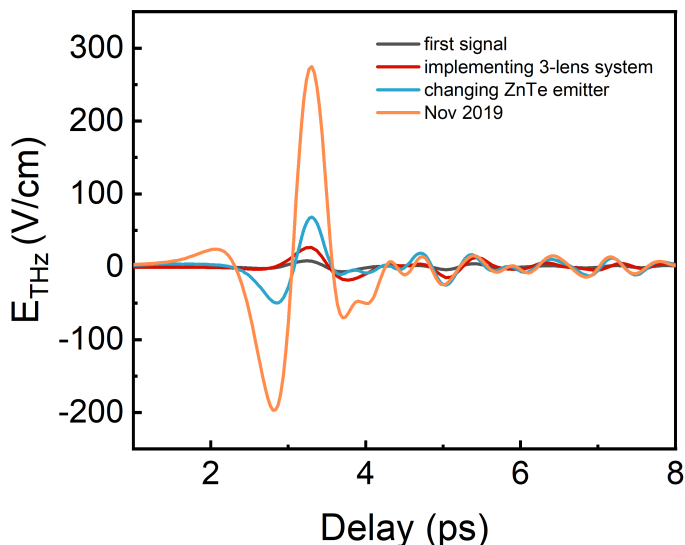Figure 3.8 shows the incremental improvement of the THz transmission

Figure 3.8: THz transmission signal enhancements: (black) the first signal, (red) implementing a 3-lens system for larger beam diameter, (blue) changing the ZnTe emitter crystal, and (orange) fine alignment procedures until November 2019

signal magnitude using pump energy pulse of 0.16 mJ. The first signal (black line) has a peak magnitude of 8 V/cm. The FFT of the time-domain signals show a broadband spectrum up to 2.5 THz, verifying the signal origin from optical recti-fication + electro optic sampling in ZnTe [Appendix B]. Further characterisations of the signal (i.e. the dependence on pump fluence and polarisation, ZnTe orienta-tion) [Appendix B] did not replicate several behaviours described in the literature, which pointed to the imperfect alignment of the setup. Moreover, the initial signal is much lower than the typical values of about 1 kV/cm from ZnTe emitter. To improve the signal magnitude, we examined the optics design and the quality of each components. In the first version of the design, a lens was used to reduce the pump beam diameter passing through the chopper and then hit the ZnTe detector. The incoming pump beam was focused, rather than collimated, which shifted the effective focal points of the emitted THz. Moreover, the beam diameter at the ZnTe was about ∼3 mm, while for optimised signal strength the entire ZnTe area of 10 × 10 mm^2 should be all pumped. The small beam diameter also means a high pump fluence (energy/area), which increases the non-linear two-photon absorption in ZnTe and reduce the energy conversion efficiency. The improved design uses a

three-lens system consisting of two convex lenses and a concave lens [Appendix C] ensuring that the pump beam diameter is small enough to pass through the chopper while has diameter of ∼10 mm at the ZnTe. This increased the signal magnitude by three-fold (red line). We further noticed the ZnTe emitter might be defective as green light emission, a by-product of the two-photon absorption, was notably strong and the saturation trend of the THz signal on the pump fluence occurred at a low fluence [Appendix B]. Replacing with a ZnTe crystal from a different supplier further increased the signal magnitude by almost three-fold (blue line) [Appendix D]. Subsequent improvements in the alignment, for instance fine tuning the beam polarisation and beam diameter, the optics position and tilting, were achieved over the course of months while performing experiments using the setup. As of November 2019, the peak signal reached 300 V/cm (orange line), giving signal-to-noise ratio of above 1000.

There were several obvious aspects that could still be improved. First, we shall remove the three-lenses telescope system as such a multiple transmissive optic system is likely to result in astigmatism, reducing the pump peak power. This requires the replacement of the chopper with one with 10 mm blade spacing at 2.5 kHz. We also need to replace the ZnTe crystal used for the detection with a higher quality one from Egorov Scientific. Lastly, a broader pulse-width instead of 40 fs [140, 141] is more desirable for optical rectification in ZnTe which is in low THz frequency spectrum. The pulse width optimisation can be done from the Solstice Ace User Interface. Further improvements of the THz transmission setup are passed down to subsequent users of THz transmission setup, as this thesis focuses on THz emission studies.

Having the THz transmission setup well-aligned ensured that the THz emission alignment only required fine tuning the 800 nm pump beam reaching the sample spot: the two OAP mirrors delivering the THz emission, electro-optic sampling + balanced detection optics are shared for the two setups. Using a spintronic THz emitter glass/Co(10nm)/Pt(3nm), we obtained THz peak signal of 15 V/cm using pump energy of 25 μJ [black line in Figure 3.9]. In the first design, the lens used to reduce the pump beam diameter at the sample led to beam clipping at the 2nd OAP mirror while the beam too focused at the sample. We replaced the lens with a two-lens telescope system consisting of a convex lens and a concave lens for obtaining a collimated beam with a bigger diameter at the sample while avoiding
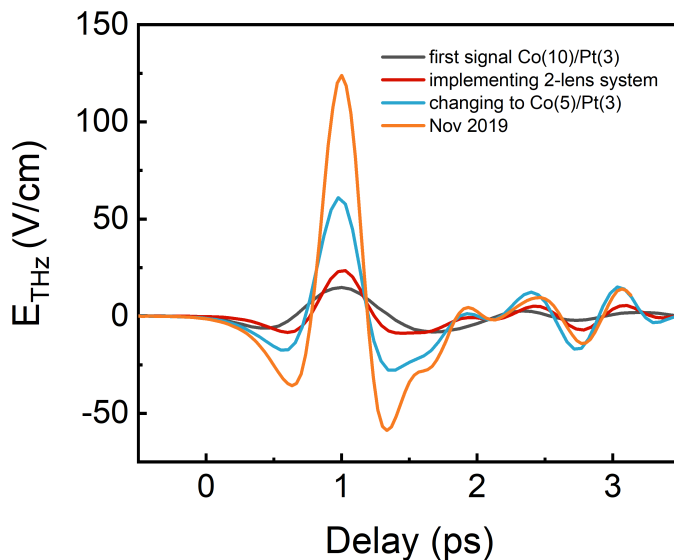
Figure 3.9: THz emission signal enhancements: (black) the first signal, (red) implementing a 2-lens system for larger beam diameter, (blue) changing Co/Pt calibration sample, and (orange) fine alignment procedures until November 2019

beam clipping [Appendix E]. This increased the signal to 25 V/cm with better THz frequency bandwidth, which could be attributed to the larger THz beam diameter giving a better spatial overlap in the electro-optic sampling (red line). We changed our calibration sample to Co(5)/Pt(3) emitting peak THz signal 60 V/cm (blue line). The subsequent alignments when using the setup for months enhanced the signal to 120 V/cm (orange line). This is considerably stronger than reported values [71], demonstrating that our setup is ready to use for research.

The nitrogen purging enabled by an insulating enclosure has improved the signal peak as well. In time-domain, the peak strength increases by 20% with Nitrogen purging due to the absence of spurious water absorption [Figure 3.10(a)]. By performing FFT to the two signals with and without Nitrogen purging, it can be seen that the increase in the signal peak magnitude in time-domain corresponds to the disappearance of water absorption dips across the spectrum [Figure 3.10(b)]. Note that there is a THz peak at $\sim$10 ps, which constantly occurs for strong signals regardless of the samples. This is likely a back-reflected THz pulse by the ZnTe detector considering the path length difference of $\frac{1}{2} \times 10$ ps/(3×10^8 m/s) $\sim$1.5 mm with the main pulse, comparable with the ZnTe thickness.
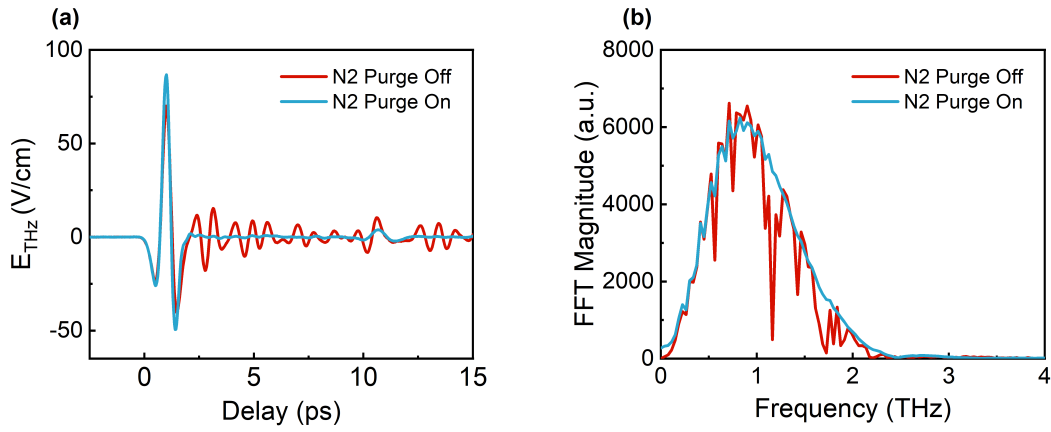
Figure 3.10: (a) Time domain and (b) frequency domain of THz emission with (blue line) and without (red line) N_2 purging
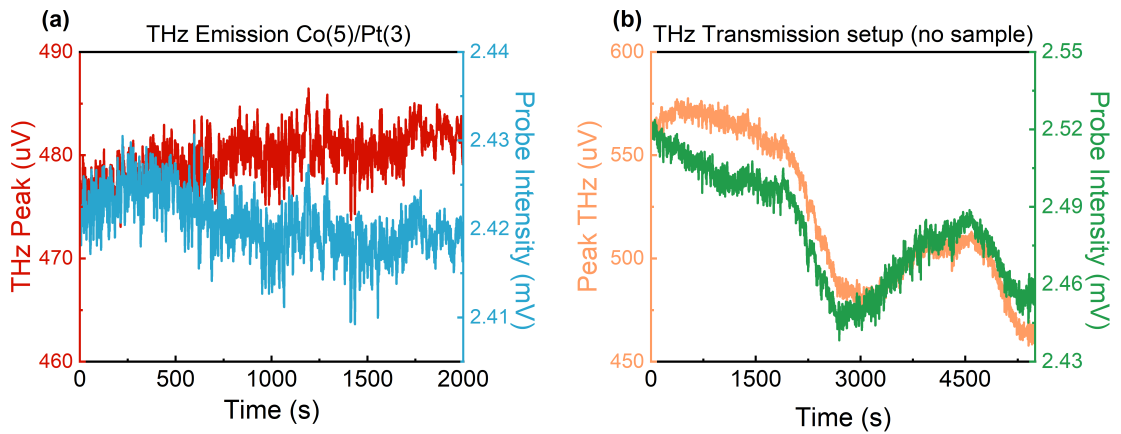

Figure 3.11: Signal stability of THz emission setup (a) in normal circumstances and (b) when the ambient temperature fluctuates

The signal stability of the emission setup has been excellent. By time tracing the THz peak of Co/Pt, the signal drifted by 1-2% for over 30 minutes [Figure 3.11(a)]. The probe is also stable with less than 1% fluctuation. Temperature fluctuations in the environment, however, could significantly disturb the signal stability [Figure 3.11(b)] as observed during heatwave in August 2019 when the temperature controller in our building struggled to maintain a constant temperature.

3.8 Future improvements

3.8.1 Data acquisition card

We use the lock-in time constant of 300 ms, which corresponds to about one data point per second for stabilising the low-pass filter. This however makes the measurements extremely slow when long time-domain range and many iterations are required. Long acquisition time is prone to beam pointing and laser power fluctuations as well as changes in the environment. Moreover, in THz emission measurements, where the laser pulses continuously hit the sample, long measurements accelerate sample degradation.

One solution is to replace the lock-in amplifier with a data acquisition (DAQ) card [142]. This device digitises the analog signal of each pulse. The fast sampling rate of 1 MS/s means that it can sample every pulse received by the photodiodes; a sampling time of 10 ms of the DAQ card gives an averaging of 25 pulses. Such a speed enables much faster acquisition time than lock-in, while providing a slightly better SNR. Hence, a DAQ card is highly recommended when long scans are necessary.

3.8.2 Balanced heterodyne detection

The current setup that uses a 1 mm thick crystal of ZnTe as the detector allows for a sensitivity of 0.1 V/cm, which may hinder the detection of many inherently weak spintronic effects. While increasing the thickness of the detector crystal theoretically enhances the sensitivity, the stronger absorption and phase mismatch of the incoming THz pulse inside the crystal offset the signal enhancement [Figure 3.6]. A maximum thickness of 2 mm for ZnTe seems to be the consensus.

Recent reports demonstrate a sensitivity enhancement by manipulating

the phase retardation by the QWP instead [143, 144]. In earlier discussions, the balanced detection assembly sets the probe beam to have circular polarisation when there is no THz pulse. The balanced signal output is then linearly proportional to the THz electric field. The newer technique instead sets the probe beam to be slightly elliptically polarised with few degrees of phase offset, the phase induced by EOS is then substantially enhanced with a quadratic term. This technique can enhance the signal by up to an order of magnitude.

There are several modifications to employ this heterodyne balanced detection technique. The non-linear contribution needs to be eliminated for accurate conversion of the raw signal to THz electric field. This can be done by subtracting the sampling when using $+\phi$ phase retardation with the one with $-\phi$. A motorised polariser holder is needed to reliably switch between $+\phi$ and $-\phi$ for each scan. Moreover, the elliptical probe results in a huge power difference between the two beams after the Wollaston prism. Hence, a variable attenuator should be placed along the path of the stronger beam to equalise the two intensities reaching the photodetector.

Despite the apparent advantage, implementing the heterodyne balanced detection adds more complications in our setup. Measurements will take twice longer with an additional electronic instrument involved. Unless the QWP and its motorised polariser holder is perfectly orthogonal with the probe beam, rotating a QWP can modify the beam pointing which renders the subtracted data unreliable. Moreover, placing the variable attenuator adds an additional noise source that is uneven for the two beams, which is something to avoid in balanced detection. Implementing the heterodyne detection should only be considered for detecting extremely weak THz emission.

3.8.3   Intense THz generation using Mg:LiNbO3 or organic crystals

ZnTe meets most requirements for efficient optical rectification: high electro-optic coefficient, low THz absorption lower than phonon absorption <5 THz and good phase matching for 800 nm. Its limiting factor comes from the relatively low bandgap of about 2.5 eV. This leads to strong two-photon absorption which gives saturation trend for fluences roughly above $1\,\mathrm{mJ/cm^2}$ [Section B.0.3]. THz peak field from ZnTe

of the order of 1 kV/cm is sufficient for linear THz transmission experiments. Much stronger THz fields of about 100 kV/cm open more opportunities for THz spintronics. For instance, the magnetic field component of the THz pulse can resonantly excite antiferromagnetic dynamics [58] and the electric field component can induce high electric current density in metals triggering spintronic effects [145]. Having an intense THz source will allow experiments replicating typical microwave spintronic studies, but in a much higher frequency domain.

Mg-doped $LiNbO_3$ has been the most popular intense THz pulse emitter for table-top setups [81]. This material meets all the requirements, except the phase matching. The phase mismatch can be solved by tilting its pulse front, which requires a diffraction grating, and by making the out-coming surface of the crystal tilted with respect to the pump k-vector [81]. The crystal can reach a peak THz pulse of >1 MV/cm using pump energy per pulse of 1 mJ [146] and even higher if the crystal is cooled down to ∼100 K [147]. Using an Mg:$LiNbO_3$ is ideal for measurements in the low THz frequencies below 2 THz.

Organic crystals provide alternatives for broader THz bandwidths. DAST, DSTMS, and OH1 have bandwidth of 3-4 THz [148, 149]. These crystals have extremely high r_{41}, but sizeable THz absorption. Hence, typical THz organic crystals have thickness of few hundreds μm. DAST and DSTMS crystals efficiently emit THz of about 0.5 MV/cm.mJ for pump pulse central wavelength of 1100 and 1300 nm. Topas-Prime is hence needed as the pump source. Alternatively, the organic crystals can still emit strong THz pulse of 0.1 MV/cm.mJ at the 800 nm Solstice Ace output [150]. However, these crystals have lower damage thresholds than Mg:$LiNbO_3$, which hinder these organic crystals to achieve an electric field pulse peak of 1 MV/cm.

3.9 Summary

This chapter describes the design and the process of building a THz time-domain spectroscopy setup using an amplified Ti:Sapphire femtosecond laser. The setup is designed to perform both THz transmission and THz emission spectroscopy measurements. The THz source of the THz transmission setup is a ZnTe crystal that emits a broadband THz pulse by optical rectification of the femtosecond optical pulse. Both setups use the same detection assembly that relies on electro-optic sampling process in another ZnTe crystal to construct a time trace of a THz broadband

pulse. The considerations in designing setup, determining the electronic and optical instruments, and the steps for the optical alignment are outlined.

The THz transmission setup attains 300 V/cm signal using 0.16 mJ energy per pulse without a sample, which corresponds to signal-to-noise ratio of 1500:1. We use a Co/Pt thin film bilayer deposited on a glass substrate as our calibration sample and we detect a peak signal of 120 V/cm using 25 μJ per pulse, higher than many reported THz setups in the literature. Potential improvements for the setups include simplifying beam shaping optics and employing a data acquisition card instrument. Moreover, utilising an intense THz source or a new highly sensitive balanced detection technique may enable performing new types of experiments.

Chapter 4

Picosecond Spin Seebeck Effect in Ferrimagnetic YIG/Pt

In recent years, a plethora of SSE studies in $Y_3Fe_5O_{12}$(YIG)/Pt have been reported, mainly focusing on understanding and characterising the underlying mechanisms of magnonic transport [41, 127, 131, 151–153]. The common geometry used is the longitudinal spin Seebeck effect (LSSE) where the temperature gradient is along the YIG thickness. As outlined in Chapter 2, the contributions of the LSSE can originate from the bulk and/or from the interface [73, 120, 154]. When electronic techniques are used to generate the thermal gradient via Joule heating both bulk and interface contribute since the temperature varies not only across the interface, but also through the thickness of the ferrimagnet [131].

Only recently, experimental studies isolating the interfacial contribution of the LSSE have been made possible by using ultrafast laser techniques [72, 155]. In this case a high-power femtosecond optical pulse is absorbed by the non-magnetic metal (NM) layer and the effective electron temperature rises significantly. In the first 50-100 fs, the highly non-equilibrium electron system thermalises via electron-electron scattering, and its energy distribution follows Fermi-Dirac function with an elevated temperature [72]. The effective magnon temperature, however, barely increases due to the transparency of the YIG to the wavelengths of the optical pulse. This leads to a significant difference between the effective electron temperature in the NM and the magnon temperature in the ferrimagnet, leading to a strong LSSE. The interfacial LSSE dominates in this case because the temperature gradient is significant only at the interface and occurs within a short time period, hindering
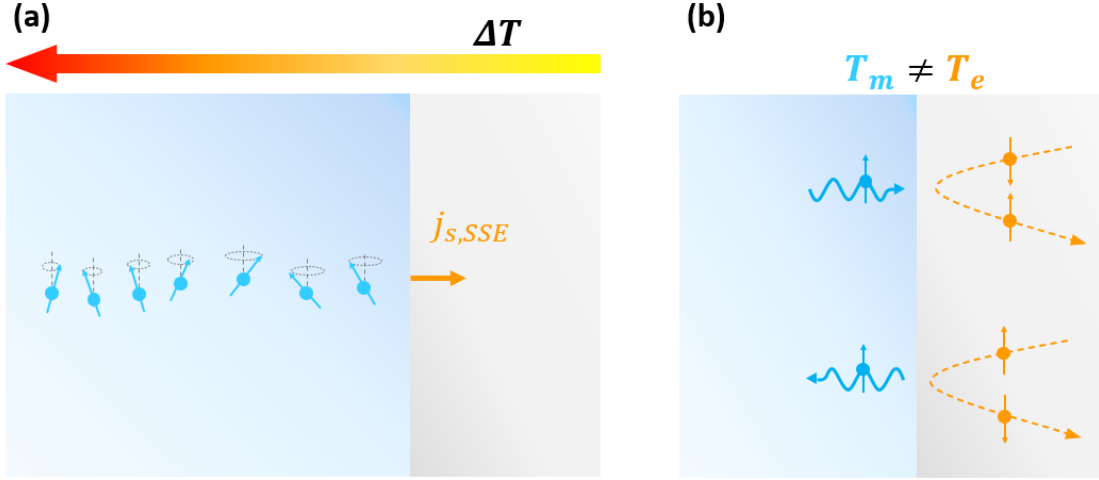
Figure 4.1: An illustration comparing (a) bulk SSE and (b) interfacial SSE, where
the former involves magnons (and phonons) propagation while the latter can be
interpreted as interfacial inelastic spin-flip electron scatterings that induce magnon
creation or magnon annihilation

a build-up of a temperature gradient in the bulk of YIG. The effective electron
temperature subsequently reaches equilibrium with the phonons after few ps, giving
a temporal variation of the LSSE.

The spin transfer between the YIG and the NM is directly proportional
to the temperature difference between the laser-excited electrons in the NM and the
magnons in the YIG, thus it decreases as the electrons thermalise with phonons. This
generated spin-current is converted in the NM into a charge current via the inverse
spin Hall effect, which leads to an electro-dipole radiation in the THz frequency
domain [156]:

$$E_{THz}(\omega) = \frac{Z_0}{n_i(\omega) + n_o(\omega) + \int_0^d Z_0\sigma_{Pt}(\omega)dz}\lambda_s\Theta_{SH}ej_s(\omega) \qquad (4.1)$$

Z_o is the free space impedance, σ_{Pt} is the electrical conductivity of Pt, d
is the thickness of Pt, λ_s is the spin diffusion length Θ_{SH} is the spin Hall angle of
Pt, e is the electron charge. We detect the THz emission via electro-optic sampling
technique and obtain a direct measure of the interfacial contribution of the LSSE.
The earliest experiment on the picosecond LSSE using THz emission spectroscopy
demonstrated that the activation time of the picosecond LSSE is <100 fs, owing
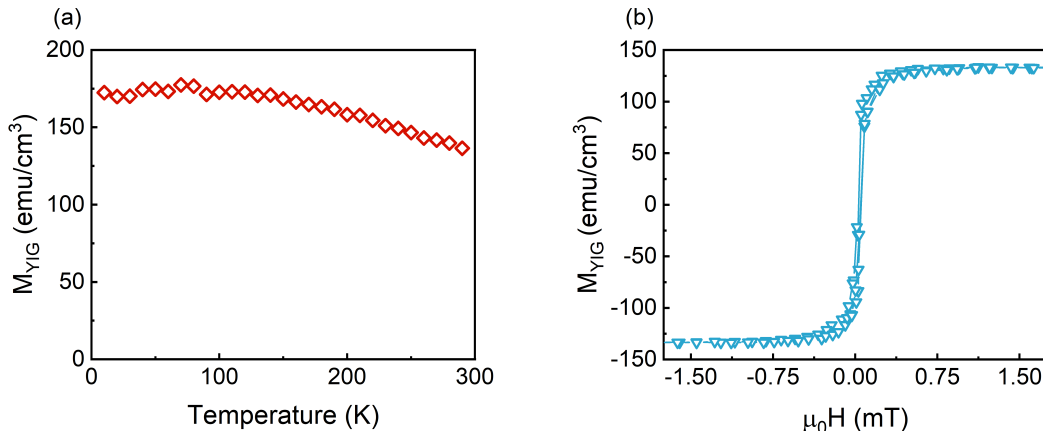
Figure 4.2: (a) Magnetisation vs temperature and (b) magnetisation vs external field trend of GGG/YIG measured using SQUID magnetometry

to the fast dynamics of the spin susceptibility of YIG and Pt [72]. It was shown that the time-domain profile of the THz emission is the convolution between the temporal evolution of the effective electron temperature and the response function of the electro-optic sampling crystal [Section 2.1.2].

Differently from the previous study [72], which only covered the temperature range from room temperature up to the Curie temperature of YIG (550 K), this chapter presents a study on the picosecond LSSE in YIG/Pt at low temperatures. The temperature dependence of the picosecond LSSE in YIG/Pt between 10 K to RT differs from previous reports of low frequency LSSE measurements. The excitation mechanism of the picosecond LSSE excludes the role of the suppressed thermal magnons in the YIG and the magnon propagation length variation, which should contribute to only the bulk SSE. The simpler phenomenology allows an analysis of spin-transport properties in the Pt and at the interface. Moreover, we identify a contribution to the THz emission that does not have a magnetic origin. The contribution likely comes from the bulk GGG substrate via a non-linear electro-optic effect. From this point, the term 'PSSE' refers to the picosecond LSSE.

4.1 Sample characterisation and fabrication

The material under study is a commercial polished Yttrium Iron Garnet or YIG with a thickness of 100 nm grown on a $Gd_3Ga_5O_{12}$ or Gadolinium Gallium Garnet (GGG) substrate with (111) orientation. The sample area is 5×5 mm^2 and the
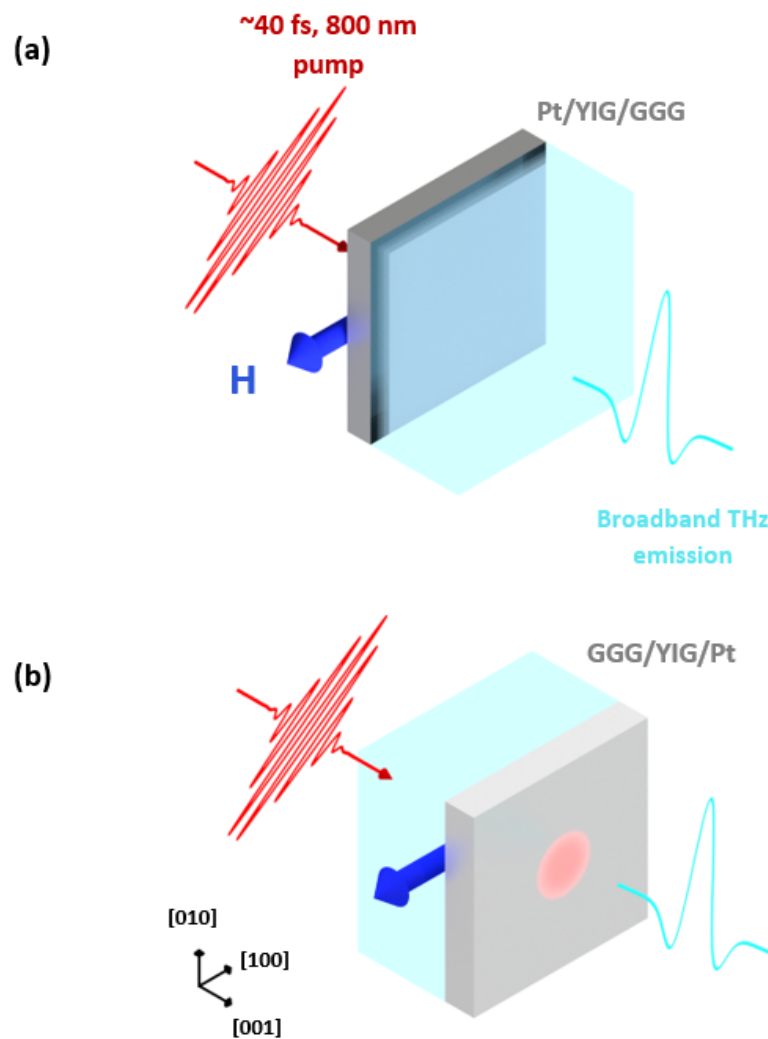
Figure 4.3: Illustration of the THz emission experiment using 40 fs optical pulse
with central wavelength of $\omega = 800$ nm. The ultrafast build-up of the interfacial
temperature difference injects pure spin current, which is converted to THz charge
current by the ISHE. Two configurations used in the experiment (a) GGG substrate-
side pumping (b) Pt-side pumping

polished surface has a roughness of ± 1 nm. Figure 4.2 shows the superconducting quantum interference devices (SQUID) measurements of YIG performed using the MPMS system at the Maxwell Centre. YIG is an uncompensated ferrimagnet with a Curie temperature of $\sim$550 K [157]. The magnetisation varies from $M_s = 172$ kA/m at 10 K to $M_s = 136$ kA/m at RT [Figure 4.2(a)]. YIG behaves like a soft ferromagnet with a very low coercivity of $H < 10$ Oe [Figure 4.2(b)].

  The deposition of Pt (5 nm) was performed in the Device Material Group in the Department of Materials Science & Metallurgy by Lauren McKenzie-Sell. Before the deposition, the YIG was cleaned using piranha etching [158,159] procedure ensuring a good quality of the YIG surface. The 5 nm thickness was chosen to maximise the ISHE signal, taking into consideration the spin diffusion length of Pt, the electrical resistivity and morphology uniformity [160]. THz emission experiments of the PSSE were performed in two different configurations, shining the optical pulse either from the GGG side or from the Pt side. The pump pulse has a central wavelength of 800 nm, which coincides with a high transparency window for both YIG and GGG (the transmittance of GGG/YIG is $\sim$80%) [161,162]. In the limit of a metallic layer thickness much thinner than the optical wavelength, its absorbance is strong and independent on the layer electrical resistivity ($A \approx \frac{n_{YIG}}{(n_{YIG}+n_o)} \approx 0.69$ for substrate-side pumping and $A \approx \frac{n_{no}}{(n_{YIG}+n_o)} \approx 0.31$ for Pt-side pumping [163,164] where $n_{YIG} \approx 2.2$ [161] and $n_o = 1$), owing to multiple reflections that constructively interfere [163]. Unless stated otherwise, the experiment was set to detect the THz electric field polarised along the normal to the optical table [Figure 4.3]. The default incident pump fluence used in the experiment is 0.43 mJ/cm^2.

4.2 Field dependence and ISHE symmetry analysis at RT

To verify that the THz electric field emission (E_{THz}) from YIG/Pt is indeed due to PSSE, field-dependence measurements and a symmetry analysis were performed. Figure 4.4(a) shows that the polarity of $E_{THz}||[010]$ (red lines) is reversed by reversing the direction of the external field from +0.25 T (solid red line) to -0.25 T (dashed red line), whereas $E_{THz}||[100]$ (blue lines) is unaffected. Moreover, Figure 4.4(b) shows that the polarity of $E_{THz}||[010]$ reverses when the pump pulse hits the sample from the substrate-side (green line) or the Pt-side (orange line). According to the ISHE, the generated electric current ($\mathbf{j_e}$) is parallel to the the cross product of
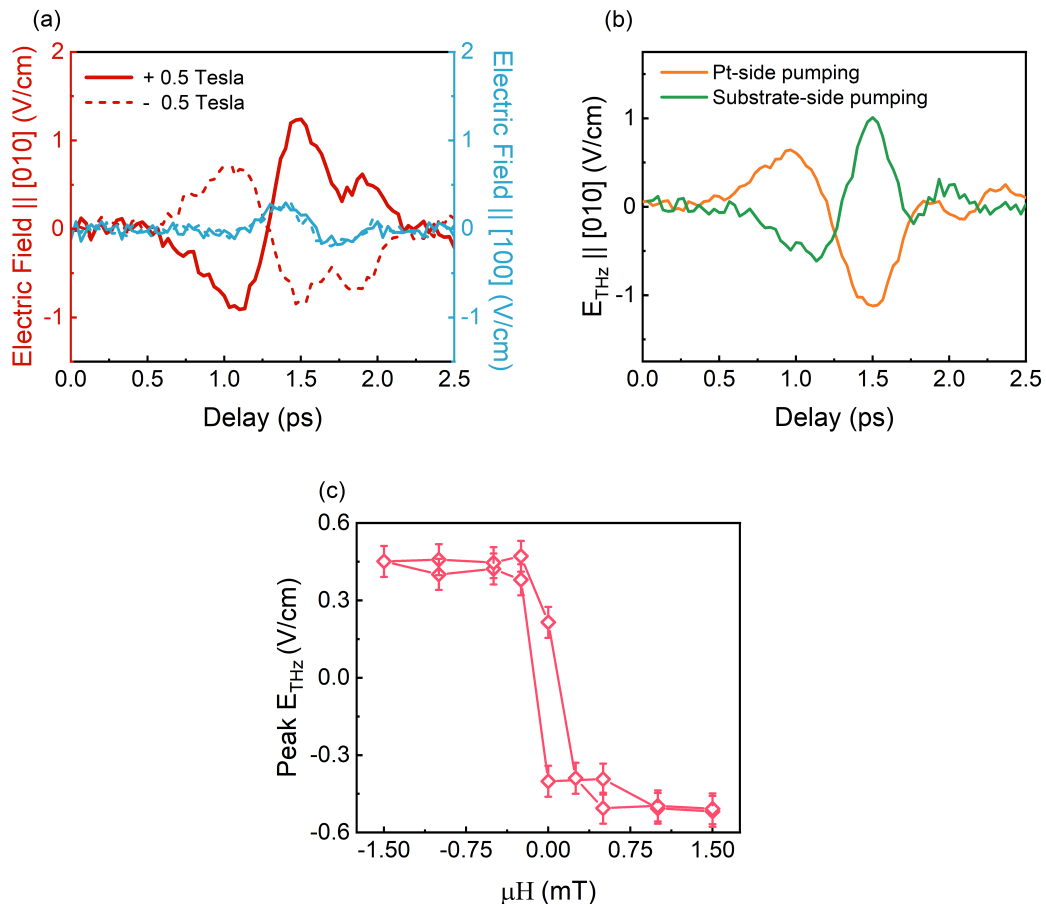
Figure 4.4: (a) $E_{THz}||[010]$ and $E_{THz}||[100]$ at $+0.25$ T and -0.25 T external field
(b) and $E_{THz}||[010]$ for the two configurations represented in Figure 4.3. These
measurements were taken at RT without optical windows using an absorbed fluence
of 0.28 mJ/cm^2 (c) Hysteresis loop of $E_{THz}||[010]$ taken at RT using absorbed fluence
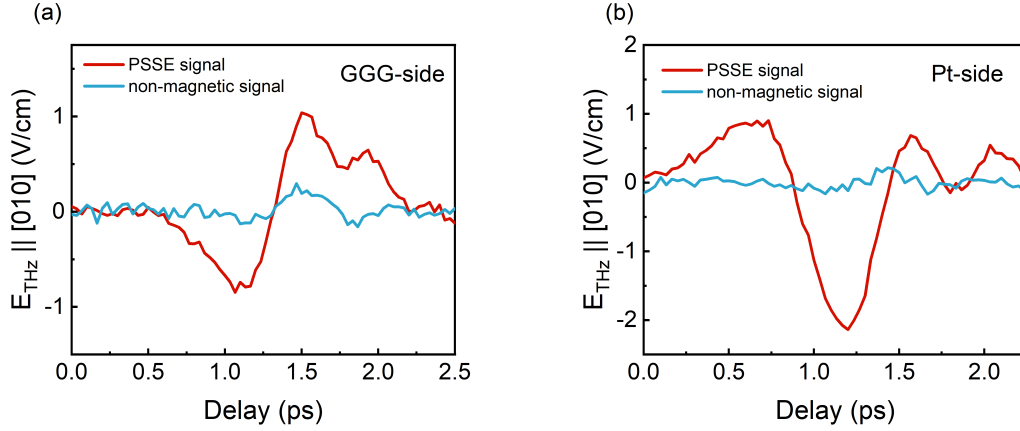0.09 mJ/cm^2

Figure 4.5: Magnetic and non-magnetic origin contributions of $E_{THz}||[010]$ taken at 10 K for (a) GGG-side pumping and (b) Pt-side pumping

the spin polarisation σ (along $\mathbf{M_{YIG}}$ [100]) with the spin current direction $\mathbf{j_s}$ which is along the normal to the interface [001] $[\mathbf{j_e} \propto \mathbf{j_s} \times \sigma]$. Lastly, $E_{THz}||[010]$ exhibits hysteresis behaviour [Figure 4.4(c)] replicating the YIG spontaneous magnetisation shown in Figure 4.2(b).

We should note that there is also a signal that does not have a magnetic origin. This can be isolated by separating the component of the THz emission that is odd with respect to the external field $[(S(+H) - S(-H)/2]$ from the one that is even $[(S(+H) + S(-H)/2]$ [Figure 4.5(a)]. While it has been established that the magnetic origin signal corresponds to the PSSE, the non-magnetic signal in YIG/Pt has not been reported previously. By pumping the sample from the Pt-side, the non-magnetic signal is barely detected [Figure 4.5(b)], suggesting that it originates in the bulk GGG/YIG. The analysis of the non-magnetic signal is covered at the end of the chapter while next sections will focus on the PSSE in YIG/Pt.

4.3 Temperature dependence of PSSE

Figure 4.6 shows the temperature dependence of the PSSE in YIG/Pt from RT to 10 K for (a) substrate-side pumping and (b) Pt-side pumping. In both cases, the PSSE signal monotonically increases by a factor of three. Pumping from the substrate side results in a more rapid increase below 100 K than the Pt-side pumping. Subsequent analyses is based on the data relative to the Pt-side pumping measurements [Figure 4.5(b)].
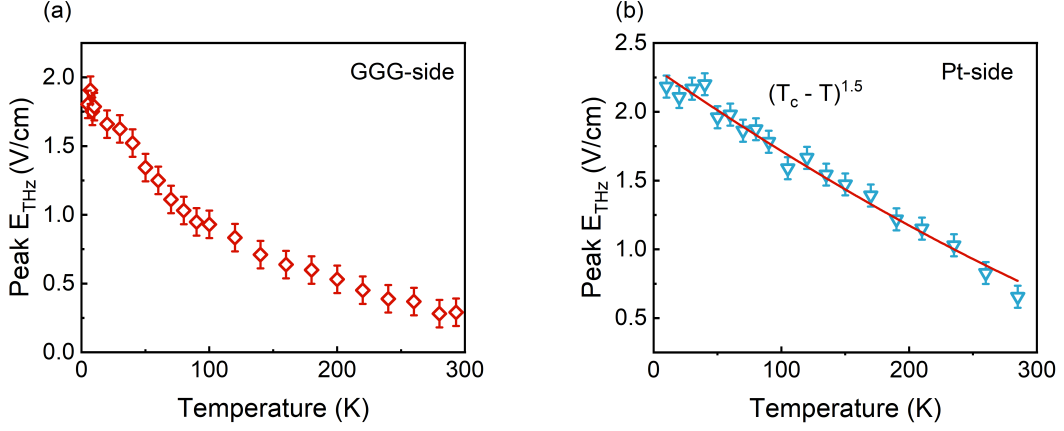
Figure 4.6: Temperature dependence of PSSE signal measured by (a) substrate-side
pumping and (b) Pt-side pumping

The monotonic increase of the PSSE in YIG/Pt for lowering temperature
agrees with the previous PSSE YIG/Pt experiment from RT to Curie Temperature
$T_C = 550$ K [72]. In the study, the trend was fitted with an exponential function with
decay constant $\alpha = 2 - 2.5$, consistent with other measurements of the bulk SSE in
YIG/Pt using DC techniques [72]. In our case, fitting (red line Figure 4.6(b)) gives
a decent agreement with a slightly lower decay constant of $\alpha = 1.5$, which suggests
that the mechanism determining the temperature variation of the PSSE is the same
both above and below room temperature.

However, the low temperature behaviour of the PSSE that we measure
differs substantially from that measured using DC techniques. In previous studies
of the bulk SSE, the signal increment is attributed to the lengthening of the magnon
propagation length l_m in the μm range in the bulk YIG, which influences the spin
current magnitude arriving to the Pt [131]. Such an interpretation cannot apply
to the PSSE. The ultra-short time window of the laser-induced rapid change in
electron temperature, which only lasts for 1-2 picoseconds, does not allow the build-
up of a thermal gradient in bulk YIG. The phonons that carry the thermal energy
in YIG propagate at the speed of sound $\sim 10^4$ m/s, which makes the picosecond
measurement only sensitive to bulk contributions originating in a few nm of YIG
in contact with the interface with Pt. It follows that changes in l_m should not be
probed in the PSSE measurements.

Moreover, the PSSE trend at low temperatures is in direct contrast with

the bulk SSE, where the signal peaks at 100-200 K and decreases to zero at $T \sim 0$ K [131, 132, 165]. In these studies, the propagating thermal magnons and phonons carry the pure spin current, and the populations of both carriers decrease to zero at very low temperatures where the thermal energy reduces to zero [see Bose-Einstein function Equation 2.29]. As the number of spin carriers is less in the bulk magnet the SSE signal is consequently suppressed.

On the other hand, the PSSE occurs due to the spin-dependent scatterings of the laser-excited electrons in Pt at the YIG/Pt interface. The inelastic electron scatterings at the interface induce magnon creation and annihilation in the YIG [135, 166]. Reciprocally, magnon scatterings at the YIG surface induce electron spin-flips. The difference between effective electron and magnon temperature at the interface renders a net flow of carriers. The flow across the interface has a net spin angular momentum [167] as the spin-dependent chemical potentials of YIG makes the probabilities of spin up-down and spin down-up scattering events unequal. Therefore, in the PSSE, the electrons are the spin carriers and their population is directly determined by the absorbed laser energy, not by the thermal energy determined by the environmental temperature. Using a crude estimation and assuming that all the absorbed energy is contained within the electron system until reaching its internal thermal equilibrium [Section 2.2.1], the increase of the effective electron temperature is [168]

$$\gamma(T_e^2 - T_0^2) \approx U_{abs} \tag{4.2}$$

$$\Delta T_e = T_e - T_0 \approx \left(\frac{2U_{abs}}{\gamma} + T_0^2 \right)^{0.5} - T_0 \tag{4.3}$$

γ=750 $\mathrm{Jm^{-3}K^{-2}}$ [169] is the proportionality constant of electronic heat capacity in Pt, $C_e = \gamma T_e$, U_{abs} is the absorbed fluence, T_0 is the initial sample temperature or ambient temperature, T_e is the effective electron temperature. Equation 4.3 overestimates ΔT_e [Appendix G] because it neglects the electron-phonon coupling that exchanges heat with the phonon system during the electron thermalisation in the first 200 fs [72]. To take this effect into account a constant factor is introduced in Equation 4.3 representing the electron-phonon heat transfer in the first 100 fs [Appendix G].

The subsequent electron-phonon coupling reduces T_e while the overall en-
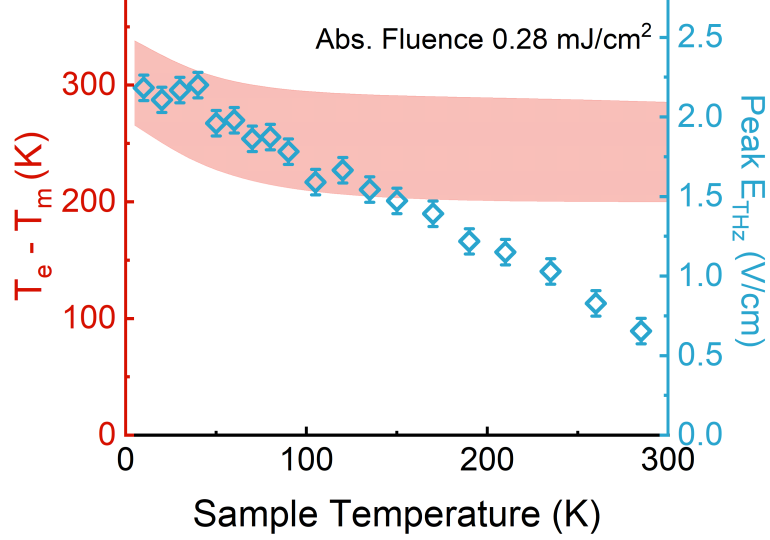
Figure 4.7: (red-shaded area) Calculated ΔT_e for absorbed pump fluence 0.28 mJ/cm^2 in the time range of 0.7-1.3 ps after laser excitation (b) the experimental data of E_{THz} using the same fluence across for sample temperatures 5 - 300 K

ergy of the system is conserved

$$\gamma T_e \frac{dT_e(t)}{dt} + g_{e-ph}(T_e(t) - T_{ph}(t)) = 0 \tag{4.4}$$

$$\frac{1}{2}\gamma(T_e^2 - T_0^2) + (U_{ph}(T_{ph}) - U_{ph}(T_0)) = U_{abs} \tag{4.5}$$

T_{ph} is the phonon temperature, $g_{e-ph} \approx 10^{18}$ Wm^{-3}K^{-1} for Pt [89], U_{ph} is the phonon energy, which can be approximated with the third order Debye function

$$U_{ph} \approx 3Nk_BT_{ph}\left(\frac{T_{ph}}{T_D}\right)^3 \int_0^{T_D/T} \frac{x^3}{e^x - 1}dx \tag{4.6}$$

where $3Nk_B = C_{ph,T\infty} = 2.85 \times 10^6$ J.m^{-3}.K^{-1} [169] is the phonon heat capacity at $T \gg T_D$ and $T_D = 240$ K is the Debye temperature of Pt.

The ΔT_e easily reaches > 100 K thanks to the very high energy density input [red-shaded area in Figure 4.7]. This is in contrast with Joule heating excitation which typically gives a heat gradient of about $\sim$10 K. The extremely high ΔT_e by the femtosecond laser absorption that persists even at ambient temperature of 5 K

means that there is no carrier population quenching as seen in bulk SSE; the PSSE remains strong at low ambient temperatures. Note that for a constant laser energy input, ΔT_e is higher for lower T_0 due to the temperature dependence of the electron and phonon heat capacities. The variation of ΔT_e contributes to the temperature dependence of the PSSE. However, as seen in Figure 4.7, the ambient temperature dependence of ΔT_e alone could not explain the fast increase of the PSSE signal at low T_0.

Apart from ΔT_e, other parameters in Equation 4.1 should be examined. The refractive indices of YIG barely change [170], $\lambda_s/\sigma_{Pt} \approx$ const. [171], $\sigma_{Pt(5nm)}$ weakly decreases on temperature [172], and Θ_{SH} also weakly changes as it is proportional to σ_{Pt} [171]. The remaining parameter is the injected spin current, which can be expressed as [133]

$$j_s(t) = \frac{2N_{int}J_{sd}^2\chi_{Pt}\tau_{Pt}}{A_{int}\hbar^2}S_{YIG}k_B(T_e(t) - T_m(t)) \tag{4.7}$$

N_{int} is the number of localised YIG spins at the interface, A_{int} is the interface contact area, $\hbar$ is the reduced Planck's constant, χ_{Pt} is the spin susceptibility of Pt, τ_{Pt} is the spin-flip scattering time, while T_e and T_m are the effective electron and magnon temperature respectively. The only parameter left that potentially varies with T_0 is the J_{sd}. We conclude that the trend in Figure 4.7 is determined by the temperature dependence of the interfacial exchange coupling J_{sd}. Previous studies based on ferromagnetic resonance have suggested that the interfacial exchange coupling has a temperature dependence of $T^{3/2}$ [173]. However, the authors have underlined the complexities in interpreting data to extract strictly the J_{sd} contribution.

Here, the change of magnon temperature in YIG ΔT_m is assumed insignificant, or $T_m \sim T_o$. Although the phonons in the Pt heat up, it takes two processes for increasing T_m: 1) interfacial heat conduction via phonons, and 2) magnon-phonon interaction in YIG. The interfacial thermal resistance, or Kapitza resistance, hinders the fast propagation of phonons across the interface. The heat transfer rate in insulator/metal interfaces is one order of magnitude smaller than metal/metal interface [74]. The subsequent magnon-phonon interaction that involves exchange interaction has a typical time scale of ~ 1 ps [98] and it is therefore unlikely that this contribution plays a significant role within the time of our measurement ~ 2 ps. Experimental evidence of the slow heat-up of T_m will be presented in Chapter
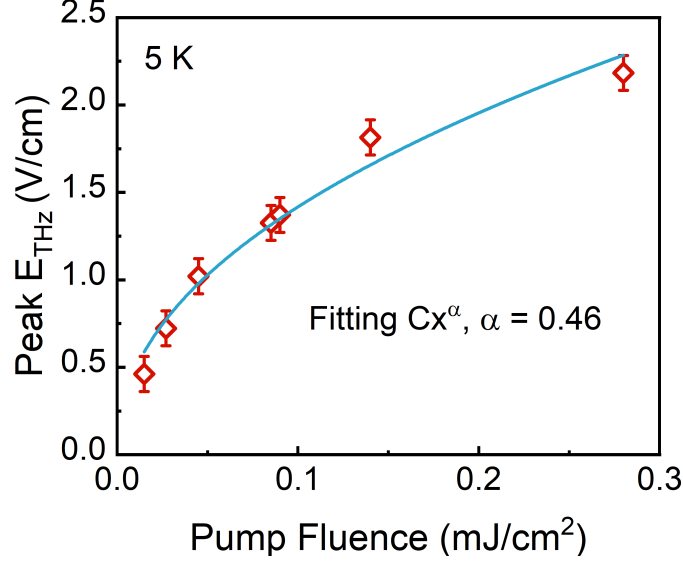
Figure 4.8: Peak PSSE signal dependence on pump fluence at 5 K. The fitting originates from $\Delta T_e \sim const.\, U_{abs}^{0.5}$ for low sample temperatures

6, where the magnetic transition temperature observed using PSSE coincides with the magnetometry data, indicating no substantial magnon heating by the PSSE.

4.4 Pump fluence dependence

Figure 4.8 shows the pump fluence dependence of the PSSE measured at 5 K. The PSSE signal does not follow a linear proportionality with the pump fluence as previously reported [72], and instead the PSSE starts to saturate at a relatively low fluence. As seen from Equation 4.2, the dependence of ΔT_e on U_{abs} is far from linear at low ambient temperatures. The much lower electronic heat energy ($U_e \sim 10^5 - 10^7$ J/m^3 at $T_e \approx 10 - 100$ K) than the absorbed fluence used in the experiment (U_{abs}= fluence/(5 nm) = $5 \times 10^7 - 5 \times 10^8$ J/m^3) means that one can approximate $\Delta T_e \sim U_{abs}^{0.5}$. Fitting $\Delta T_e = CU_{abs}^{\alpha}$ on Figure 4.8 gives α =0.46 which is in a good agreement.

Interestingly, the temperature dependence of the PSSE at the pump fluences 0.026 mJ/cm^2 and 0.28 mJ/cm^2 are similar [Figure 4.9(a)]. Meanwhile, the calculated ΔT_e at 0.026 mJ/cm^2 depends more strongly on the ambient temperature than at 0.28 mJ/cm^2 [Figure 4.9(b)]. The time profile of ΔT_e at 0.026 mJ/cm^2 shows a peculiar behaviour where it decays at a significantly faster rate at low ambi-
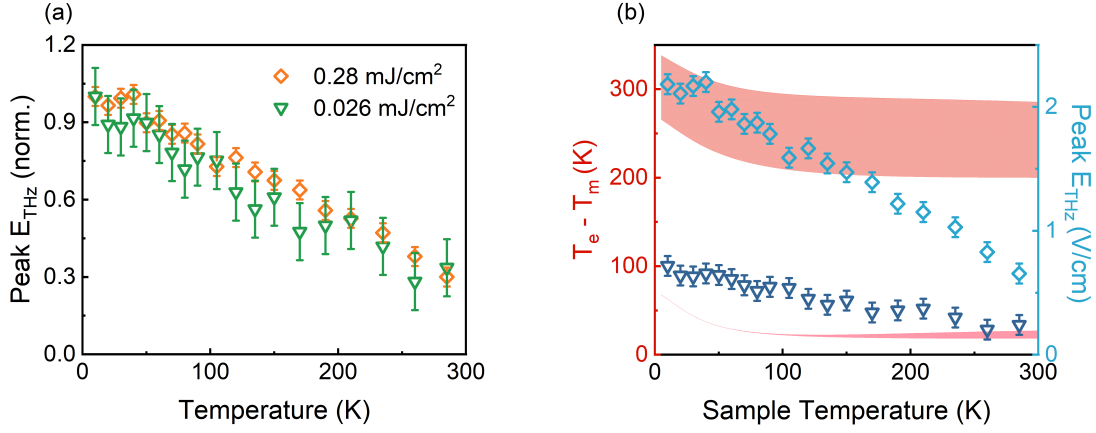
Figure 4.9: (a) Temperature dependence of normalised E_{THz} on two different pump fluences (orange triangle) 0.28 mJ/cm^2 and (green circle) 0.026 mJ/cm^2 (b) a comparison between (red-shaded area) calculated $T_e - T_m$ at 0.7-1.3 ps after excitation and PSSE Peak E_{THz} for (diamond) 0.28 mJ/cm^2 and (triangle) 0.026 mJ/cm^2
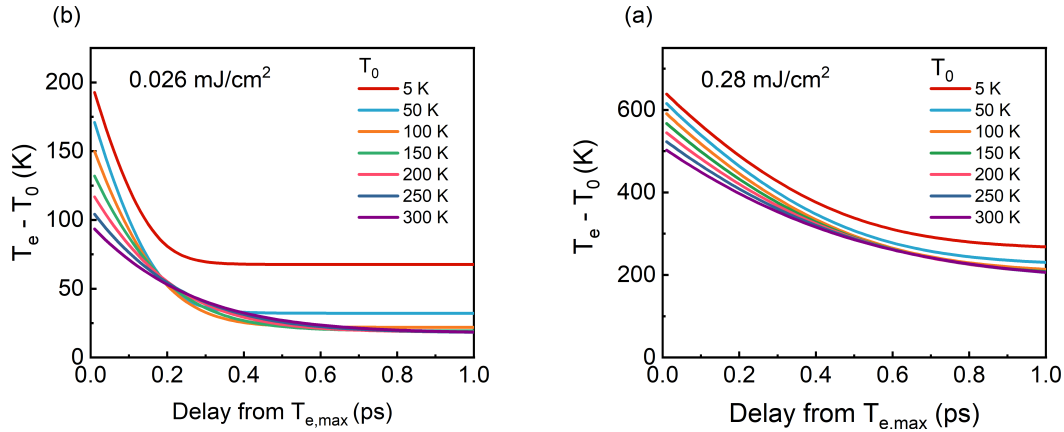
Figure 4.10: Calculated time profile of T_e for different sample temperatures using pump fluence of (a) 0.28 mJ/cm^2 (b) 0.026 mJ/cm^2

ent temperatures [Figure 4.10(a)]. This is true if we assume a constant g_{e-ph} value, however this assumption might not be appropriate. The value of g_{e-ph} that we used for the simulations has been derived for a sample temperature above T_D, where C_{ph} is constant [89]. At $T < T_D$, the number of phonon modes (and hence the phonon heat capacity) varies with temperature, which may affect the electron-phonon coupling. At 0.026 mJ/cm^2, since the energy input is low, T_{ph} remains low and using the value of g_{e-ph} derived for $T > T_D$ might constitute an overestimation. At 0.28
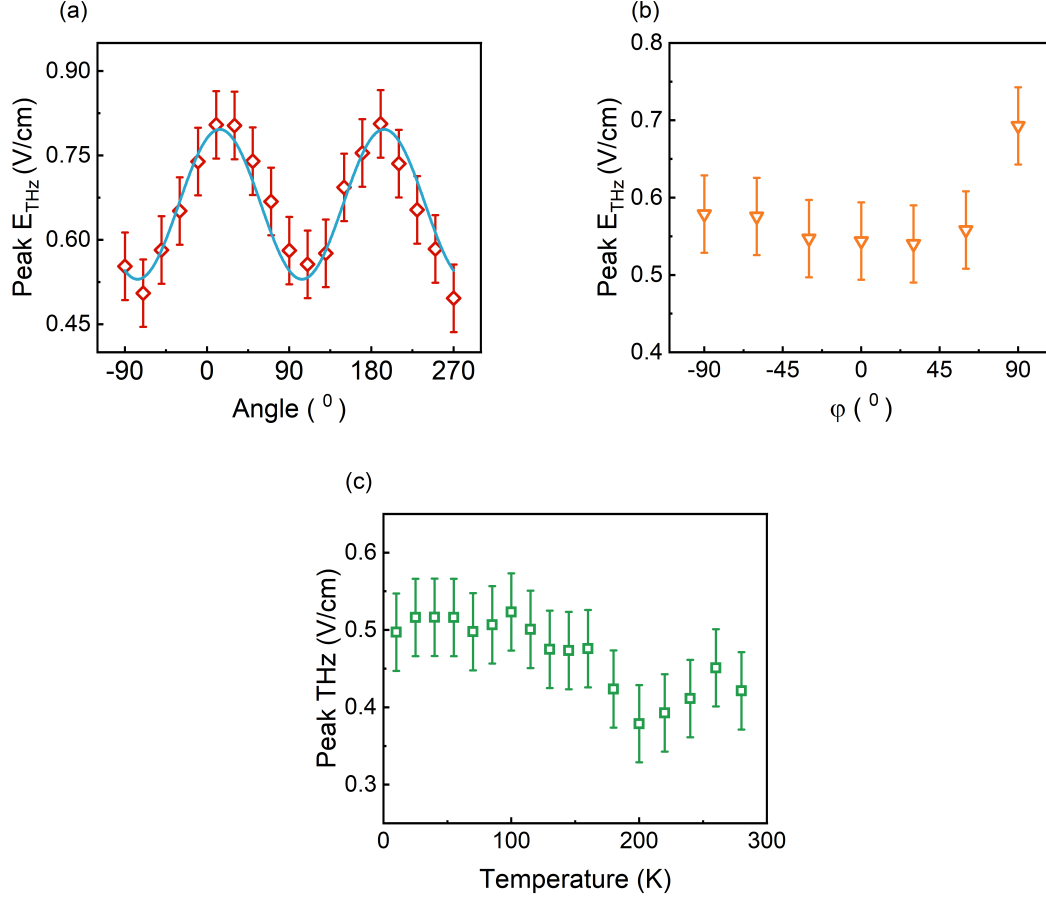
Figure 4.11: Non-magnetic signal dependence on (a) pump linear polarisation varied
using a half waveplate fitted using Equation 4.8, (b) pump ellipticity varied by a
quarter waveplate, and (c) sample temperature

mJ/cm^2, the electron system reaches a very high temperature and quickly heats up
T_{ph} to values closer to T_D, which justifies using the constant value of g_{e-ph}. There-
fore, using the 0.28 mJ/cm^2 data may be more quantitatively accurate in providing
insights on temperature dependence of the PSSE.

4.5 Electro-optic signal in GGG/YIG/Pt

The non-magnetic signal originates from electro-optic effects in the bulk GGG/YIG.
The $E_{THz}||[010]$ that is even in magnetic field shows a clear dependence on the
pump linear polarisation [Figure 4.11(a)]. Past studies have demonstrated optical
second harmonic generation (SHG) in GGG(111)/YIG [174], and therefore optical

Figure 4.12: PSSE signal as a function of pump (a) linear polarisation and (b) ellipticity

rectification (OR) is possible in the structure as both rely on the 2nd order electro-optic constant. The trend in Figure 4.11(a) follows exactly the symmetry of the 2nd order electric polarisability of (111) films [174] (blue line)

$$P_i^{(2)} = \chi_{11}(E_i^2 - E_j^2) + 2\chi_{15}E_kE_i \qquad (4.8)$$
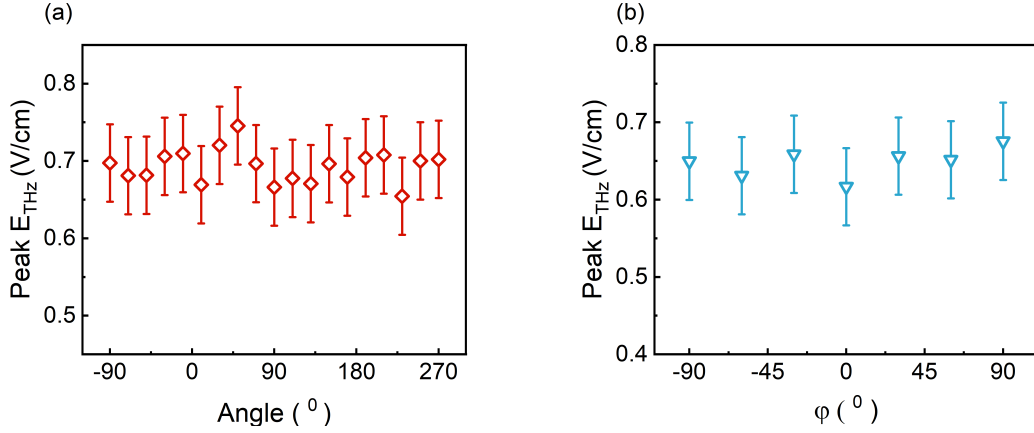
Although GGG itself is centrosymmetric, the lattice mismatch with YIG grown on top induces elastic deformations, gradually changing the lattice parameters of the YIG and breaking the inversion symmetry [174]. The non-magnetic signal is independent on phase retardation/ellipticity as expected [Figure 4.11(b)] since only 3rd order magneto-optic effects with out-of-plane magnetisation typically display such a dependence. The OR signal slightly increases with temperature. Lastly, the magnetic PSSE signal does not depend the pump polarisation [Figure 4.12(a) and 4.12(b)], showing that magnetic-induced dichroism is negligible in our thin YIG sample.

4.6 Discussion

The key result of this chapter is the temperature dependence of the PSSE that strikingly differs from the bulk DC SSE. This is explained with different mechanisms contributing to the spin transfer across the YIG/Pt interface at these timescales. The simpler phenomenology allows us to model the results and extract the temper-

ature dependence of the J_{sd} exchange constant, an extremely important parameter
in determining the magnitude of the SSE, but very hard to isolate with different
experimental techniques.

To the author knowledge, no existing expression of $J_{sd}(T_e, T_{ph})$ have yet to
be derived to and J_{sd} is often treated as an unknown constant variable perhaps due
to its high dependence on the interface quality (i.e. surface roughness) [175]. The
reduction of J_{sd} with temperature that we observe is in line with previous reports,
such as in the temperature dependence of the exchange bias in NiFe/NiO interface
[175], and of the RKKY exchange coupling in a system of FM/NM/FM [176].

4.7   Summary

Using THz emission spectroscopy technique, we measure picosecond spin Seebeck
effect in ferrimagnetic insulator YIG/Pt(5 nm) at a temperature range from room
temperature to 5 K. As the majority of studies in electronic longitudinal spin Seebeck
effect are performed in YIG, our study outlines the distinguishing mechanisms be-
tween the two measurement techniques. We demonstrate that the magnetic-origin
THz emission originates from spin Seebeck effect by performing ISHE symmetry
analysis and laser pump polarisation dependence. Femtosecond-laser excited spin
Seebeck signal is the strongest at the lowest temperature. This is in contrast to
the previous electronic spin Seebeck signal studies where the signal diminishes at
cryogenic temperatures. The Joule-heating generated temperature gradient that
extends to the bulk YIG excites thermal magnons and phonons carrying the spin
current to the Pt layer, and their populations decrease to zero at T = 0 K. In fem-
tosecond excitation, spin current is instead obtained by interfacial spin-dependent
scattering of the laser-excited electrons. The transient energetic electron population
is dictated by the absorbed laser energy, which gives a higher transient increase of
effective electron temperature ΔT_e for a lower sample temperature.

From our simple calculation using the two-temperature model, we find
ΔT_e alone could not explain the PSSE dependence on temperature. We attribute this
to a combination of the interfacial exchange interaction and transport parameters in
the Pt layer. In addition to the PSSE signal, YIG/Pt emits a THz pulse that is of
a non-magnetic origin. We conclude that it originates from optical rectification due
to symmetry breaking in the lattice mismatched GGG/YIG close to the interface.

Chapter 5

Antiferromagnetic Picosecond Spin Seebeck Effect in KNiF$_3$/Pt

The spin Seebeck effect (SSE) can occur not only in ferromagnets or uncompensated ferrimagnets, but also in ferrimagnets at the compensation temperature when the net magnetic moment is zero, paramagnets, and antiferromagnets. A compensated ferrimagnet may have non-zero net transverse susceptibility from the two sublattices and hence net spin transport [177, 178]. For the paramagnetic SSE in DyScO$_3$/Pt and GGG/Pt [179] an external magnetic field is required for obtaining a SSE signal, and the signal decays rapidly with temperature. The antiferromagnetic SSE in Cr$_2$O$_3$ [180] and MnF$_2$ [181] displays a non-trivial dependence on external field. The SSE signal endures a jump at the spin-flop field in both materials. Below the spin-flop field, while the SSE signal is negligible in Cr$_2$O$_3$, it is non-zero and proportional to the field in MnF$_2$. In FeF$_2$/Pt [182] where the spin flop field ($\sim$42 Tesla) is unattainable by an external field source, strong SSE also occurs at a non-zero field.

Two kinds of theoretical approaches have been proposed to understand the field dependence of the antiferromagnetic SSE. The first considers the Hamiltonians of an antiferromagnet with a Zeeman energy term [136, 177]. At zero field, the two magnonic modes of opposite chirality typical of uniaxial antiferromagnets are degenerate. As they carry opposite angular momentum, their equal population leads to a zero net spin transfer upon the application of a temperature gradient. An external field lifts the degeneracy and shifts the energy of the magnons carrying a spin (anti)parallel to the field downward (upward); the antiferromagnet now has net spin states across the magnon spectrum. Similarly with ferromagnets at $T \neq 0$,

thermal energies excite the incoherent magnons which obey Bose-Einstein function. A temperature gradient across the bulk of the antiferromagnet now induces a spatial dependence of magnon (and phonon) population [Chapter 2.8] promoting magnon diffusion. Note that this formalism is constructed for bulk SSE.

Another approach treats the SSE in terms of time-dependent spin dynamics at the antiferromagnetic insulator (AFI)/NM interface using Ginzburg-Landau equations [133]. Both spin dynamics in the NM and the AFI are described by the respective spin susceptibilities and their interaction is mediated by the interfacial exchange coupling. Similarly to the formalism developed for ferromagnets, the thermal gradient is expressed in terms of thermal fluctuations which induce time-dependent magnetisation or spin direction [Chapter 2.8]. The final expression of the SSE spin current has a linear proportionality with the magnetic field and both spin susceptibilities [183].

$$j_s \propto \frac{g\mu_B}{\hbar^2} J_{sd}^2 \chi_{Pt} \tau_{Pt} \chi_{AFI} H_{ext} (T_e - T_m) \qquad (5.1)$$

j_s is the spin current, g is the gyromagnetic ratio, μ_B is the Bohr magneton, $\hbar$ is the Planck's constant, J_{sd} is the sd-type interfacial exchange coupling, χ_{Pt} is the spin susceptibility in Pt, τ_{Pt} is the spin scattering time in Pt, χ_{AFI} is the spin susceptibility in AFI, T_e is the effective electron temperature, and T_m is the magnon temperature. Note that Equation 5.1 resembles Equation 4.7 for ferrimagnet YIG apart from the $\chi_{AFI} H_{ext}$ factor. The antiferromagnetic SSE is predicted to peak at the Néel temperature T_N due to χ_{AFI} [184]. This formalism is used to describe antiferromagnetic SSE both below and above T_N in the long-range magnetically ordered phase and paramagnetic phase as the concept of spin susceptibility can be extended to both regimes.

In this chapter, experimental work on the PSSE in antiferromagnetic KNiF$_3$/Pt heterostructure is presented. Using the same technique as in the previous chapter, the study aims to elucidate the difference between PSSE in ferrimagnets with PSSE in antiferromagnets. Moreover, the study seeks to understand whether the formalisms above applies at very fast timescales comparable to the spin dynamics. To the author's knowledge, this study is the first experimental demonstration of PSSE with antiferromagnets as the spin current source.
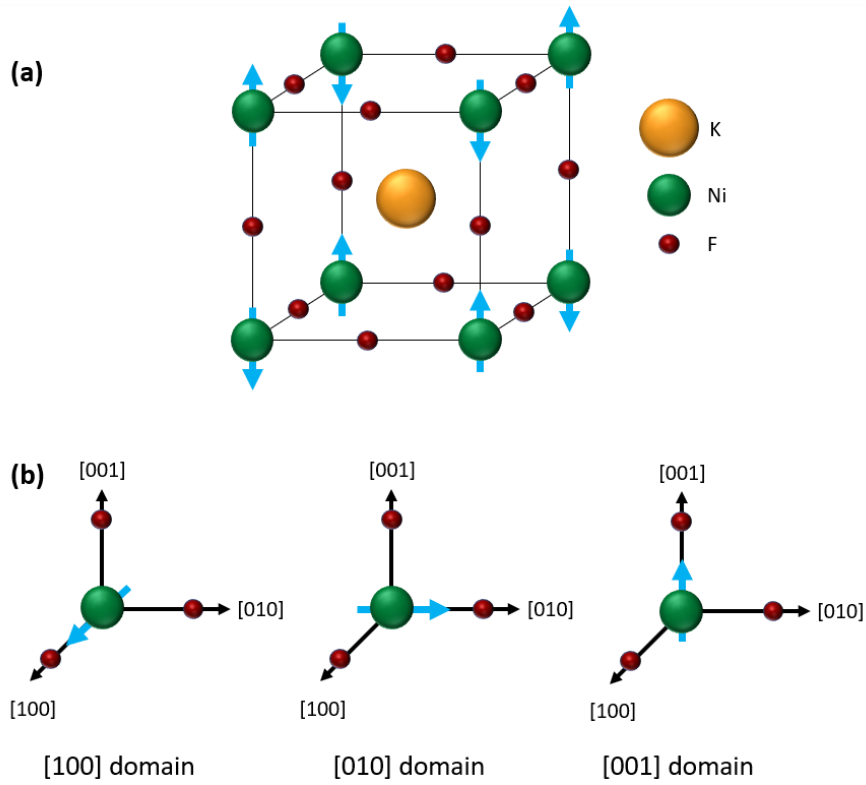
Figure 5.1: Illustration of (a) the crystal and magnetic structure and (b) the three types of domains in $KNiF_3$ structure
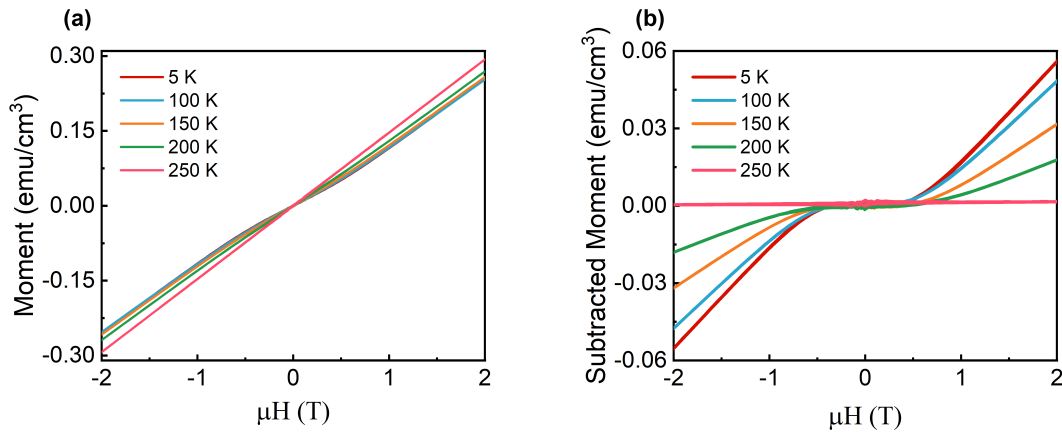

Figure 5.2: (left)Raw M-H measurements of $KNiF_3$ (right) M-H with a linear background subtraction

5.1 Sample characterisation and fabrication

The sample is a $KNiF_3$ bulk crystal (0.8 mm thick) , a model Heisenberg antiferromagnet or simple antiferromagnet where the neighbouring spins have opposite spin
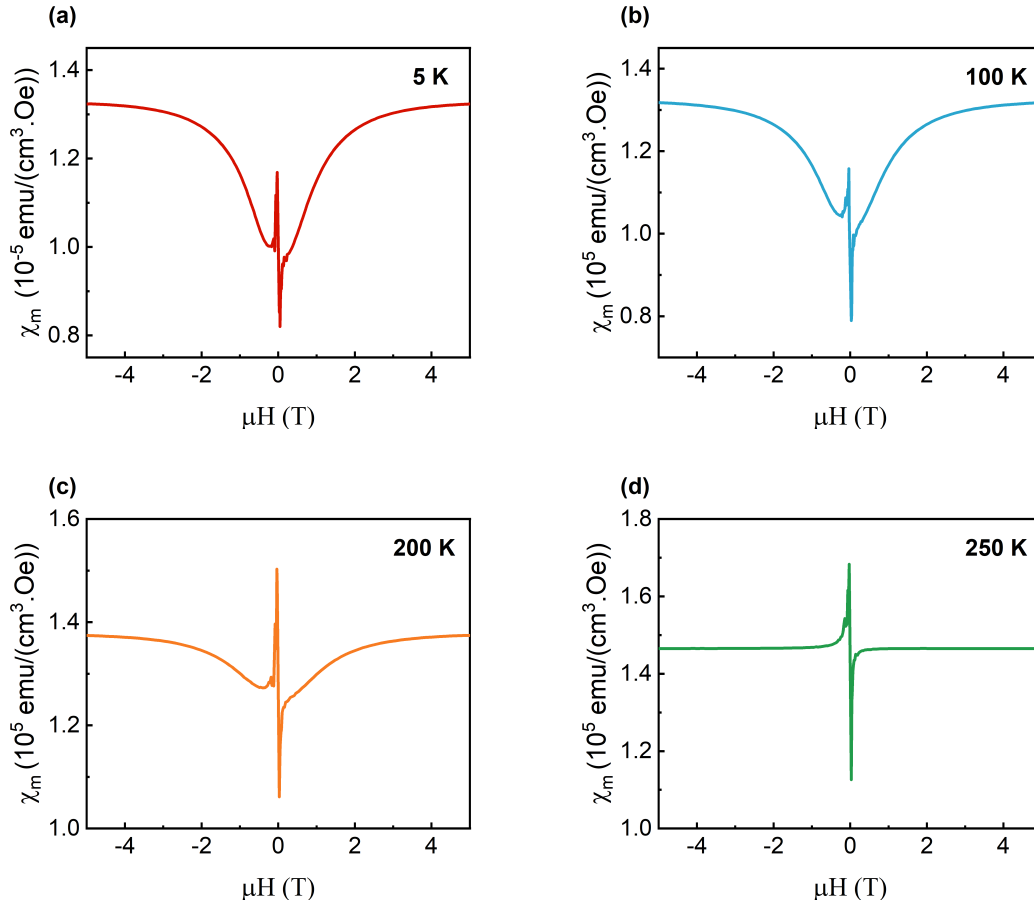
Figure 5.3: KNiF$_3$ susceptibility dependence on field at (a) 5 K (b) 100 K (c) 200
K (d) 250 K

directions in a cubic lattice [Figure 5.1] [184]. There coexist three types of domains
owing to its low anisotropy; each of them corresponds to the antiferromagnetic vec-
tor being collinear with each of the three main cubic axes ([100],[010],[001]) [Figure
5.1(b)] [185,186]. A magnetometry measurement then detects contributions from all
three types of domains. The field dependence of the magnetisation was measured at
various temperatures via SQUID [Figure 5.2(a)]. By a linear background subtraction
we extracted a critical field of 0.5 T after which the magnetisation starts to linearly
increase with the field. Likewise, the susceptibility $\chi_m = dm/dH$ on the external
field data was taken, and a value of the critical field $\sim$0.3 Tesla was obtained as
shown in Figure 5.3. Note that due to the low anisotropy in KNiF$_3$, the critical field
does not correspond to the spin-flop field but rather to the field at which domain

Figure 5.4: (left)(green) KNiF$_3$ magnetic susceptibility and (blue) its first derivative on temperature. (right) Illustration of THz emission experiment in KNiF$_3$/Pt

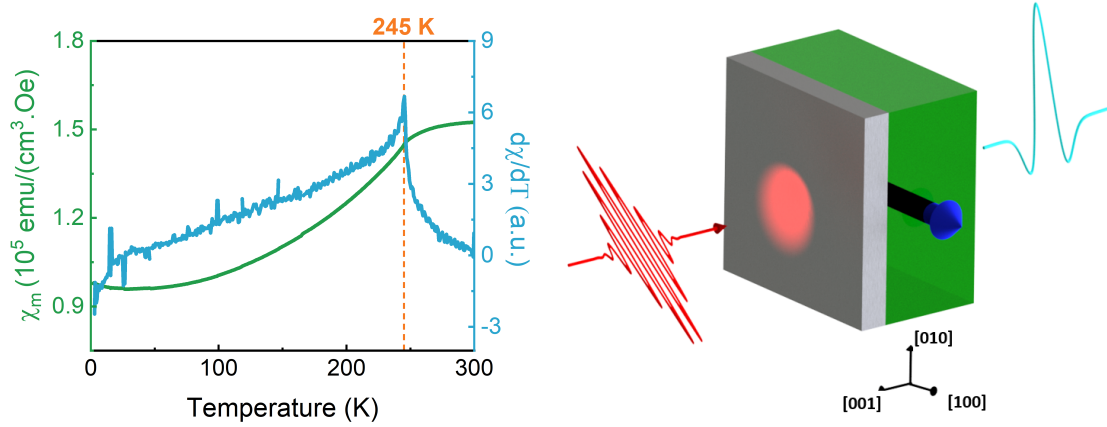walls start to move expanding domains with the Néel vector perpendicular to the field [186]. A ferromagnetic component with very low coercivity is present at all temperatures and can be due to the presence of clustered Ni islands in the crystal.

A single-domain state cannot be obtained by an external field. Applying a field along the main [100] cubic axis reduces the sizes of the [100] domains via the domain wall motion, while the [010] and [001] domains coexist and are in principle energetically equivalent and both give non-zero susceptibility values at low temperatures [Figure 5.4(a)]. However, the presence of strain or defects might include additional anisotropy terms and result in a preferential domain orientation. Increasing the temperature reduces the magnetic anisotropy making the KNiF$_3$ spins more susceptible with the field. At 245 K, the magnetic susceptibility shows a cusp. This temperature is defined as the antiferromagnetic transition temperature, or Néel temperature T_N. Above T_N, the long-range magnetic order ceases to exist and the KNiF$_3$ becomes a paramagnet. The χ_m at low temperatures is approximately 2/3 of χ_m at T> 245 K, which may indicate that the [100] domains constitute roughly 1/3 of the KNiF$_3$ volume and are fully suppressed at low temperatures as expected [187].

For the PSSE study, a 7-nm thick Pt layer was deposited on top of the KNiF$_3$. The KNiF$_3$ was polished to a surface roughness of <10 nm for good interface quality. The measurement technique that we use to characterise the picosecond SSE is terahertz emission spectroscopy described in the previous chapter. 800 nm coincides with KNiF$_3$ $^3T_{1g}^a$ mode, which results in a strong absorbance of 70 cm^{-1}
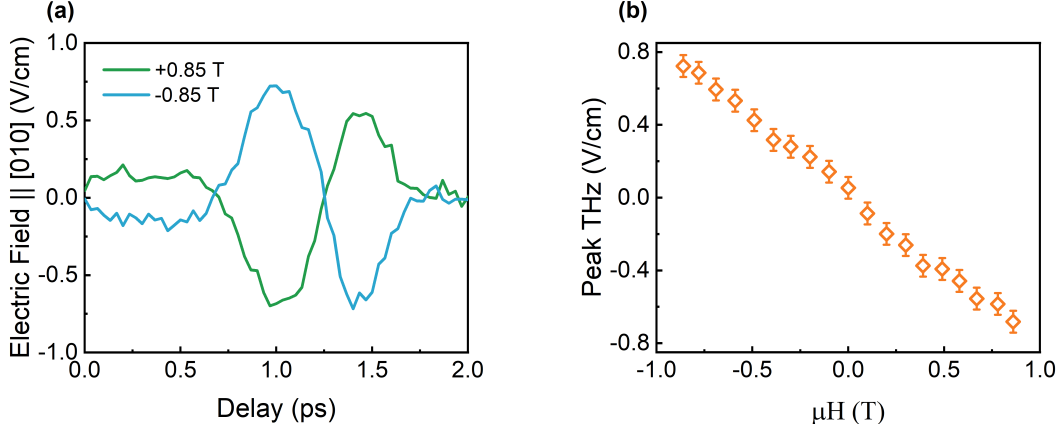
Figure 5.5: (a)Time-domain trace of THz emission from KNiF$_3$/Pt (b) Linear field
dependence of the peak THz electric field

[188]. Hence, all the PSSE measurements were done by pumping from the Pt side
[Figure 5.4(right)] to maximise the energy deposited in Pt. The absorption in the
Pt is $\sim$ 40% ($A \approx n_o/(n_{\mathrm{KNiF_3}} + n_o) \approx 0.4$ [163] where $n_{\mathrm{KNiF_3}}$(800 nm)$\approx$ 1.5 and
$n_o = 1$ [189]). The KNiF$_3$ is transparent in the low terahertz range with the lowest
phonon absorption dip at $\sim$5 THz [190]. Hence, the emitted THz from Pt is not
affected by traveling through the bulk KNiF$_3$, apart from the Fresnel reflection at
the KNiF$_3$/air interface, which is $<$ 20% in the low THz range [190]. A generous
amount of silver paste was applied to glue the sample and minimise temperature
drift during measurements. Prior to the measurements, the KNiF$_3$ was cooled down
to 10 K with applied external field of 0.85 Tesla to induce larger magnetic domains.
As the pump beam diameter is about 2 mm, the obtained THz signal is the average
signal from multiple magnetic domains, each of which is about hundreds of μm in
size [186].

5.2 Field dependence and ISHE symmetry analysis

THz emission was detected from KNiF$_3$/Pt as shown in Figure 5.5(a). To verify
that the THz emission originates from the PSSE, field dependence measurement
and ISHE symmetry analysis were performed. Figure 5.5(a) shows the time-domain
trace of the emitted pulse at 10 K using an absorbed fluence of 0.1 mJ/cm^2 in a +0.85
Tesla (green) and -0.85 Tesla (blue) magnetic field. The reversed polarity of the THz
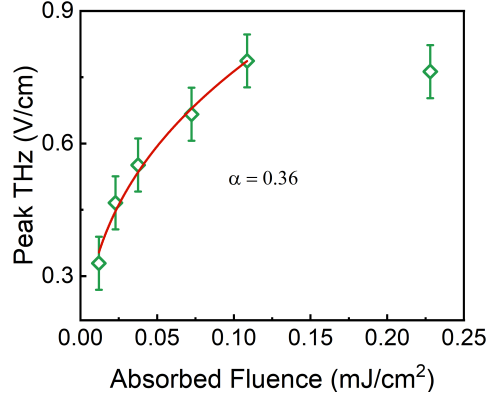
76

Figure 5.6: Fluence dependence of peak THz signal measured at 25 K

electric field at opposite values of the field demonstrates the magnetic origin of the signal. Here, the detected THz is polarised along the [010] direction, orthogonal to the external field [100] and the normal vector [001]. The negative polarity for a positive magnetic field agrees with the result of the previous chapter for Pt-side pumping. These observations are in an agreement with the ISHE symmetry. The signal displays a linear dependence on a low external field as predicted by Equation 5.1 [Figure 5.5(b)] and persists even at very low values of field below the critical field of the domain wall motion. In the proximity of the critical field, no clear jump in the amplitude of the THz emission was observed, in a contrast with bulk SSE measured in Cr_2O_3/Pt [180] and MnF_2/Pt [181]. This is likely correlated to the susceptibility, which shows a slow increase, as obtained from the magnetometry measurements [Figure 5.2], instead of an abrupt increase as in the other two antiferromagnets.

However, we need to keep in mind that the magnetometry data [Figure 5.2 and 5.3] is sensitive to the domain configuration of the entire bulk and and does not give information on the domain structure near the surface, most relevant for the PSSE. According to the two models of the SSE described above, a SSE signal is expected from all three types of domains with the Néel vector pointing along one of the main cubic directions. While the interpretation of breaking the degeneracy between opposite chirality modes is originally developed for domains with the Néel vector parallel to the field, the resonant frequency splitting also applies for the other two types of domains [2.6.3]. Moreover, the magnetic field induces a canting between opposite spins and a small magnetic moment emerges [182].
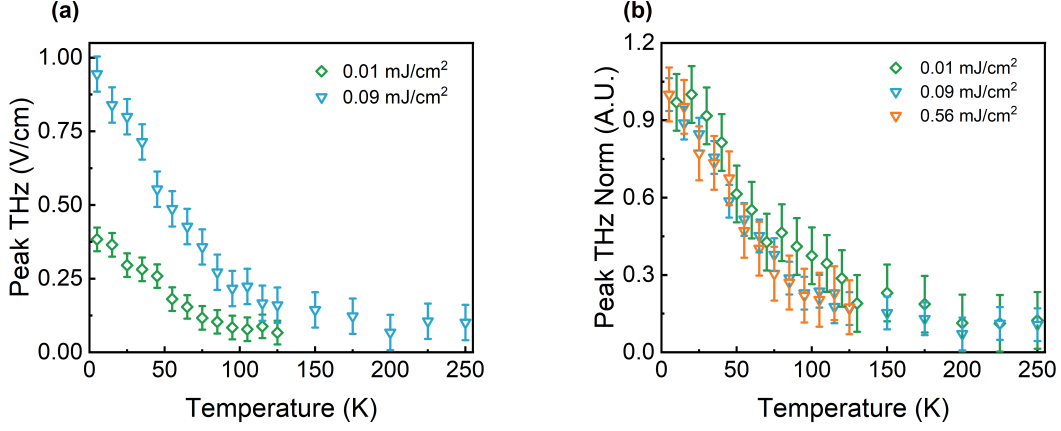
Figure 5.7: (a) raw peak signal (b) normalised signal of temperature dependence of
PSSE for different pump fluences

5.3   Fluence dependence of the PSSE

Figure 5.6 shows the fluence dependence of the peak of PSSE signal in KNiF$_3$/Pt
measured at 25 K. The signal is also nonlinear with the fluence as in YIG/Pt. This
is expected as the nonlinearity originates from the effective electron temperature de-
pendence on the pump fluence, intrinsic of the Pt layer [Chapter 4.4]. The magnetic
ordering should not affect the saturation. The PSSE in KNiF$_3$/Pt has a different
exponential factor of 0.36 compared to 0.46 in YIG/Pt. The discrepancy may origi-
nate from the absorbing KNiF$_3$, which makes the assumption of negligible ΔT_m less
appropriate.

5.4   Temperature dependence of the PSSE

In Chapter 4 we pointed out that the temperature dependence of the PSSE in
YIG/Pt is dominated by ΔT_e in Pt and J_{sd}. Differently from YIG, where the
magnetisation is roughly constant below 300 K, in KNiF$_3$ the magnetic susceptibility
increases with temperature up to the magnetic transition at 245 K [Figure 5.4(a)].

The temperature dependence of the PSSE signal in KNiF$_3$, shown in Fig-
ure 5.7 is however not correlated to the susceptibility and instead endures a rapid
increase as the temperature decreases, which resembles the YIG/Pt data in Chapter
4. Using a higher pump fluence to enhance the signal results in a similar tempera-
ture dependence trend. This is because the gradual reduction of χ_{KNiF_3}, which about

50% from 245 K to 100 K and below [Figure 5.4(a)], is overshadowed by the stronger temperature dependence of the other parameters, i.e. J_{sd} and ΔT_e. We note that the temperature dependence of J_{sd} in KNiF$_3$/Pt may differ than in YIG/Pt.

5.5 Discussion

Despite being an antiferromagnet, the PSSE signal in KNiF$_3$/Pt is notably strong. At 10 K for an absorbed fluence of $\sim$0.1 mJ/cm^2, $E_{THz} \sim$0.8 V/cm. In a comparison, at a similar absorbed fluence $E_{THz} \sim$2 V/cm in YIG/Pt. This is surprising considering that the field-induced magnetisation of KNiF$_3$ is $\chi_m H$=0.1 kA/m at 0.85 Tesla field, three orders of magnitude weaker than the spontaneous magnetisation in YIG $M_s = 172$ kA/m. Moreover, in the most recent theoretical models proposed to explain the dynamic SSE in ferrimagnetic YIG the transverse spin susceptibility $\chi_\perp$, rather than spontaneous magnetisation, has been identified as the main parameter that determines the magnitude of the PSSE [72]. Averaging over time leads to $< \chi_\perp > = | < S_{YIG} > | = 14\mu_B$, where S_{YIG} is the spin moment. Hence, the expected spin current ratio if the other parameters are comparable is $j_{s,YIG/Pt}/j_{s,\text{KNiF}_3/Pt}$ is $\sim | < S_{YIG} > |/a^3 \chi_{\text{KNiF}_3} H \approx 500$, where $a_{YIG} = 12.4$ Å [see Equation 4.7 and 5.1]. Such a huge discrepancy suggests that J_{sd} exchange coupling is orders of magnitude higher at the KNiF$_3$/Pt interface with respect to YIG/Pt [Equation 5.1]. This is in line with other experimental observations of excellent spin transport in various types of antiferromagnetic heterostructures. Strong bulk SSE was also observed in antiferromagnetic MnF$_2$/Pt. Used as a spacer layer between a ferromagnetic and a NM layer, an antiferromagnetic insulating layer of a few nm can substantially enhance spin current flowing across the interface [191–193]. Very high values of the ISHE have also been reported in metallic antiferromagnets. [194, 195]. One could argue that spurious effects may instead exist at the YIG/Pt interface which causes the reduced interfacial spin transport efficiency. However, know spurious effects such as spin-memory loss is only applicable in ferromagnetic metals [196], and magnetic proximity effects in YIG/Pt are found insignificant in modifying spin pumping [197, 198]. These findings support our argument that J_{sd}, or spin mixing conductance, in KNiF$_3$/Pt is much higher than in YIG/Pt.

The common feature among the previous observations in antiferromagnets is that spin transport is mostly efficient at temperatures close to T_N. In our case of PSSE in KNiF$_3$/Pt, no signal enhancement is observed at $T_N = 245$ K and the

strongest signal is instead observed at 10 K, in disagreement with previous measurements of the DC antiferromagnetic SSE [180–182]. The SSE is expected to drop more rapidly at low temperatures than in ferromagnets due to the typically higher antiferromagnetic magnon energies. Magnon excitation is forbidden at frequencies below the resonance mode; the population of the thermal magnons at low temperatures is hence further suppressed if the average thermal energy is lower than the magnon resonant frequency, or often called magnon gap [132, 165]. This is in disagreement with what we measure in KNiF$_3$/Pt.

The PSSE in KNiF$_3$/Pt clearly lacks several features commonly observed in antiferromagnetic SSE or any distinguishing behaviour from the PSSE in YIG/Pt apart from the linear dependence on the external field. The reason lies on the fact that KNiF$_3$ has a low antiferromagnetic resonance of 0.097 THz (0.4 meV) [188, 199] at low temperatures. Such a low resonance frequency does not hinder thermal fluctuations ($\sim$1 meV at 10 K) to excite magnons. In fact, the pulsed laser excitation easily reaches transient effective electron temperature of $\sim$100 K ($\sim$10 meV), and hence signal quenching due to the magnon gap should not be observed. The enhancement of the PSSE signal expected near T_N is challenging to measure in this case due to the poor signal-to-noise ratio and because other parameters that affect the temperature dependence of the signal more strongly.

5.6   Summary

Using the same THz emission technique, we demonstrate picosecond spin Seebeck effect in an antiferromagnetic insulator KNiF$_3$. This Heisenberg-type antiferromagnet has a resonant frequency at 0.1 THz and its transition temperature is at 245 K. We observe a linear proportionality of the PSSE signal to the applied magnetic field, which agrees with the models based on both net spin dynamics at the interface and splitting of degenerate antiferromagnetic magnon modes. The PSSE signal is strongest at the lowest temperature available and decreases to the noise level at the transition temperature 245 K. The trend resembles the one measured in YIG/Pt, and therefore we may attribute this to mostly the femtosecond excitation method, J_{sd} spin transport parameters in Pt.

The PSSE signal in KNiF$_3$ does not exhibit key signatures predicted by the models, which are a signal maximum at T_N and a stronger signal quenching at low temperatures as compared with the ferro/ferrimagnetic counterpart. We attribute

these to the relatively weak magnetic susceptibility dependence on temperature in comparison with other parameters, and the low resonant frequency. Notably, the PSSE signal magnitude in $KNiF_3$ is only several times weaker thah the one obtained in YIG/Pt despite having a three orders of magnitude weaker net magnetisation. This suggests excellent interfacial spin transparency in antiferromagnet, which has been observed in previous experiments performed using electronic techniques.

Chapter 6

Antiferromagnetic and Paramagnetic Picosecond Spin Seebeck Effect in KCoF$_3$/Pt

Following the PSSE study in KNiF$_3$/Pt, this chapter expands the work by studying KCoF$_3$/Pt. KCoF$_3$ is also a Heisenberg antiferromagnet, but with much higher antiferromagnetic resonance at $\omega_{res} = 1.17$ THz at low temperatures [45,123]. Moreover, its T_N is 117 K. The comparison between antiferromagnetic PSSE and paramagnetic PSSE measurements becomes possible using the same sample. Moreover, the high magnon gap $\hbar\omega_{res} \sim 4$ meV is comparable with the thermal energy $k_B T_e$ of the optically excited electrons heated in the Pt at low pump fluences. This allows examining the influence of the magnon dispersion on the PSSE signal at different temperatures and fluences. Having the possibility of comparing two antiferromagnets, KNiF$_3$ and KCoF$_3$, that have identical magnetic and crystal structures but very different magnon frequencies allows pinning the role of long-range magnetic order and the opening of a gap in the magnon dispersion in the measurement of the PSSE.

6.1 Sample characterisation and fabrication

The KCoF$_3$ sample is a bulk single crystal of $4 \times 4 \times 0.8$ mm^3 with transition temperature of $T_N = 117$ K, as detected from SQUID measurements in Figure 6.1(b). Similarly to KNiF$_3$, KCoF$_3$ is a simple cubic antiferromagnet and three types of antiferromagnetic domains coexist. As expected from a multi-domain antiferromag-
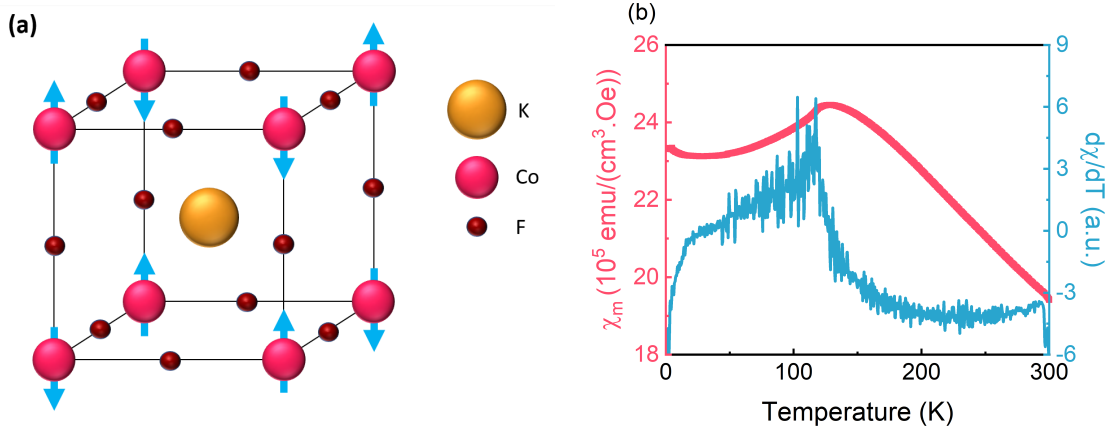
Figure 6.1: (a) Illustration of $KCoF_3$ crystal structure (b) SQUID measurement of magnetic moment (0.1 Tesla field applied) as a function of temperature, showing a peak at 117 K

net, the field-induced moment is linear in field [Figure 6.2(a)]. As shown in the SQUID measurements of the magnetisation after subtracting a linear background [Figure 6.2(b)], the first critical field in $KCoF_3$ is 2 T, higher than in $KNiF_3$ due to the higher crystalline anisotropy. We also observe a ferromagnetic-like (hysteretical) signal superimposed at low field <1 Tesla in the antiferromagnetic phase, at the transition point and in paramagnetic state at 300 K as seen in Figure 6.2(b). We attribute this to the presence of ferromagnetic clusters that form within the crystal during the growth.

Figure 6.2(c) and 6.2(d) show the magnetic susceptibility as a function of field. The sharp peaks at low fields originate from the ferromagnetic spurious moment. Disregarding the sharp peaks, our $KCoF_3$ sample changes its susceptibility by 2% from low to high field regime, which is quite different from the change of of $\sim 30\%$ measured in $KNiF_3$ [Figure 5.3(a) and 5.3(b)]. It is likely that the magnetic domains in $KCoF_3$ are already mainly comprised of the perpendicular domains (i.e. [010] and [001] domains); the [100] domains, which are the ones quenched by the magnetic field and contribute to the susceptibility change, only constitute a small portion of the entire magnetic volume. $KCoF_3$ is known for its strong magnetoelastic effect, and therefore stress induced by defects or when performing polishing could alter the magnetic domains. The small reduction of χ_m from T_N to 2 K [Figure 6.1(b)] further confirms that $\chi_\perp$ gives the larger contribution and that the sample is pre-
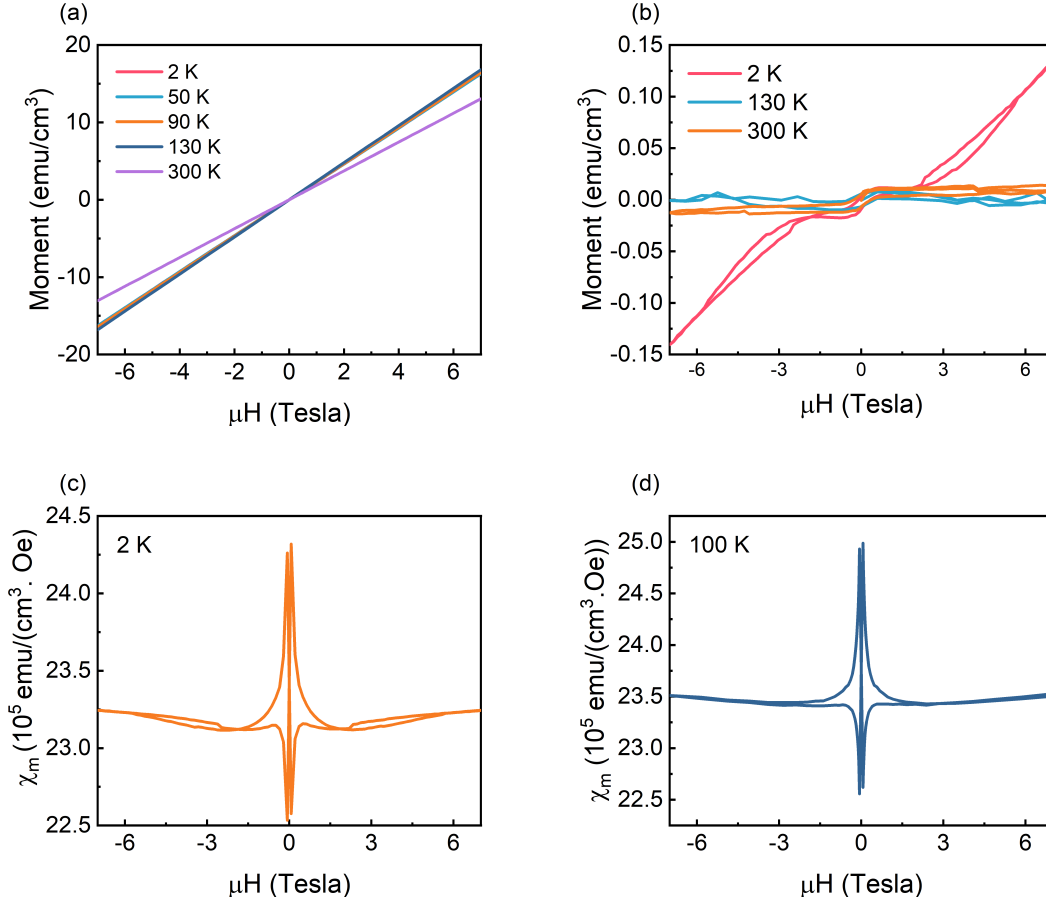
Figure 6.2: (a)Raw magnetic moment vs applied external field for $T = 2 - 300$
K (b) Hysteresis loop of ferromagnetic-like moment which appears at low fields for
all temperatures even at 300 K (c) Magnetic susceptibility χ_m as function of the
external field at 2 K and (d) at 100 K

dominantly made by the [010] and [001] domains; [100] domains would decrease its
susceptibility to about a half at low temperatures [187]. Differently from KNiF$_3$, un-
quenched orbital momentum of Co^{2+} in KCoF$_3$ strongly contributes to susceptibility
with a magnitude roughly equal with the strength of its spin susceptibility [187,200].
Field-cooling of 1 Tesla only gives a minor change in the temperature dependence
of the susceptibility [Figure 6.3], as expected from the $\chi(\mu_0 H)$ data. The downward
shift of χ with field cooling is due to the ferromagnetic clusters that exist at all
temperatures measured [Figure 6.2(b)].

For the THz emission experiments, a Pt layer of 5 nm was deposited
by sputtering on a polished surface with roughness of 1 nm. The THz emission
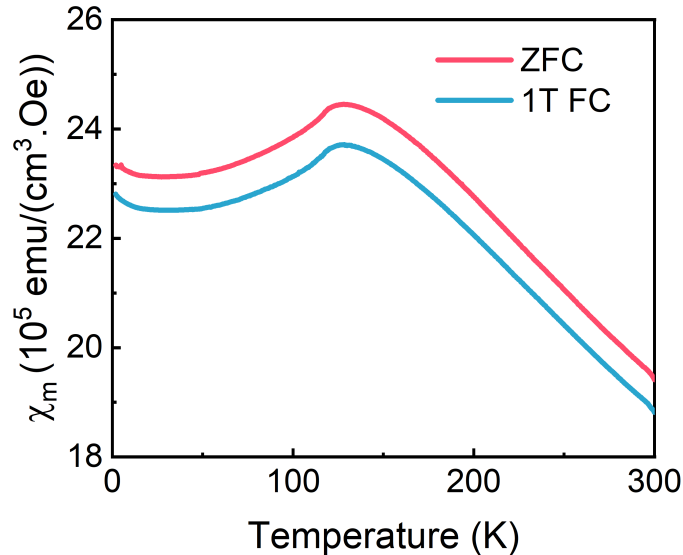
Figure 6.3: Magnetic susceptibility as a function of temperature with (red) zero-field cooling (blue) 1-Tesla field cooling

measurements were performed for both $KCoF_3$-side and Pt-side pumping. $KCoF_3$ is transparent at 800 nm and the absorption of Pt is also of the order of 60(40)% for $KCoF_3$(Pt)-side pumping, as $n_{KCoF_3,800nm} \approx 1.5$ [201]. Moreover, $KCoF_3$ first absorption dips is at $\sim$4 THz and the reflectivity is $\sim$0.2 for < 4 THz [202]. Field cooling using $\mu_0 H$=0.85 Tesla was performed prior to the measurements.

6.2 ISHE symmetry analysis and control measurements

Strong THz emission signals were detected from $KCoF_3$/Pt, as shown in Figure 6.4(c) and 6.4(d). The signals follow the ISHE symmetry; the E_{THz} polarisation is a cross product of the surface normal and the spin polarisation induced by the external field. E_{THz} is always polarised along [010] regardless of the linear pump polarisation, supporting the idea that the origin of our THz emission is connected to thermal effects. No signal is detected for [100] polarisation. The signal has the same symmetry below and above T_N, as shown in Figure 6.4(c) and Figure 6.4(d), respectively. Several control THz measurements were conducted on a $KCoF_3$ bulk crystal and a Pt layer deposited on a glass substrate [Figure 6.4(b)]. Both measurements detected zero signal, excluding any signal contribution from bulk
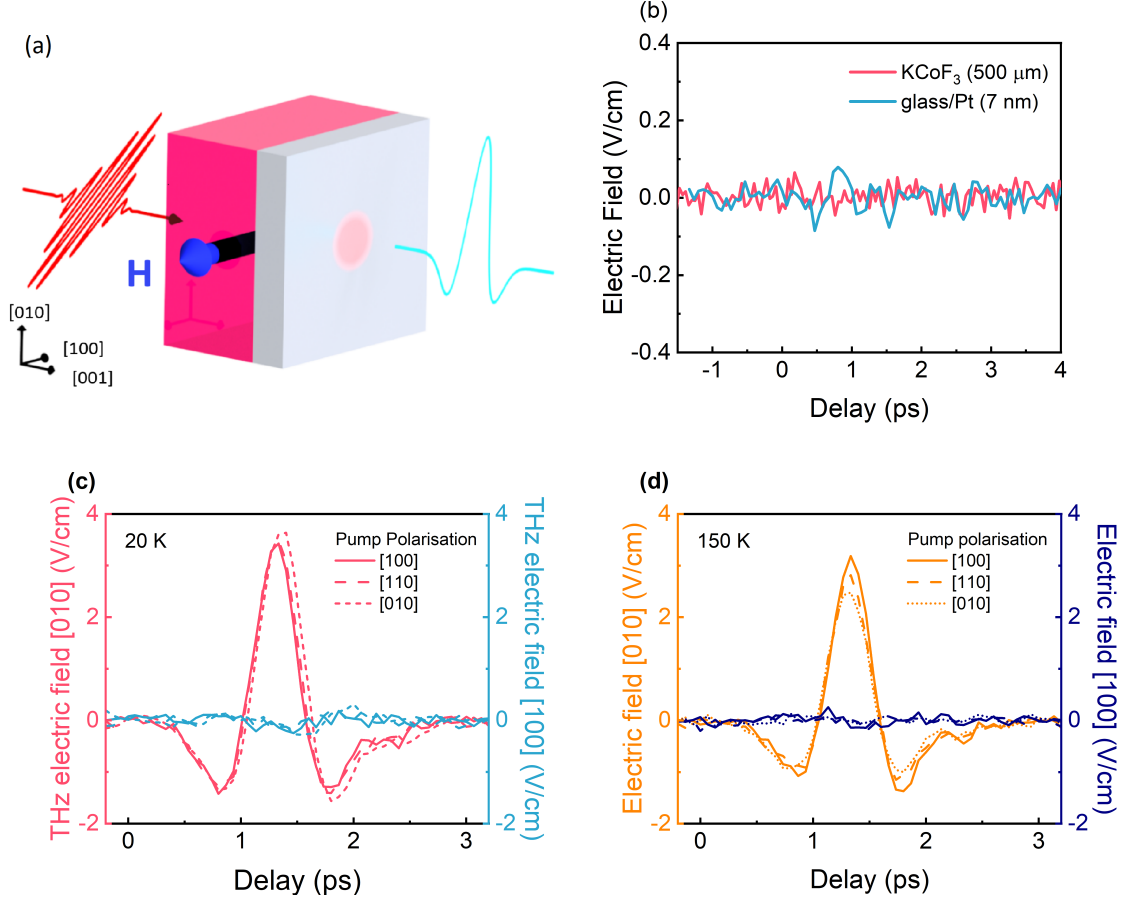
Figure 6.4: (a) Illustration of THz emission experiments in KCoF$_3$/Pt (b) Control measurements using a bulk KCoF$_3$ (pink) and glass/Pt(7nm) (light blue) which both show no signal (c) Time-domain trace of polarisation resolved THz emission (E_{THz}||[010] and E_{THz}||[100]) from KCoF$_3$/Pt at 20 K and (d) at 150 K

KCoF$_3$ and the Nernst effect from the Pt layer, respectively. We conclude that the broadband THz emission from KCoF$_3$/Pt is therefore purely from the PSSE.

6.3   Temperature dependence of the PSSE

The PSSE signals in KCoF$_3$/Pt display distinct temperature dependence compared to KNiF$_3$/Pt. As clearly seen in Figure 6.5(a), 6.5(b), the PSSE in KCoF$_3$/Pt peaks in the proximity of T_N=117 K at low fluences. Moreover, the temperature dependence changes with changing the absorbed fluence. Above T_N, the PSSE signal decays rapidly as a function of temperature with a rate that does not depend on

Figure 6.5: (a) Temperature dependence of peak E_{THz} PSSE signal for varying absorbed pump fluence (a) in V/cm and (b) in a normalised unit

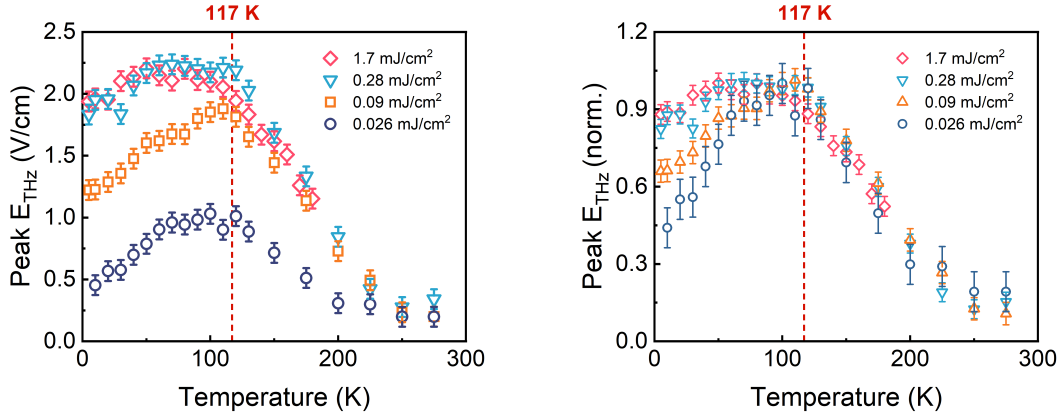the fluence. On the other hand, the rate of signal quenching below T_N is influenced by the pump fluence. At 0.026 mJ/cm^2 the PSSE signal is halved from T_N to $T = 5$ K, whereas at 0.28 mJ/cm^2 and above the PSSE signal reduces by only $\sim 10\%$. This is in direct contrast with the PSSE in KNiF$_3$/Pt which increases as temperature decreases and its rate does not change with the pump fluence. The different behaviour of the PSSE signal above and below T_N points at the role of long-range magnetic order. The discussion of the paramagnetic and the antiferromagnetic PSSE will be separated in the next sections.

6.3.1 Paramagnetic PSSE

The signal decay with temperature and the independence on the absorbed fluence above T_N in KCoF$_3$/Pt resemble the measurements in YIG/Pt and KNiF$_3$/Pt, except that the rate in KCoF$_3$/Pt is faster. Equation 5.1 also applies to paramagnets at temperatures close to T_N [183]. Hence, also in this case the parameters that determine the temperature variation of the PSSE signal are the electron temperature ΔT_e, J_{sd} interfacial exchange coupling, and the spin susceptibility of KCoF$_3$ χ_{KCoF_3}. Figure 6.6 shows that from from 120 to 300 K χ_m decreases by only $\sim 20\%$, which may not be sufficient to explain the PSSE decay rate.

The trend observed in KCoF$_3$/Pt resembles the LSSE in FeF$_2$/Pt above T_N, which also drops at a much faster rate than the field-induced magnetic moment [182], similar to our observation. In other experiments of bulk paramagnetic
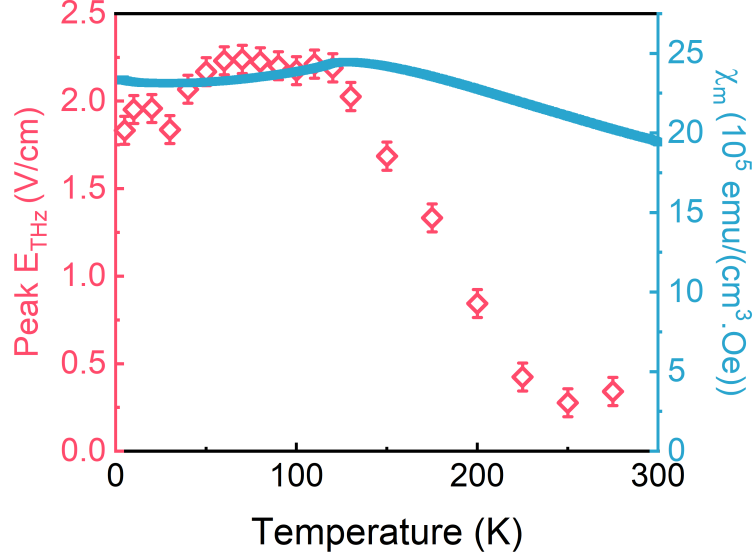
Figure 6.6: (diamond symbols) Peak E_{THz} and (blue line) magnetic susceptibilities
as a function of temperature

SSE in GGG and DySrO$_3$, the signal also decays faster than in ferromagnets at temperatures close to T_C [179]. In these experiments, the rapid decay of the signal is attributed to the temperature dependence of the spin correlation length [134,135,193]. Above T_N, although long range magnetic ordering ceases to exist, the paramagnetic spin short-range correlations extend to temperatures of 2-3 $\times$ T_N and are responsible for the spin pumping into the paramagnet. At T_N, the spin fluctuations are at maximum, which manifest with a peak in the dynamic spin susceptibility. The discrepancy observed in Figure 6.6 likely originates from the fact that PSSE probes dynamic spin susceptibility, while SQUID magnetometry measures the static susceptibility [72]. Moreover, a theoretical model in KCoF$_3$ predicts that the dynamic spin correlation parameter in drops much faster than the static susceptibility above T_N [203], supporting our interpretation for the rapid decay of the PSSE above T_N.

6.3.2 The influence of magnon dispersion on antiferromagnetic PSSE

The antiferromagnetic SSE in KCoF$_3$/Pt involves a more complex phenomenology than what is described in Equation 5.1 and the energy overlap between the magnon
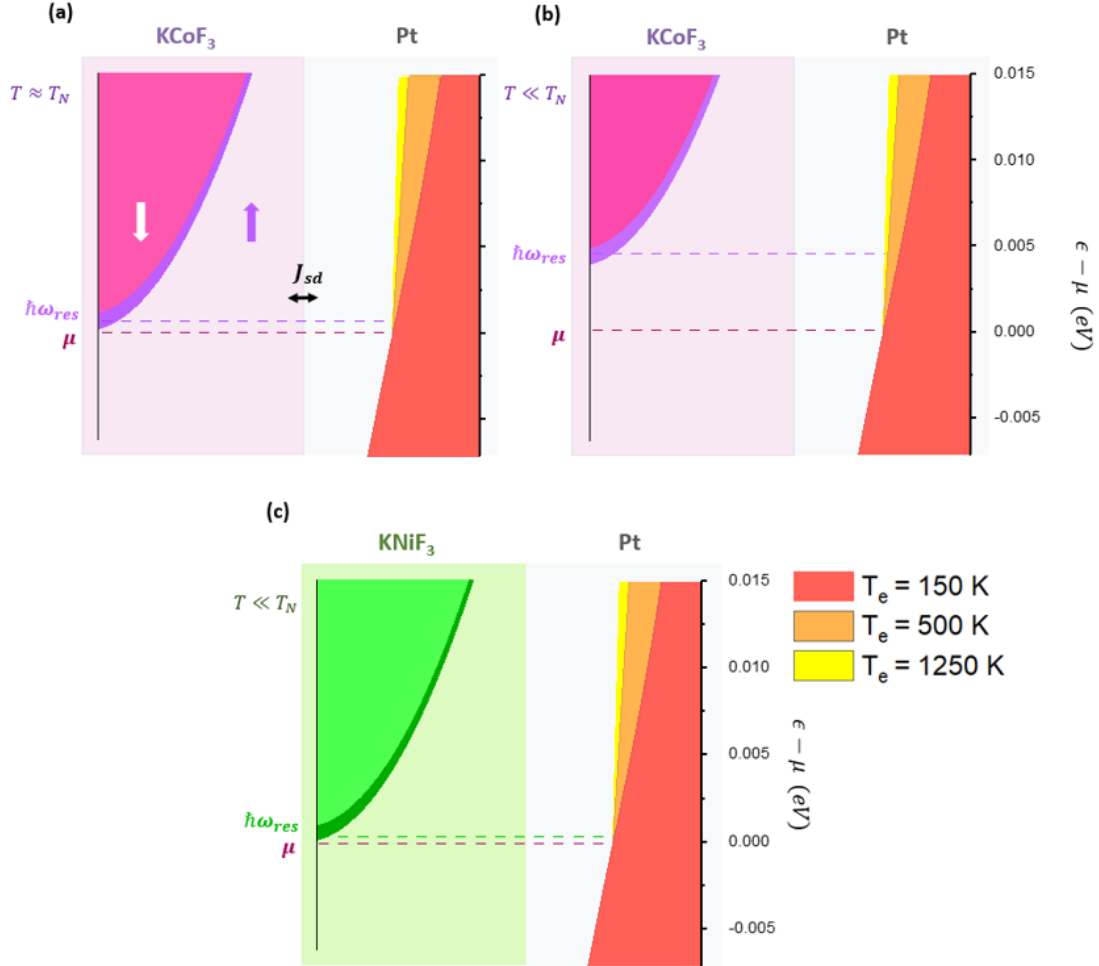
Figure 6.7: Diagram of the interplay between magnon density of states in $KCoF_3$ (purple halved-parabolic area) and electron Fermi-Dirac distribution in Pt (red, orange, and yellow area) above chemical potential defined as $\epsilon = 0$ eV (a) at sample temperature $T_0 \approx T_N$ and (b) at $T_0 \ll T_N$, (c) same but for $KNiF_3$/Pt at $T \ll T_N$. The electron temperatures $T_e = 150, 500, 1250$ K are determined using the calculation obtained in Chapter using pump fluence of 0.02, 0.2, and 1.0 mJ/cm^2 respectively.

density of states (DOS) of KCoF$_3$ and the electron energy distribution in Pt needs to
be considered. Figure 6.7(a-c) show magnon DOS in KCoF$_3$ and the electron energy
distribution in Pt, described by a Fermi Dirac function. At $T = T_N$, the thermal
fluctuations weaken the effective exchange interaction and the anisotropy such that
the resonant frequency is zero [Figure 6.7(a)]. As the temperature decreases below
T_N a magnon gap corresponding to the AFMR frequency mode opens in the magnon
density of states, and reaches 1.17 THz ($\hbar\omega \approx 4$ meV) at low temperatures. In easy
axis antiferomagnets, applying an external field along the easy axis $H||L$ splits
the resonance precessional modes into two modes with opposing chirality that carry
opposing spins [Section 2.6.3]. Consequently, the spin-up(down) magnon DOS shifts
down (up), inducing a net spin accumulation as represented by the dark purple area
at the bottom of the magnon DOS curve in Figure 6.7(a). While the Zeeman splitting
only applies to [100] domains, the external field still induces a net magnetic moment
in [010] and [001] domains and splits the magnon DOS into two branches with similar
dispersion to the [100] domains [Section 2.6.3]. These high energy spin states, can
only be excited by carriers with energy above $\hbar\omega = 4$ meV, which is higher than
thermal excitations ($k_B T_0 = 1$ meV for $T_0 = 10$ K). Even with femtosecond laser
excitation using a low pump fluence of 0.026 mJ/cm^2 or equivalently $T_e \sim 150$ K,
a substantial fraction of electrons has energy below the gap [red shared area in
Figure 6.7(a)]. In this case, the PSSE is quenched as the opening of the magnon
gap gradually excludes low energy electrons in the excitation.

At a moderate fluence of 0.2-0.3 mJ/cm^2, corresponding to $T_e \approx 500$ K [or-
ange area], the number of electrons above the gap increases and hence the quenching
of the PSSE is less pronounced. Further increase of the fluence >1 mJ/cm^2 [yellow
area], however, does not substantially increase the fraction of the electron population
above the magnon gap. In Figure 6.7 (b) we present the Fermi Dirac distribution
at $T_e = 500$ K, and $T_e = 1250$ K showing that the electron occupation probability
at energies below 4 meV is almost identical. Consequently, the temperature de-
pendence of the PSSE is expected to be similar for moderate and high fluences, as
indeed observed in Figure 6.5.

Differently from KCoF$_3$/Pt, in KNiF$_3$/Pt the magnon gap is very low
($\hbar\omega = 0.4$ meV) [188, 199]. The energy barrier introduced by the magnon gap can
be easily overcome even at very low fluences, and only excludes a tiny fraction of
low energy electrons as illustrated in Figure 6.7(c). The vast majority of the laser-
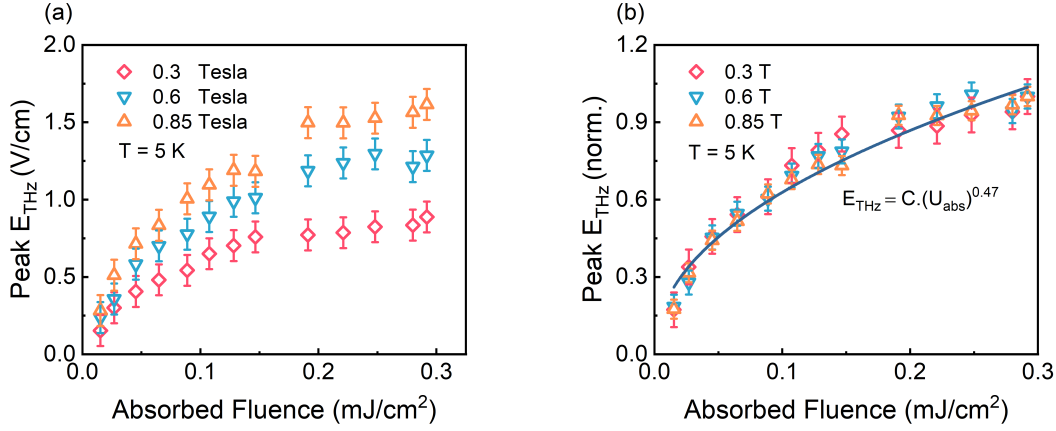
Figure 6.8: Fluence dependence peak E_{THz} for varying external fields at 5 K in V/cm and (b) normalised with fitting using $E_{THz} = \text{const. U}_{abs}^{0.47}$

excited electrons can already interact with magnons and induce interfacial net spin transfer; further increasing the absorbed fluence does not modify the energy overlap. This explains why the PSSE signal in $KNiF_3$/Pt is not quenched by lowering the sample temperature or modified by changing the pump fluence, as already discussed in Chapter 5.

Here, we address the interpretation of antiferromagnetic SSE provided in the FeF_2/Pt study, where the Zeeman splitting of magnon dispersion is treated similarly to a two-level system [182]. In this framework, only magnons in the lower branch are excited using a low energy excitation, leading to a net spin transfer. Increasing the excitation energy results in an increasing number of magnons being excited in the higher energy branch, which should result in a superposition of spin-up and spin-down population and thus a saturation of the SSE signal. In this scenario, the PSSE signal would saturate at lower fluences when lower magnetic fields are applied due to the smaller Zeeman gap. Our results in Figure 6.8 show instead that the normalised signal $E_{THz}/\mu_0 H$ has exactly the same dependence on fluence for three different values of external fields (0.3, 0.6, and 0.85 Tesla). The fluence dependence of the PSSE signal follows the fluence dependence of $T_e(U_{abs})$ explained in Chapter 4 with $E_{THz} \propto U_{abs}^{0.47}$. This is a much stronger effect than the one described above since $\mu_B \mu_0 H_{ext} \approx 0.05$ meV $<< k_B T_e$. Instead of considering magnons as a two-level system, the full magnon spectrum $k \neq 0$ illustrated in Figure 6.7 has to be considered to interpret our data. Varying the external field modifies
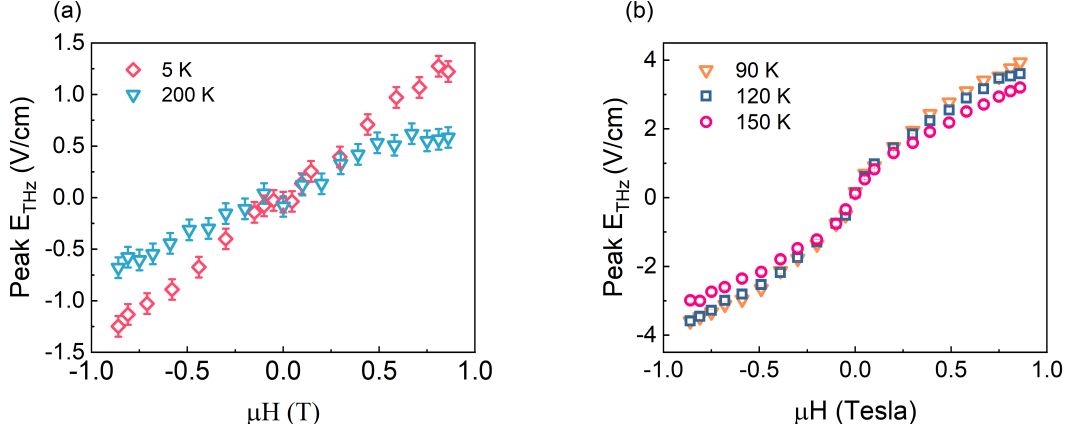
Figure 6.9: E_{THz} field dependence for temperatures (a) far from T_N and (b) close to T_N

the density of available spin states across the magnon spectrum (dark purple area in Figure 6.7 (a,b)) and increasing the absorbed fluence means more magnon states in the high energy spectrum are accessed by the electrons.

6.4 Field dependence of the PSSE

Figure 6.9 shows the field dependence of the peak in E_{THz} at different temperatures. A linear dependence is observed at temperatures well below and above T_N [Figure 6.9(a)]. In contrast, a non-trivial dependence with a kink at a low field of $\sim$0.3 Tesla is seen at temperatures between 90-150 K, as shown in Figure 6.9(b). We could not convincingly attribute this to domain wall motion as our sample is likely dominated by [010] and [001] domains [Section 6.1]. We then argue that it is due to a more complex dependence of the field-induced net magnon DOS. In studies on MnF$_2$ [136,181] and FeF$_2$ [182] at external fields below the spin-flop field, non-trivial field dependence is also observed. However, we note that these studies are in DC and more mechanisms such as bulk magnon diffusion are involved.

The small hysteresis observed in the PSSE signal at both 5 K and 150 K [Figure 6.10] is attributed to the ferromagnetic moment that is detected in our SQUID measurements [Figure 6.2(b)]. The weak ferromagnetic moment ($\sim$ 0.02 emu/cm^3) is two orders of magnitude weaker than the antiferromagnetic field-induced moment at $\mu_0 H = 0.85$ Tesla ($\mu_0 H(0.85$ Tesla) $\chi_{\text{KCoF}_3} = 2$ emu/cm^3), and indicates that it constitutes as a tiny fraction of the entire KCoF$_3$ volume. However,
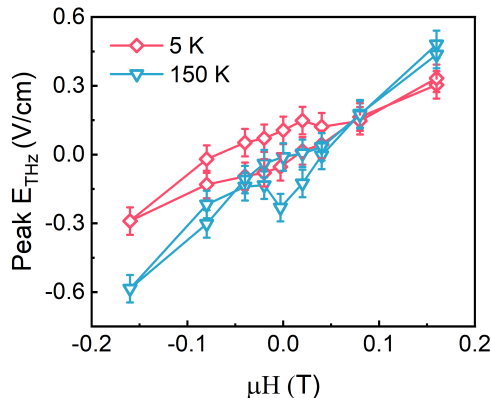
Figure 6.10: Small hysteresis PSSE signal low fields observed at antiferromagnetic state (5 K) and paramagnetic state (150 K), which then is attributed to the small ferromagnetic moment observed in Figure 6.2(b)

the ferromagnetic-like PSSE signal is about 20 times weaker than the antiferromagnetic signal at $\mu_0 = 0.85$ Tesla. The higher proportionality of the PSSE signal compared with the magnetic moment suggests that the ferromagnetic islands are more distributed towards the interface, and generate spin currents that reach the Pt layer.

6.5 PSSE signal magnitude comparison

We compare PSSE signals in $KCoF_3$, $KNiF_3$ and YIG at 120 K to exclude the influence of magnon dispersion in $KCoF_3$ as shown in Figure 6.11. The ratio of the PSSE signal between $KCoF_3$ and $KNiF_3$ is comparable to the ratio of their susceptibility. On the other hand, the PSSE signal in $KCoF_3$ is slightly stronger than in YIG despite having a field-induced magnetisation of two orders of magnitude lower than the YIG spontaneous magnetisation. This aligns with our argument discussed in Chapter 5 that the interfacial exchange coupling or spin-mixing conductance in antiferromagnets is much stronger. Further theoretical work is needed to elucidate the role of magnetic ordering to the interfacial exchange coupling.

6.6 AC spin pumping in $KCoF_3$/Pt

In a bilayer system, interfacial spin transfer can also occur via spin pumping if the staggered magnetisation is coherently excited [124]. Antiferromagnetic spin
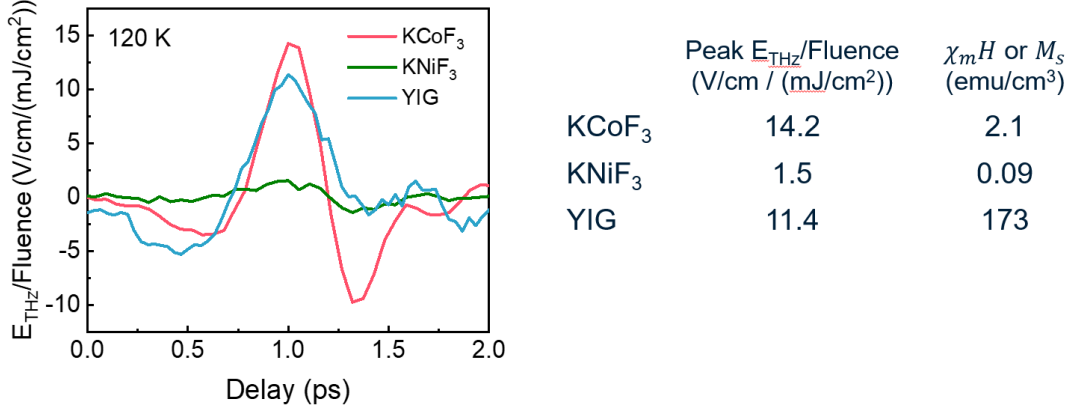
	Peak E$_{THz}$/Fluence (V/cm / (mJ/cm^2))	$\chi_m H$ or M_s (emu/cm^3)
KCoF$_3$	14.2	2.1
KNiF$_3$	1.5	0.09
YIG	11.4	173

Figure 6.11: Comparison of normalised time-domain PSSE signal with the absorbed fluence in YIG/Pt, KNiF$_3$/Pt and KCoF$_3$/Pt at 120 K for excluding the influence of KCoF$_3$ magnon gap. The table shows the values of the peak PSSE signal and the net magnetisation for each insulator

pumping has been recently demonstrated experimentally in Cr$_2$O$_3$ by a continuous wave THz source [47] and in MnF$_2$ using electron paramagnetic resonance [46] as the excitation methods. In KCoF$_3$, coherent magnon excitation using a femtosecond laser is possible via impulsive stimulated Raman scattering (ISRS) [123] [Section 2.4.1].

However, our THz experiment did not detect coherent oscillations at magnon resonance frequencies. We identify three main reasons: 1) small precessional angle induced by the ISRS excitation 2) too low sensitivity of our electro-optic sampling detection method 3) multi-domain state of KCoF$_3$. ISRS excitation in NiO is shown to give an effective magnetic field of 10 mT using 90 fs laser pulses at 80 mJ/cm^2 [204]. Assuming that the ISRS is of the same order in KCoF$_3$, the attained effective magnetic field is < 1 mT in our setup as the maximum fluence is 3 mJ/cm^2 before permanently damaging Pt via laser ablation. This is equivalent to an opening angle of the order 0.01^o. While such a magnitude is perhaps sufficient in other types of detection, the resulting spin pumping + ISHE is within the noise level of electro-optic sampling. The electric field generated by AC spin pumping can be expressed as [205]

$$E_{AC,SP}(t) = \frac{Reg^{\uparrow\downarrow}}{A} e\Theta_{SH} \frac{tanh[d_{Pt}/2\lambda_s]}{\sigma_{Pt}d_{Pt}} \omega \sin\theta \cos\theta \exp i\omega t \qquad (6.1)$$

$Reg^{\uparrow\downarrow}$ is the real part of the spin mixing conductance, A is the interface area, e is the electron charge, Θ_{SH} is the spin Hall angle of Pt, d_{Pt} is the thickness of the Pt layer, λ_s is the spin diffusion length of Pt, σ_{Pt} is the electrical conductivity, θ is the opening angle of the spin precession, ω is the precession or resonant frequency. By putting the opening angle of $\Theta_{SH} = 0.01^0$ and $\omega = 1.17$ THz, we obtain $E_{THz} \sim 0.02$ V/cm. Such a small value is further attenuated by the free space THz propagation [Section 3.3] and the multi-domain states of $KCoF_3$ [Section 6.1]. The antiferromagnetic spin pumping + ISHE signal is too weak with the current excitation and time-resolved detection.

Further work on time-resolved detection of antiferromagnetic spin pumping shall focus on stronger excitation methods and/or more sensitive detection. Mid-infrared excitation has been predicted to generate extremely strong coherent magnon $k = 0$ modes as it resonantly excites phonon modes which have stronger coupling to magnons [204]. As mentioned in Section 3.8, using heterodyne balanced detection can enhance the sensitivity by an order of magnitude. Achieving a single-domain state by applying strain of 30 GPa shall also increase the signal magnitude [187, 206].

6.7 Summary

We study picosecond spin Seebeck effect in antiferromagnetic $KCoF_3$ with transition temperature $T_N = 117$ K and resonant frequency of 1.17 THz. Despite belonging to the same antiferromagnetic class and having a similar crystal symmetry with $KNiF_3$, PSSE signal in $KCoF_3$ displays a completely different dependence on the ambient temperature and laser pump fluence. The signal is at maximum at T_N and decays above and below it. The signal quenching in antiferromagnetic phase is modified when varying the laser pump fluence, whereas in paramagnetic phase the trend is identical. Lowering the temperature below T_N gradually opens the antiferromagnetic magnon gap or increases resonant frequency, below which the low energy electrons cannot excite the magnons. Consequently, PSSE signal is quenched as fewer carriers are involved in the excitation. Increasing the laser pump fluence increases the population of high energy electrons that are above the gap and hence the signal quenching is less pronounced. These behaviours are not observed in $KNiF_3$ as the laser-excited electrons can overcome the low magnon gap at any fluence used. The measurement in paramagnetic $KCoF_3$ above T_N which is immune to the laser fluence variation supports the argument of the role of a magnon gap to the interfacial

spin excitation.

At 120 K where the influence of KCoF$_3$ magnon dispersion is not present, the PSSE signal in the two antiferromagnets shows a consistent proportionality with the magnetic susceptibility, which aligns with the model of interfacial spin dynamics. Moreover, the KCoF$_3$/Pt PSSE signal is also stronger than the YIG/Pt signal when scaled with net magnetisation. This observation further provides evidence of the excellent interfacial spin transparency in antiferromagnet. Despite detecting a strong PSSE signal, we did not detect a spin pumping signal. The coherent antiferromagnetic spin precession excited by impulsive stimulated Raman scattering is likely too weak for the current THz detector.

Chapter 7

Conclusions and Outlook

With the recent push for memory devices to perform faster, research in spintronics has expanded to explore other classes of materials such as antiferromagnets, and novel experimental techniques that exceed the well-known GHz electronics. Femtosecond laser techniques have enabled accessing the fundamental speed limits of spintronic phenomena that are orders of magnitude faster than ferromagnetic coherent precession, revealing new and rich physics on how other degrees of freedom interact with spins. THz emission spectroscopy is of a particular advantage among the other laser techniques as it acts as an ultrafast amperemeter, which allows using the magnetic insulator/heavy metal heterostructures typically used in electronic spintronic experiments. This work presented in thesis is dedicated to deepening the understanding of incoherent spin current injection by heat, namely spin Seebeck effect (SSE), by performing experiments in a faster time scale using THz emission spectroscopy.

Chapter 3 discusses the process of building the THz spectroscopy setup, which is intended for both THz emission and THz transmission spectroscopy measurements. ZnTe is used as the detector crystal for electro-optic sampling and as the THz source for THz transmission. The emission setup utilises an amplified femtosecond laser to excite the sample and detect the emitted THz radiation. Key milestones are achieved for both setups 1) SNR of >1000 for THz transmission and 2) highly sensitive THz emission detection with 120 V/cm peak THz emission from Co(5)/Pt(3) using 25 μJ energy per pulse 3) noise level of 0.1 V/cm with high signal stability for a THz emission setup.

We comprehensively investigate the spin Seebeck effect using the THz

emission spectroscopy in various magnetic orderings: ferrimagnetic, antiferromagnetic, and paramagnetic. Using a ferrimagnet YIG/Pt, a standard system for studying the SSE, this study elicits the key differences between using Joule heating and femtosecond laser absorption by the Pt layer in exciting SSE. In low frequency electronic measurements, SSE occurs when a temperature gradient in a bulk insulator causes magnon diffusion and the magnon population is determined by the available thermal energy in the system. Femtosecond laser excitation, in contrast, generates spin current by interfacial electron-magnon scattering and the population of the excited free electrons is dictated by the laser absorption in Pt.

The extremely high effective electron temperature established in the first 100 fs by the laser pulse creates a strong SSE excitation even at a cryogenic temperature, where the number of thermally excited carriers significantly diminishes. The laser excitation is in fact stronger at a lower temperature due to the low electronic heat capacity. The rapid excitation and decay of the effective electron temperature renders the temperature gradient/discontinuity localised at the interface, and therefore we can exclude the bulk contribution of magnon propagation from our analysis. The temperature dependence of the signal is therefore influenced by transport parameters in Pt, the transient increase of effective electron temperature, and the interfacial exchange interaction. We note that the higher magnon branches that carry opposite effective spin in YIG may also contribute the signal decrease at a high temperature.

In antiferromagnets where net spontaneous magnetisation is zero, an external field is required to generate the spin current. It can be understood as the field-induced moment or the breaking of degeneracy of the two antiferromagnetic magnons that carry opposite effective spins. We unambiguously demonstrate that the high antiferromagnetic resonant frequency prevents low energy electrons to be involved in the interfacial electron-magnon scattering. We clearly observe a distinct temperature and fluence dependence of PSSE signal in $KCoF_3$ as compared with in $KNiF_3$, two antiferromagnetic insulators belonging to the same magnetic class but with very different resonant frequencies. In $KCoF_3$, a signal quenching below magnetic transition temperature originates from the high resonant frequency, which can be seen as a magnon gap preventing low energy electron-magnon scatterings. Increasing the absorbed laser fluence energises the electrons to overcome the magnon gap. This effect is absent in $KNiF_3$ due to its low resonant frequency and hence

most electrons are energetic enough to excite the magnons regardless of the experimental condition. Our experiments may explain discrepancies in previous studies of antiferromagnetic spin transport across different heterostructures. In antiferromagnets with a high magnon gap such as CoO, NiO, FeF$_2$, the interfacial spin current is maximum at T_N, as the magnon gap disappears. On the other hand, in Cr$_2$O$_3$ and MnF$_2$, such signal divergence at T_N is not observed as their low magnon gaps do not substantially quench the number of thermally excited magnons even at low temperatures.

Our results of strong antiferromagnetic PSSE signals corroborate earlier observations of high interfacial spin transparency in several antiferromagnets. The model of dynamic SSE may allow us to point to the interfacial exchange coupling J_{sd}. The model is developed, however, for electronic measurements where the full frequency spectrum of spin susceptibility is not explicitly expressed. Moreover, the dispersion function of the lowest magnon mode not only dictates the minimum electron energies but also influences the magnon density of states available for the excitation. Developing mathematical expressions of these parameters may unveil the origins of the high spin transparency at AFI/NM interfaces in comparison to FI/NM interfaces. It may also be instructive to perform PSSE studies in a simple ferromagnet such as EuO, and in paramagnetic GGG, to obtain a complete picture of magnetic ordering influence on the interfacial spin Seebeck effect. Gaining these insights may accelerate the progress towards harnessing the full potentials of antiferromagnets for fast spintronic memory devices.

Appendix A

Steps to assemble THz setup

The steps of assembling and fine tuning the THz setup are briefly outlined. The configuration of the entire table was designed using AutoCAD for precise space management and optical path measurement. Next, the optical table was marked according to the design. To place and roughly align the optics, a low power HeNe continuous wave (CW) 632 nm laser was used. The low power laser was placed right after the first beam splitter close to the Solstice Ace output and ensured to be parallel to the expected path of the actual beam. Once all mirrors were in place, the direct output of Solstice Ace was used for more precise alignment. For safety reasons, a laser goggle and NIR viewing card were used all the time.

Alignment of the delay line assembly was performed by observing the beam pointing movement at about 3 meters from the delay line. The alignment was considered acceptable when the beam spot movement on a ruled beam block could not be distinguished by eye (less than 1 mm) when moving the stage in the maximum range (0-325 mm). This alignment method is satisfactory as for day to day measurements only 3-5 mm linear stage range is used. This corresponds to the beam spot travelling ~ 10 μm (assuming 325 mm travel result in ~ 1 mm beam travelling), which is much smaller than the focused pump beam size of about ~ 2 mm.

Alignment procedures for the 4 OAP mirrors were slightly different because the 1st OAP mirror is supposed to capture the diverging THz beam from the ZnTe emitter. Using the collimated 800 nm Solstice output resulted in the beam being focused after the 1st OAP mirror instead of being collimated. To solve this, a beam diffuser was placed on the spot where the ZnTe would be placed to replicate

the diverging THz beam. Although one should prevent directing 800 nm femtosecond pulses to a gold-coated mirror due to its relatively high absorption (10% at 800 nm), the femtosecond beam was always diverged when reaching the OAP mirrors, and hence had a low fluence. Moreover, the protective coating above the gold coating should prevent the mirrors from damage. By observing the reflected beam all the way after the 4th OAP mirror using the viewing card, all the OAP mirrors were fine tuned to direct the beam to the point where the ZnTe detector was in place. Aligning the THz beam path using 800 nm pump pulse provided a satisfactory quality of alignment because the THz emission from ZnTe is collinear with the 800 nm pump. Aligning the probe beam to the ZnTe detector and the balanced detector, on the other hand, was straightforward.

Once the spatial overlap was roughly achieved at the ZnTe detector location (Figure A.1), the power of the pump and probe beams were adjusted. The balanced/subtraction (monitor) channel is connected to Lock-In 1(2), respectively. To tune the balanced/subtraction channel, the frequency was set to 5 kHz and the balanced output was minimised by adjusting the QWP with the THz path blocked. For optimal use, the balanced channel reading is 0.2 mV or below at 5 kHz, and $< 0.5~\mu V$ at 2.5 kHz. In normal use, the monitor channel reads 2-3 mV. At this point, the THz path was opened.

Once a THz peak was detected, fine alignment further improved the signal by first setting the linear stage at the position of the peak of the THz pulse. The recommended starting point is adjusting the ZnTe detector and the ZnTe emitter. The orientation of the ZnTe detector influences the magnitude of the detected signals as demonstrated in Section 3.3.1. After rotating the ZnTe detector, an adjustment at the QWP is needed to compensate the ZnTe linear birefringence. Moreover, the position of the ZnTe detector should be finely adjusted to find the exact focal point of the THz beam. Next, the orientation of the ZnTe emitter should be fine tuned. Finely adjusting the OAP mirrors tilting might greatly enhance the detected THz signals. Aligning the OAP mirrors however shifts the temporal overlap and one should inspect the change in zero time delay of the THz pulse. The 4th OAP mirror controls the spatial overlap between the THz pulse and the probe beam, and hence one might want to start fine alignment from this mirror after adjusting the ZnTe crystals. Lastly, adjusting the two mirrors right before both the ZnTe emitter and detector also enhanced the signal by tuning the THz beam and probe beam

101

Figure A.1: A picture of spatial overlap between the probe beam (smaller stronger spot at the centre) and the THz beam, which is represented by 800 nm light surrounding the probe beam

propagation direction, respectively.

Appendix B

First version of THz transmission setup

This appendix presents the first THz signals obtained using the setup. Several tests were performed to further optimise the measurement parameters, as well as identify room for improvement.

B.0.1   The first THz signals

Figure B.1 shows our first time-resolved THz signals. We detected a THz peak signal of 280 μV, with a probe power of 6 mV (lock-in reading). This probe power was quite high and in the subsequent measurements, lower power was used. The single cycle THz pulse emitted from ZnTe signal was the first 3 peaks enclosed by the blue dashed rectangle. The subsequent peaks correspond to the absorption and re-emission of the THz pulse by water vapour in the environment, back reflections inside the ZnTe, and electro-optic sampling artefacts [207]. Figure B.2(a) shows the FFT of the obtained signal. The bandwidth is about 2.5 THz, which matches with the estimation in Figure 3.6. As mentioned in Section 2.1.2, the low-frequency side of the band is limited by propagation loss in the setup. The high frequency limit is mainly imposed by the TO phonon absorption of ZnTe at about 5.3 THz, and the group velocity mismatch. In frequency domain, the water absorption manifests as dips in the spectrum. The strong dips at 1.17 THz and 1.7 THz agree with reported data [139]. If FFT is only performed for the three main peaks (blue dashed rectangle), we obtain a smooth frequency domain with the same bandwidth, shown
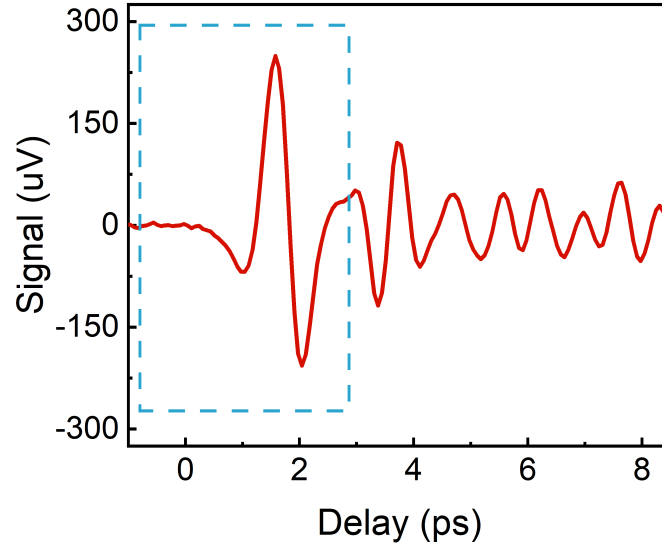
Figure B.1: The first THz time-domain data from our setup. The blue dashed rectangle indicates the actual signal from the ZnTe emitter
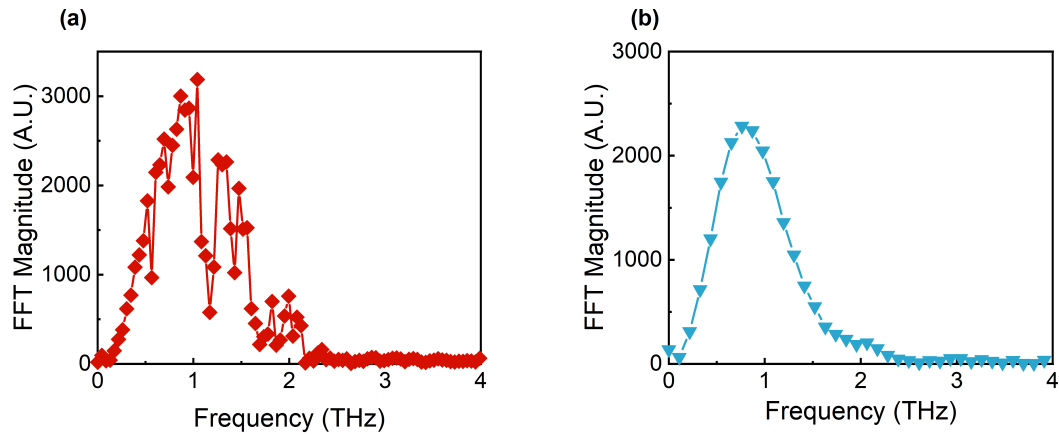

Figure B.2: Frequency-domain data after performing FFT to (a) the entire 20 ps range of data (b) the first 3 peaks of the time-domain data presented in Figure B.1
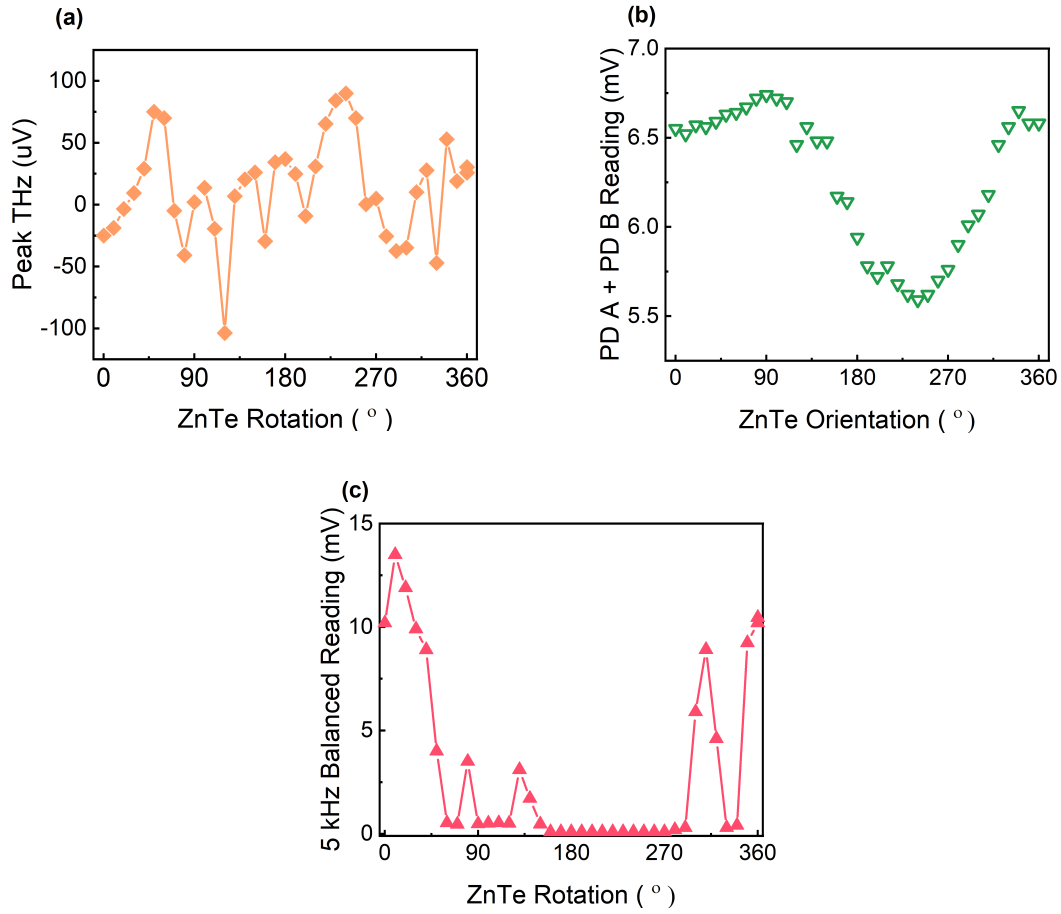
Figure B.3: The influence of ZnTe detector orientation on (a) Peak time-domain THz signal, (b) total probe intensity read by the two photodiodes, (c) minimized 5 kHz balanced channel output

in Figure B.2(b). The observations prove that the signal is THz emission from ZnTe.

The measurements presented in Figure B.3(a) show how the THz peak amplitude changes upon rotating the ZnTe detector. However, this was different from the experimental data shown in [138]; in fact our signal appeared to be scattered rather than having a definite trend. When the ZnTe detector was turned, the QWP needed readjustment for compensating the linear birefringence of the ZnTe. This constant adjustment hindered obtaining a consistent readout of phase of the lock-in signal. The beam pointing changed when rotating the ZnTe detector since the total probe intensity received by the two photodiodes differed [Figure B.3(b)]. Moreover, at certain ZnTe orientations, the balanced channel could not be minimized to below
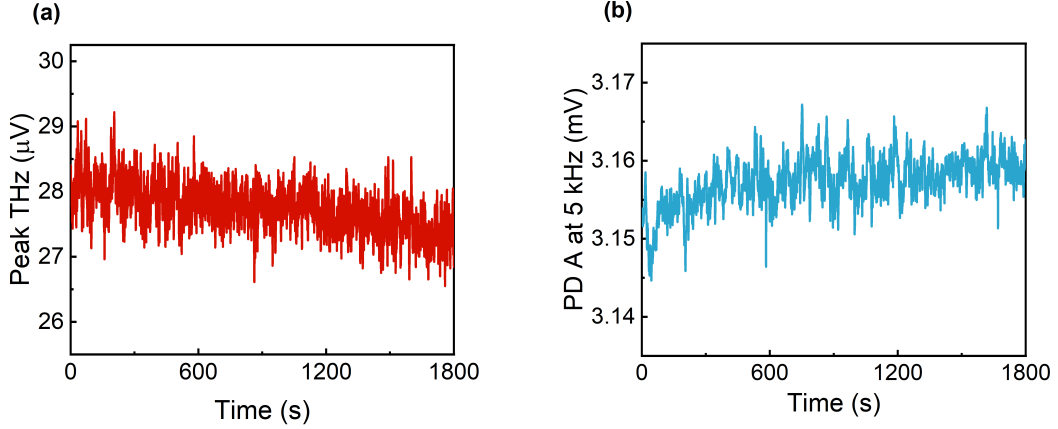
Figure B.4: (a) Peak THz pulse signal stability and (b) the corresponding monitor reading of 1st version of the setup

0.3 mV, implying that the split probe beams clipped outside the active area of the photodiodes. Further fine alignment was needed.

The THz peak and the corresponding monitor channel had good stability for 1800s [Figure B.4]. The signal fluctuated only $\pm$ 1 μV while the probe intensity fluctuated less than 1%. The time profile of the two photodetector monitor readings (referred to as PD A and PD B) were mostly identical across the acquired time [Figure B.5(a)]. Note that the difference in PD A and PD B reading of 0.2 mV should correspond to 6 mV in the balanced channel (30 times amplification of the balanced channel). Instead, the balanced channel also read 0.2 mV. The discrepancy might be due nonlinear sensitivity at high power. This mismatch could be avoided by choosing a low probe power, as explained later.

Another test showed the instance when the two channels did not have common intensity profiles [Figure B.5(b)] which could lead to inaccurate balanced channel reading. The beam pointing can deviate during the measurement due to heating of the optics and/or dusts landing on one of the optics. The non-balanced reading could bury the electro-optic signal, as shown in Figure B.5(c).

B.0.2   Probe power dependence

The dependence of the monitor lock-in output on the probe power was performed. A fine control of the probe power was achieved by using a half wave plate (HWP)
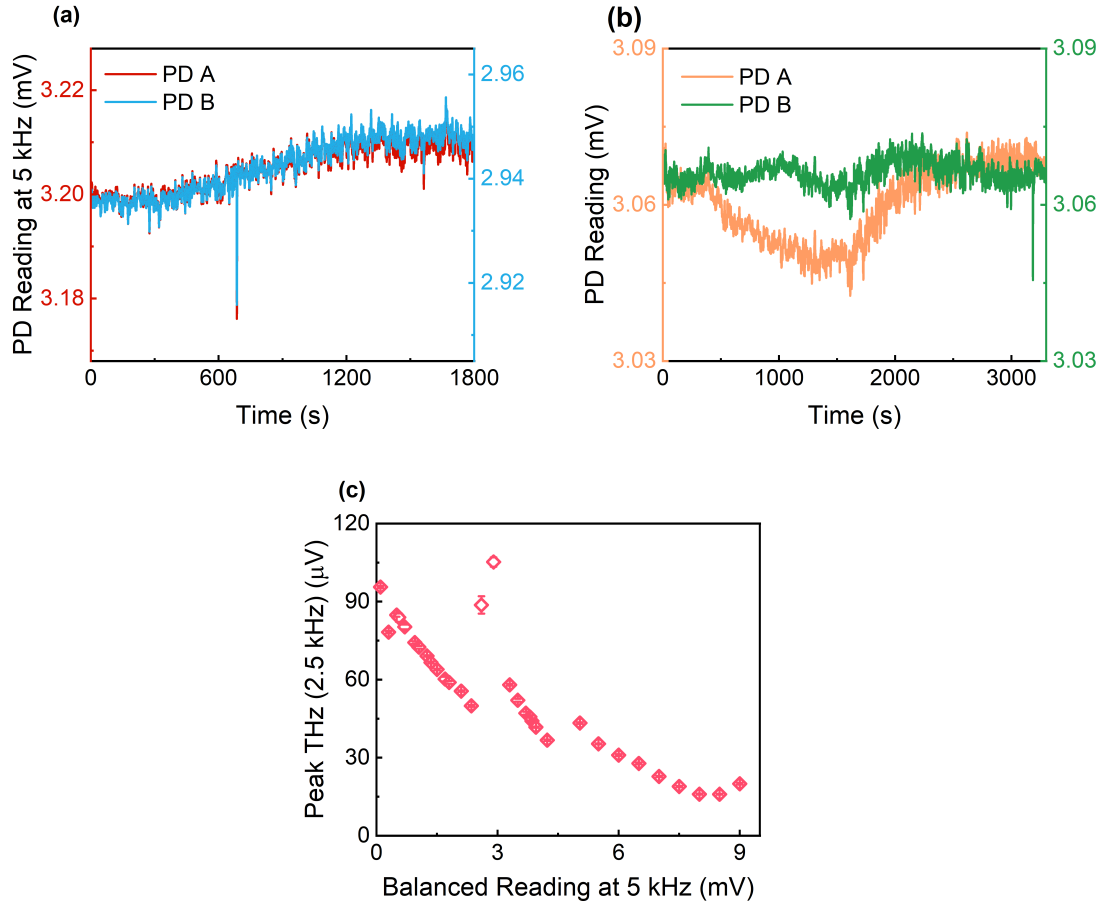
Figure B.5: Probe stability as read by the two monitor channels: (a) the desired signals (b) when the readings change over time. (c) Peak THz signal at 2.5 kHz as a function of balanced channel reading at 5 kHz

and a linear polariser. HWP rotated the probe beam polarisation and the linear polariser only allowed horizontally polarised light to transmit. According to Malus' Law, the transmitted intensity is $I = \cos^2(\theta)$, where θ is the angle between the probe beam polarisation and the linear polariser axis. Figure B.6 plots monitor output vs $\cos^2(\theta)$ of polarisation rotation, which is expected to be a linear dependence. However, the linearity occurred only up to a monitor output power of 2 mV. Above that, the monitor output voltage displayed saturation behaviour. At high probe power, the monitor channels sent a high voltage to the lock in due to its 10 V/mW amplification. Input voltages above 2 V saturated the lock-in input channel. Any part of the peak above 2 V was cropped, which lowered the demodulated lock-in
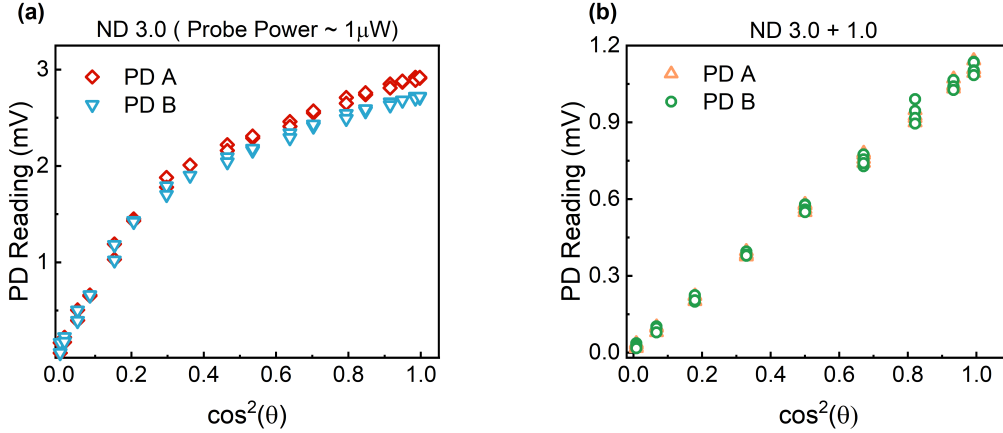
Figure B.6: Monitor reading dependence on $\cos^2(\theta)$ of angle between probe polarisation and the polariser axis. It should be linear as expected from Malus' Law. The two figures use different maximum probe power controlled by ND filters (a) ND 3.0 (b) ND 3.0 + 1.0

output and hence gave the saturation trend. The lock-in displayed 'input overload' above 2.7 mV of monitor output. Moreover, the magnitude trend differed for the two photodiodes above 2 mV, as shown in Figure B.6(a) despite having the exact same response at low probe power. The discrepancy originated from unequal response of the two photodiodes at high input power. This was further verified by putting an additional ND 1.0 filter, which rendered the outputs equal [B.6(b)].

B.0.3 Pump power dependence

Figure B.7 shows the THz peak signal dependence on pump beam power, detected using probe monitor output of 2 mV. The plot shows the converted raw signal to E_{THz} as a function of pump energy per pulse (pump spot size $\sim$3 mm diameter). Our obtained data was much lower than the published data for 1 mm ZnTe emitter and detector, and saturated at a much lower pump fluence ($\sim$0.1 mJ/cm^2) [208,209]. Note that the small pump spot was used because the beam must be smaller than the chopper spacing of $\sim$5 mm. As only one lens was in place, the converging pump beam size was $\sim$3 mm when reaching the ZnTe emitter. The pump beam size should be equal to the ZnTe diameter for optimum THz generation. On a side note, some irregularities were observed in the ZnTe emitter. The crystal emitted strong green light when being pumped by 800 nm. Moreover, after several hours of usage, the
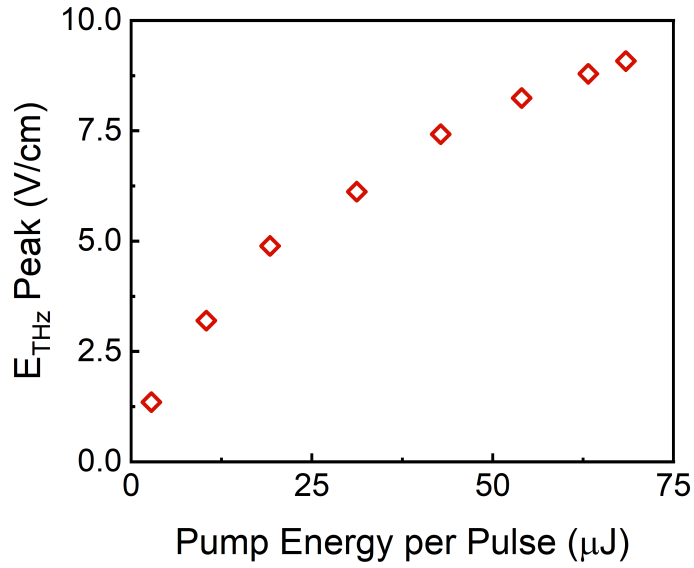
Figure B.7: THz electric field peak (V/cm) as a function of pump energy per pulse

crystal slightly changed its colour, although the crystal colour recovered after cooling down. These were indicatives of the ZnTe absorbing a substantial fraction of the pump power.

Appendix C

Three-lens system for pump beam in THz transmission

The telescope system illustrated in Figure C.1 has enabled utilising the entire ZnTe emitter area to maximise THz generation. The telescope system consists of two 2-inch f=300 mm plano-convex lenses (Thorlabs LA1256-B-M) and one 1-inch f=-50 mm plano-concave lens (Thorlabs LC1715-B-ML). The first lens focuses the beam, and the second lens expands the beam. The chopper is placed where the beam size is ~4.5 mm as the chopper wheel is for a laser beam diameter < 5 mm. The third lens collimates the pump beam with roughly 10 mm diameter. The telescope system improved the signal by a factor of 2-3 [Figure C.2]; the THz peak was still at least an order magnitude smaller than the previously reported data. This led us to change the ZnTe emitter to one from a different supplier.
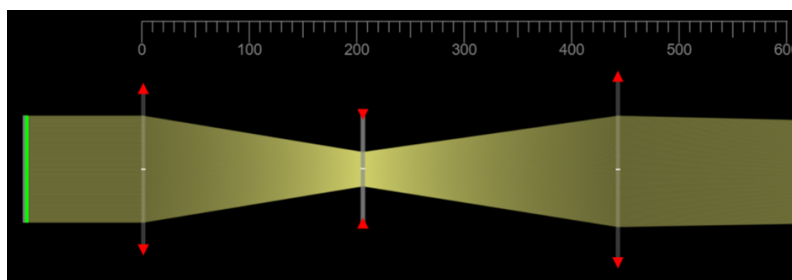
Figure C.1: An illustration of a three-lens system simulated using free online ray simulation software https://ricktu288.github.io/ray-optics/simulator/
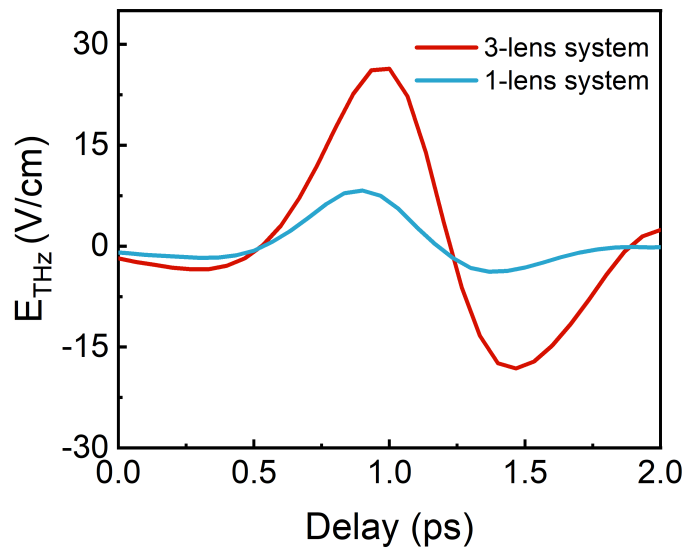
Figure C.2: THz peak obtained with three-lens system compared to one-lens system

Appendix D

Replacing the ZnTe emitter
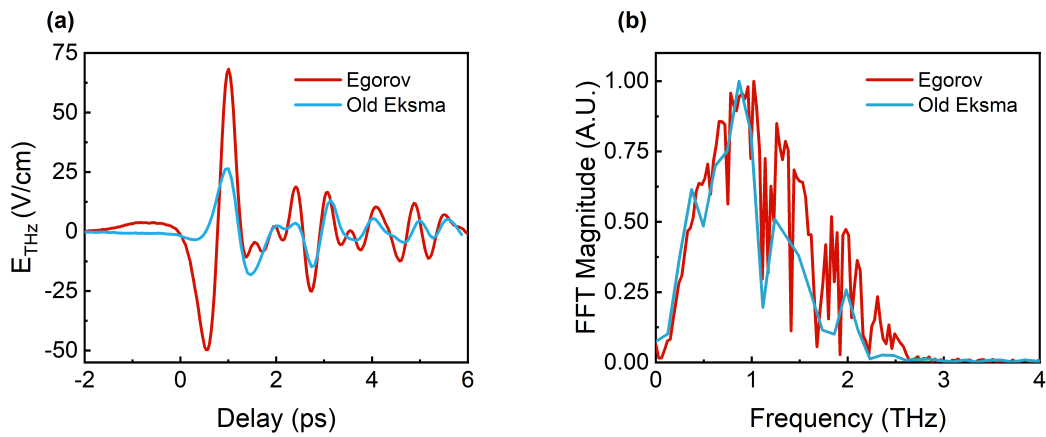
Figure D.1: (a) Time-domain (b) frequency domain data of THz emitted by the ZnTe crystal from Egorov Scientific

The new 1-mm thick ZnTe emitter with 10 mm diameter was from Egorov scientific. This crystal generated 3 times stronger signal without substantially changing the alignment [Figure D.1(a)]. The frequency domain data also showed the expected spectrum [Figure D.1(b)]. Moreover, the signal to noise ratio (SNR) was about 700 with averaging >5 iterations.

Appendix E

First version of THz emission setup

This section discusses the results obtained from the first version of the THz emission setup. As a calibration sample, we used Co/Pt thin film bilayers with varying thicknesses deposited on a glass substrate. The 800 nm femtosecond pump pulse excites spin-polarised electrons in the Co and the spins flow to the Pt layer [62]. By Inverse Spin Hall Effect, the Pt layer converts the spins to charge current. As the current flows in a sub-picosecond time scale, THz electro-dipole radiation is emitted at the Pt/air interface [70]. A FM/NM thin bilayer is an ideal calibration sample for its simple structure and the extensive literature available.

The results presented here were obtained from a Co(10)/Pt(3) sample. The pump beam width should be smaller than 3 mm when passing through the 2nd OAP mirror to avoid clipping. On the other hand, the pump diameter should be large enough at the sample to minimise the divergence of the emitted THz and to avoid damaging the Co/Pt with a too high fluence. To fulfill those requirements we initially used a convex lens with longest possible focal length available f=1000 mm (Thorlabs LA1464-B).

We measured a peak signal of 15 V/cm at a pump energy per pulse of 25 μJ comparable to the published data [71, 210]. However, focusing using only one lens limited us to fully utilise the pump power available. The pump lost its power by a factor of 2, largely due to beam clipping. In addition, the Co/Pt saturated at low pump energy, even ablated at only 45 μJ. This was because of the small pump beam ($\sim$1.5-2 mm diameter) resulting in a very high fluence >3 mJ/cm^2. The current
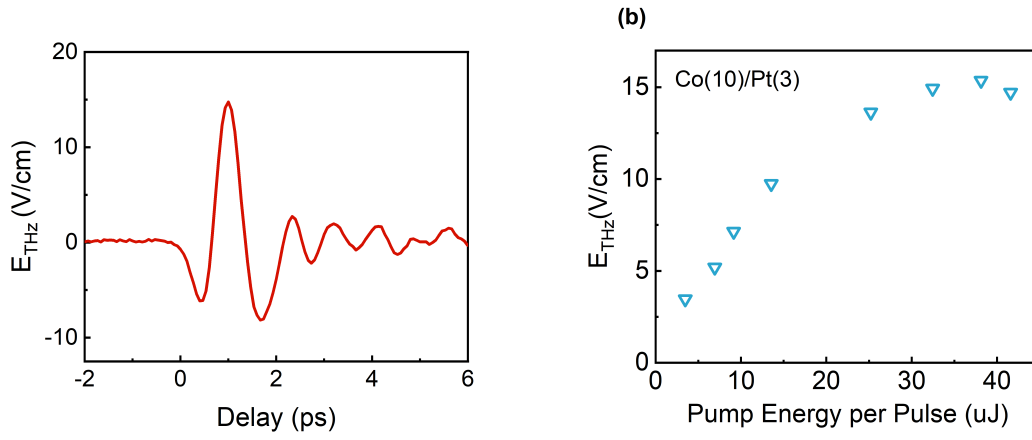
Figure E.1: (a) Time domain (b) frequency domain data of THz emitted by the Co(10)/Pt(3) on glass substrate, pumped with 25 μJ energy per pulse. The pump is focused using one lens (Thorlabs LA1464-B)

lens hence needed to be replaced.

Appendix F

Two-lens system for pump beam in THz emission

The new pump beam focusing system is a Galilean telescope, which consists of a plano-convex lens (EksmaOptics 110-1519ET+ UBBAR) and a concave lens (EksmaOptics 112-1110ET+ UBBAR). The plano-convex lens focuses the beam, and the concave lens, placed before the focal point of the first lens, collimates the beam. To achieve this, the distance between the two lenses is $L = f_{convex} - |f_{concave}|$. The lenses are designed for femtosecond laser pulses, having 1-3 mm thick to minimise pulse stretching, and high damage threshold up to 50 mJ/cm^2. Coating of the lenses are suitable for 350-900 nm wavelengths.

The new focusing telescope increased the THz emission signal by almost a factor of 2 for a constant pump energy per pulse [Figure F.1]. The telescope system enabled exciting bigger area of the Co/Pt, generating higher THz pulse energy with less beam divergence. The frequency domain data showed the expected bandwidth up to 3 THz as well. Using the telescope system also minimised the beam clipping in the 2nd OAP mirror. The telescope system addressed the problems occurred in the previous version of THz emission setup.

Emission from Co(5)/Pt(3) and Co(3)/Pt(5) were also measured, using the same 25 μJ pump energy per pulse. The Co(5)/Pt(3) emitted more than twice stronger THz than Co(10)/Pt(3), agreeing with previous studies [211]. Co(3)/Pt(5) generated stronger THz emission than Co(10)/Pt(3), but weaker than Co(5)/Pt(3). The optimum thickness for the Pt layer is about 3 nm, which is comparable with its spin diffusion length while still electrically resistive to generate strong THz electric

Figure F.1: A comparison between Co(10)/Pt(3) THz emission using (a) the one-lens system and (b) the two-lens system
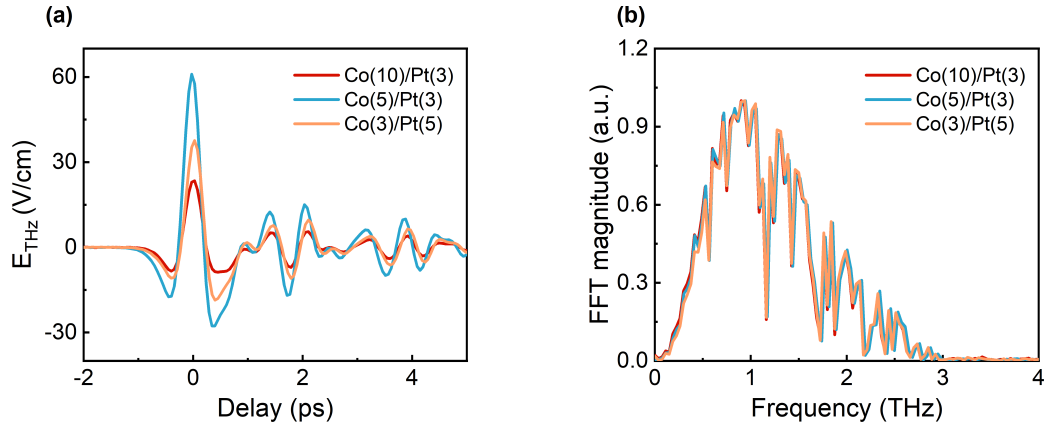
Figure F.2: A comparison between THz emitted from the Co(10)/Pt(3), Co(5)/Pt(3) and Co(3)/Pt(5), pumped with 25 μJ energy per pulse using the Galilean telescope in (a) time domain (b) frequency domain

field ($j = \sigma.E$) [160]. The frequency domain data of all three samples showed identical spectrum, even the absorption dips. The spectrum indeed should not depend on thickness. By successfully reproducing published research data with good repeatability, we concluded that our THz emission setup was ready for research purposes.

Appendix G

Code to calculate effective electron temperature by femtosecond laser excitation

```
function X = TimeDependentTe(To,flu)

%To in Kelvin
% flu is fluence in mJ/cm^2

y= 750;  % electron capacity constant Ce= y*Te
g=1*10^6; % electron phonon-coupling for Te<1000 K
Cph=2.85*10^6; % phonon heat capacity constant 3 Nkb
Td= 240; % Debye temperature of Platinum
Uabs= flu*10/(5*10^-9); %converting to J.m^-2 and divided by Pt (5 nm)


Upho = Cph*To*((19.517-3.1264*(Td/To)+0.149779*(Td/To)^2))
/(19.539+3.9827*Td/To+(Td/To)^2);
% initialise phonon heat tempeature using Debye model

Te= zeros(200,1); %array for electron temperature
Tp= zeros(200,1); %array for phonon temperature
```

```
t= zeros(200,1);  %array for time
Cp=zeros(200,1);  %array for phonon heat capacity
dT=zeros(200,1);  %array for Te - Tp


Teo=((2*Uabs/y)+(To)^2)^0.5;
% initial electron temperature after all fluences absorbed
% approximation of electron-phonon coupling at the first 0.1 ps,
% coefficient 0.52 is to take into account the electron-phonon coupling
% the coefficient is calculated by comparison with atomic simulation
% provided by Seifert et. al. 2018

Te(1)=To+(Teo-To)*0.52;
Tp(1)=To;
t(1)=0;
Cp(1)=Upho/To;
dT(1)=Te(1)-To;

%constants for calculating phonon temperature Tp
I= 3953.632;
J= 682.0012;
K= 143.155337;
L= 15.121491;
M= 3953.632;
N= -800.6087;
O= 85.07724;
P= -4.432582;
Q= 0.0946173;

for i=2:200

% calculating of phonon temperature using third-order Debye function
Uph = Upho+Uabs-0.5*y*(Te(i-1)^2-To^2);
B= Cph/Uph;
```

```
a= B*M;
b= B*N*Td - I;
c= B*O*Td^2 - J*Td;
d= B*P*Td^3 - K*Td^2;
e= B*Q*Td^4 - L*Td^3;
f= -Td^4;


p = [a b c d e f];
R=roots(p);

% calculating of subsequent electron temperature and Te-Tp
for n=1:3
    if Tp(i)<real(R(n))
        Tp(i)=real(R(n));
        % selecting the real solution of Tp from the polynomial equation
    end
end
t(i)=0.01*(i-1); % time step of 0.01 ps
Te(i)= Te(i-1)-g*(Te(i-1)-Tp(i))/(y*Te(i-1))*0.01; % new Te
Cp(i)=Uph/Tp(i); % new phonon heat capacity
dT(i)=Te(i)-To;  % the interfacial temperature gradient

end


X = plot (t, dT);
end
```

Appendix H

Time domain THz emission data in YIG/Pt
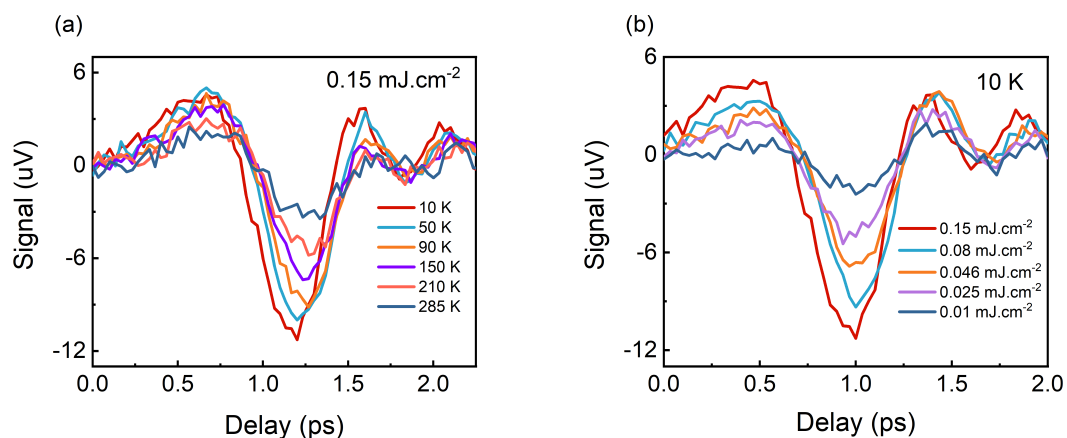
Figure H.1: Time domain data of THz emission from YIG/Pt for varying (a) temperature at 0.15 mJ/cm^2 and (b) pump fluence at a constant temperature 10 K

Appendix I

Time domain THz emission data in KNiF$_3$/Pt
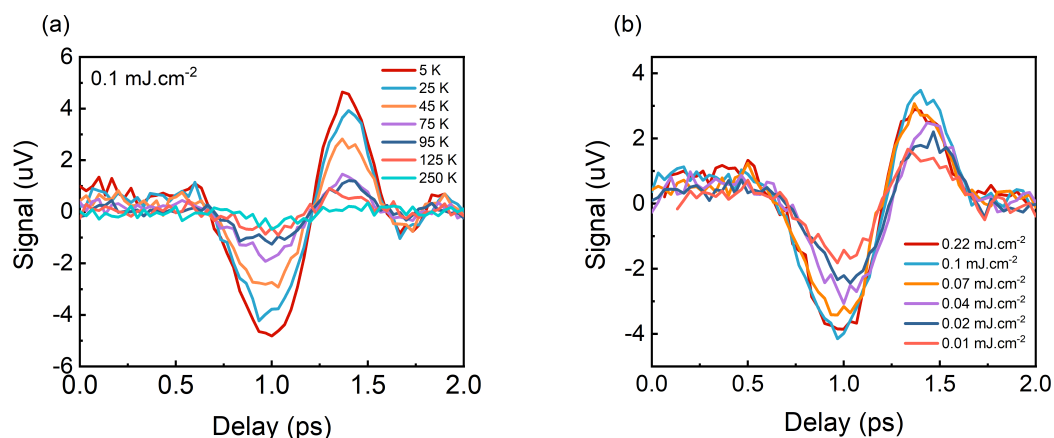
Figure I.1: Time domain data of THz emission from KNiF$_3$/Pt for varying (a) temperature at 0.15 mJ/cm^2 and (b) pump fluence at a constant temperature 10 K

Appendix J

Time domain THz emission data in KCoF$_3$/Pt
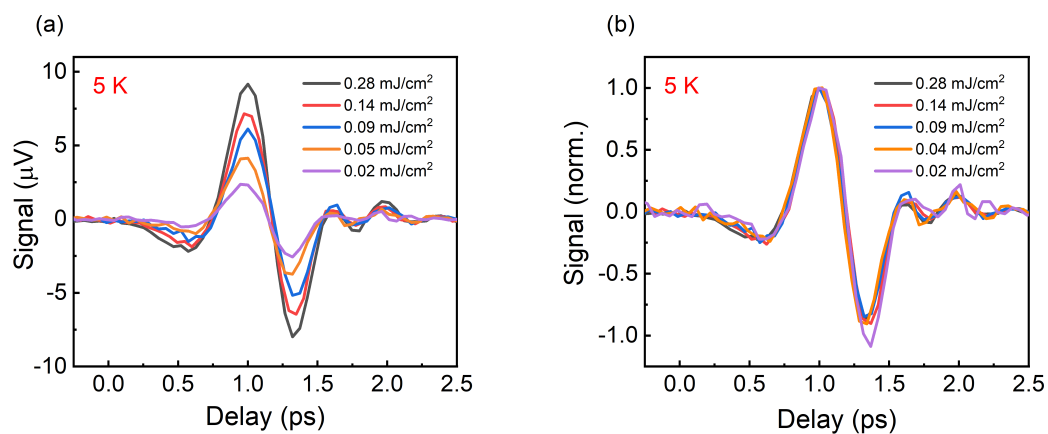
Figure J.1: (a) Raw and (b) normalised time domain data of THz emission from KCoF$_3$/Pt for varying pump fluence at 5 K
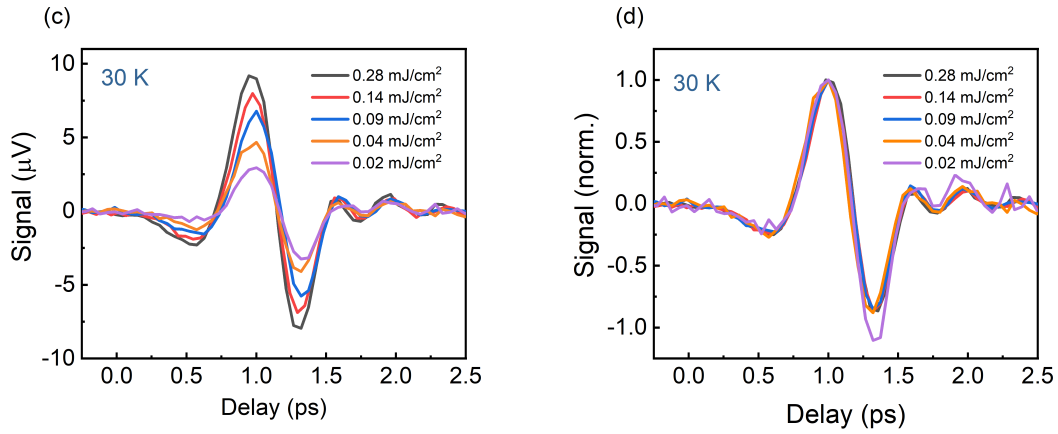
Figure J.2: (a) Raw and (b) normalised time domain data of THz emission from KCoF$_3$/Pt for varying pump fluence at 30 K
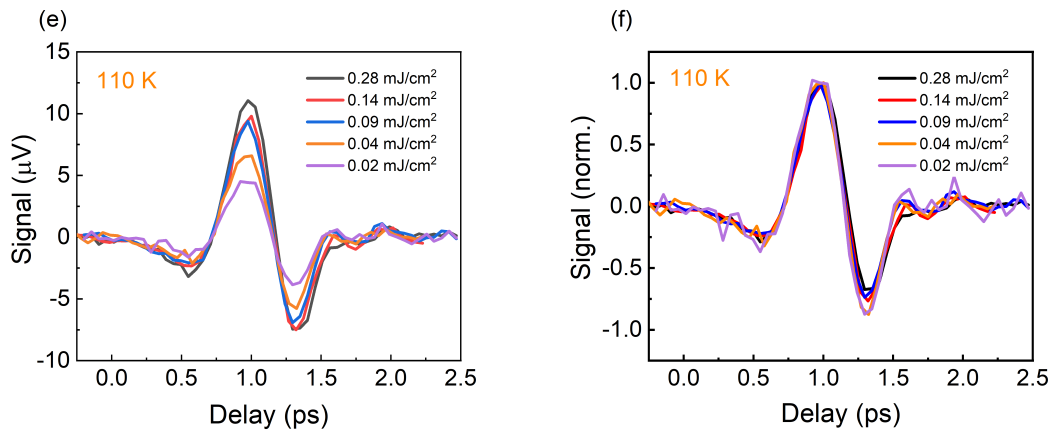
Figure J.3: (a) Raw and (b) normalised time domain data of THz emission from KCoF$_3$/Pt for varying pump fluence at 110 K

Bibliography

[1] M. Julliere, "Tunneling between ferromagnetic films," *Physics Letters A*, vol. 54, no. 3, pp. 225–226, 1975.

[2] Y. Re and R. H. Johnson, Mark; Silsbee, "Interfacial Charge-Spin Coupling: Injection and Detection of Spin Magnetization in Metals," *Physical Review Letters*, vol. 55, no. 17, pp. 1790–1793, 1985.

[3] M. N. Baibich, J. M. Broto, A. Fert, F. N. Van Dau, F. Petroff, P. Eitenne, G. Creuzet, A. Friederich, and J. Chazelas, "Giant magnetoresistance of (001)Fe/(001)Cr magnetic superlattices," *Physical Review Letters*, vol. 61, no. 21, pp. 2472–2475, 1988.

[4] I. Zutic, J. Fabian, and S. Das Sarma, "Spintronics: Fundamentals and applications," *Reviews of Modern Physics*, vol. 76, no. 2, pp. 322–410, 2004.

[5] S. A. Wolf, D. D. Awschalom, R. A. Buhrman, J. M. Daughton, S. von Molnar, M. L. Roukes, A. Y. Chtchelkanova, and D. M. Treger, "159_Spintronics-A Spin-Based Electronics vision for the future_S.A.Wolf_Science," *Science*, vol. 294, no. 5546, pp. 1488–1495, 2001.

[6] A. Fert, "Origin, development, and future of spintronics (Nobel lecture)," *Angewandte Chemie - International Edition*, vol. 47, no. 32, pp. 5956–5967, 2008.

[7] J. Mathon and A. Umerski, "Theory of tunneling magnetoresistance of an epitaxial Fe/MgO/Fe(001) junction," *Physical Review B - Condensed Matter and Materials Physics*, vol. 63, no. 22, pp. 1–4, 2001.

[8] N. Nishimura, T. Hirai, A. Koganei, T. Ikeda, K. Okano, Y. Sekiguchi, and Y. Osada, "Magnetic tunnel junction device with perpendicular magnetization

films for high-density magnetic random access memory," *Journal of Applied Physics*, vol. 91, no. 8, pp. 5246–5249, 2002.

[9] S. S. Parkin, C. Kaiser, A. Panchula, P. M. Rice, B. Hughes, M. Samant, and S. H. Yang, "Giant tunnelling magnetoresistance at room temperature with MgO (100) tunnel barriers," *Nature Materials*, vol. 3, no. 12, pp. 862–867, 2004.

[10] Y. Sakuraba, M. Hattori, M. Oogane, Y. Ando, H. Kato, A. Sakuma, T. Miyazaki, and H. Kubota, "Giant tunneling magnetoresistance in Co2MnSi/Al-O /Co 2MnSi magnetic tunnel junctions," *Applied Physics Letters*, vol. 88, no. 19, pp. 10–13, 2006.

[11] S. Ikeda, K. Miura, H. Yamamoto, K. Mizunuma, H. D. Gan, M. Endo, S. Kanai, J. Hayakawa, F. Matsukura, and H. Ohno, "A perpendicular-anisotropy CoFeB-MgO magnetic tunnel junction," *Nature Materials*, vol. 9, no. 9, pp. 721–724, 2010.

[12] W. G. Wang, M. Li, S. Hageman, and C. L. Chien, "Electric-field-assisted switching in magnetic tunneljunctions," *Nature Materials*, vol. 11, no. 1, pp. 64–68, 2012.

[13] S. S. P. Parkin, R. Bhadra, and K. P. Roche, "Oscillatory Magnetic Exchange Coupling through Thin Copper Layers," *Physical Review Letters*, vol. 66, no. 16, pp. 2152–2155, 1991.

[14] S. S. Parkin, N. More, and K. P. Roche, "Oscillations in exchange coupling and magnetoresistance in metallic superlattice structures: Co/Ru, Co/Cr, and Fe/Cr," *Physical Review Letters*, vol. 64, no. 19, pp. 2304–2307, 1990.

[15] S. S. Parkin, "Systematic variation of the strength and oscillation period of indirect magnetic exchange coupling through the 3d, 4d, and 5d transition metals," *Physical Review Letters*, vol. 67, no. 25, pp. 3598–3601, 1991.

[16] P. Bruno and C. Chappert, "Oscillatory coupling between ferromagnetic layers separated by a nonmagnetic metal spacer," *Physical Review Letters*, vol. 67, no. 12, pp. 1602–1605, 1991.

[17] P. P. Freitas and L. Berger, "Observation of s-d exchange force between domain walls and electric current in very thin Permalloy films," *Journal of Applied Physics*, vol. 57, no. 4, pp. 1266–1269, 1985.

[18] C. Y. Hung and L. Berger, "Exchange forces between domain wall and electric current in permalloy films of variable thickness," *Journal of Applied Physics*, vol. 63, no. 8, pp. 4276–4278, 1988.

[19] K. L. Wang, J. G. Alzate, and P. Khalili Amiri, "Low-power non-volatile spintronic memory: STT-RAM and beyond," *Journal of Physics D: Applied Physics*, vol. 46, no. 8, 2013.

[20] S. Tehrani, J. M. Slaughter, M. DeHerrera, B. N. Engel, N. D. Rizzo, J. Salter, M. Durlam, R. W. Dave, J. Janesky, B. Butcher, K. Smith, and G. Grynkewich, "Magnetoresistive random access memory using magnetic tunnel junctions," *Proceedings of the IEEE*, vol. 91, no. 5, pp. 703–712, 2003.

[21] B. N. Engel, J. Akerman, B. Butcher, R. W. Dave, M. DeHerrera, M. Durlam, G. Grynkewich, J. Janesky, S. V. Pietambaram, N. D. Rizzo, J. M. Slaughter, K. Smith, J. J. Sun, and S. Tehran, "A 4-Mb toggle MRAM based on a novel bit and switching method," *IEEE Transactions on Magnetics*, vol. 41, no. 1 I, pp. 132–136, 2005.

[22] J. C. Slonczewski, "Current-driven excitation of magnetic multilayers," *Journal of Magnetism and Magnetic Materials*, vol. 159, no. 1-2, 1996.

[23] L. Berger, "Emission of spin waves by a magnetic multilayer traversed by a current," *Physical Review B*, vol. 54, no. 13, pp. 9353–9358, 1996.

[24] E. B. Myers, "Current-Induced Switching of Domains in Magnetic Multilayer Devices," *Science*, vol. 285, no. 5429, pp. 867–870, 1999.

[25] J. Katine, F. Albert, R. Buhrman, E. Myers, and D. Ralph, "Current-Driven Magnetization Reversal and Spin-Wave Excitations in Co /Cu /Co Pillars," *Physical Review Letters*, vol. 84, no. 14, pp. 3149–3152, 2000.

[26] S. I. Klselev, J. C. Sankey, I. N. Krivorotov, N. C. Emley, R. J. Schoelkopf, R. A. Buhrman, and D. C. Ralph, "Microwave oscillations of a nanomagnet

driven by a spin-polarized current," *Nature*, vol. 425, no. 6956, pp. 380–383, 2003.

[27] J. E. Hirsch, "Spin Hall Effect," *Physical Review Letters*, vol. 83, no. 9, pp. 1834–1837, 1999.

[28] J. Sinova, D. Culcer, Q. Niu, N. A. Sinitsyn, T. Jungwirth, and A. H. Macdonald, "Universal Intrinsic Spin Hall Effect," *Physical Review Letters*, vol. 92, no. 12, pp. 1–4, 2004.

[29] Y. K. Kato, R. C. Myers, A. C. Gossard, and D. D. Awschalom, "Observation of the Spin Hall Effect in Semiconductors," *Science*, vol. 306, no. 5703, pp. 1910–1913, 2004.

[30] J. Wunderlich, B. Kaestner, J. Sinova, and T. Jungwirth, "Experimental Observation of the Spin-Hall Effect in a Two-Dimensional Spin-Orbit Coupled Semiconductor System," *Physical Review Letters*, vol. 94, no. 047204, pp. 1–4, 2005.

[31] J. Sinova, S. O. Valenzuela, J. Wunderlich, C. H. Back, and T. Jungwirth, "Spin Hall effects," *Reviews of Modern Physics*, vol. 87, no. 4, pp. 1213–1260, 2015.

[32] E. Saitoh, M. Ueda, H. Miyajima, and G. Tatara, "Conversion of spin current into charge current at room temperature: Inverse spin-Hall effect," *Applied Physics Letters*, vol. 88, no. 18, pp. 1–4, 2006.

[33] I. Mihai Miron, G. Gaudin, S. Auffret, B. Rodmacq, A. Schuhl, S. Pizzini, J. Vogel, and P. Gambardella, "Current-driven spin torque induced by the Rashba effect in a ferromagnetic metal layer," *Nature Materials*, vol. 9, no. 3, pp. 230–234, 2010.

[34] L. Liu, T. Moriyama, D. C. Ralph, and R. A. Buhrman, "Spin-torque ferromagnetic resonance induced by the spin Hall effect," *Physical Review Letters*, vol. 106, no. 3, pp. 1–4, 2011.

[35] K. Ando, S. Takahashi, J. Ieda, Y. Kajiwara, H. Nakayama, T. Yoshino, K. Harii, Y. Fujikawa, M. Matsuo, S. Maekawa, and E. Saitoh, "Inverse spin-

Hall effect induced by spin pumping in metallic system," *Journal of Applied Physics*, vol. 109, no. 10, 2011.

[36] G. E. Bauer, E. Saitoh, and B. J. Van Wees, "Spin caloritronics," *Nature Materials*, vol. 11, no. 5, pp. 391–399, 2012.

[37] Y. Tserkovnyak, A. Brataas, and G. E. W. Bauer, "Enhanced Gilbert Damping in Thin Ferromagnetic Films," *Physical Review Letters*, vol. 88, no. 11, pp. 1–4, 2001.

[38] Y. Tserkovnyak, A. Brataas, and G. E. W. Bauer, "Spin pumping and magnetization dynamics in metallic multilayers," *Physical Review Letters*, vol. 66, no. 224403, pp. 1–10, 2002.

[39] P. W. Brouwer, "Scattering approach to parametric pumping," *Physical Review B*, vol. 58, no. 16, pp. 135–138, 1998.

[40] S. Mizukami, Y. Ando, and T. Miyazaki, "Ferromagnetic resonance linewidth for NM / 80NiFe / NM films (NM " Cu , Ta , Pd and Pt)," *Journal of Magnetism and Magnetic Materials*, vol. 226-230, pp. 1640–1642, 2001.

[41] K. I. Uchida, H. Adachi, T. Ota, H. Nakayama, S. Maekawa, and E. Saitoh, "Observation of longitudinal spin-Seebeck effect in magnetic insulators," *Applied Physics Letters*, vol. 97, no. 17, 2010.

[42] A. Kirilyuk, A. V. Kimel, and T. Rasing, "Ultrafast optical manipulation of magnetic order," *Reviews of Modern Physics*, vol. 82, no. 3, pp. 2731–2784, 2010.

[43] T. Jungwirth, X. Marti, P. Wadley, and J. Wunderlich, "Antiferromagnetic spintronics," 3 2016.

[44] P. L. Richards, "Far-infrared magnetic resonance in CoF2, NiF2, KNiF3, and YbIG," *Journal of Applied Physics*, vol. 34, no. 4, pp. 1237–1238, 1963.

[45] R. A. Cowley, W. J. L. Buyers, D. Bloor, and G. M. Copland, "Excitations in KCoF3-I. Experimental," *J. Phys. C: So!id St. Phys.*, vol. 4, pp. 2127–2138, 1971.

[46] P. Vaidya, S. A. Morley, J. van Tol, Y. Liu, R. Cheng, A. Brataas, D. Lederman, and E. Del Barco, "Subterahertz spin pumping from an insulating antiferromagnet.," *Science*, vol. 368, no. 6487, pp. 160–165, 2020.

[47] J. Li, C. B. Wilson, R. Cheng, M. Lohmann, M. Kavand, W. Yuan, M. Aldosary, N. Agladze, P. Wei, M. S. Sherwin, and J. Shi, "Spin current from subterahertz-generated antiferromagnetic magnons," *Nature*, vol. 578, no. 7793, pp. 70–74, 2020.

[48] P. Nemec, M. Fiebig, T. Kampfrath, and A. V. Kimel, "Antiferromagnetic opto-spintronics," *Nature Physics*, vol. 14, no. 3, pp. 229–241, 2018.

[49] Nogues J, Schuller I K, "Exchange bias," *Journal of Magnetism and Magnetic Materials*, vol. 192, no. 2, pp. 203–232, 1999.

[50] E. Beaurepaire, J.-C. Merle, A. Daunois, and J.-Y. Bigot, "Ultrafast Spin Dynamics in Ferromagnetic Nickel," *Physical Review Letters*, vol. 76, no. 22, pp. 4250–4253, 1996.

[51] A. V. Kimel, A. A. Tsvetkov, A. Kirilyuk, T. Rasing, and V. N. Gridnev, "Picosecond dynamics of bleaching and spin splitting in InP revealed by the photoinduced magneto-optical Kerr effect near the spin-orbit split-off exciton transition," *Physical Review B - Condensed Matter and Materials Physics*, vol. 69, no. 16, pp. 1–5, 2004.

[52] C. D. Stanciu, F. Hansteen, A. V. Kimel, A. Kirilyuk, A. Tsukamoto, A. Itoh, and T. Rasing, "All-optical magnetic recording with circularly polarized light," *Physical Review Letters*, vol. 99, no. 4, pp. 1–4, 2007.

[53] L. Le Guyader, S. El Moussaoui, M. Buzzi, M. Savoini, A. Tsukamoto, A. Itoh, A. Kirilyuk, T. Rasing, F. Nolting, and A. V. Kimel, "Deterministic character of all-optical magnetization switching in GdFe-based ferrimagnetic alloys," *Physical Review B - Condensed Matter and Materials Physics*, vol. 93, no. 13, pp. 1–9, 2016.

[54] L. L. Guyader, M. Savoini, S. E. Moussaoui, M. Buzzi, A. Tsukamoto, A. Itoh, A. Kirilyuk, T. Rasing, A. V. Kimel, and F. Nolting, "Nanoscale sub-100

picosecond all-optical magnetization switching in GdFeCo microstructures," *Nature Communications*, vol. 6, no. 5839, pp. 1–6, 2015.

[55] A. Stupakiewicz, K. Szerenos, D. Afanasiev, A. Kirilyuk, and A. V. Kimel, "Ultrafast nonthermal photo-magnetic recording in a transparent medium," *Nature*, vol. 542, no. 7639, pp. 71–74, 2017.

[56] A. V. Kimel, A. Kirilyuk, P. A. Usachev, R. V. Pisarev, A. M. Balbashov, and T. Rasing, "Ultrafast non-thermal control of magnetization by instantaneous photomagnetic pulses," *Nature*, vol. 435, no. 7042, pp. 655–657, 2005.

[57] T. Satoh, S. J. Cho, R. Iida, T. Shimura, K. Kuroda, H. Ueda, Y. Ueda, B. A. Ivanov, F. Nori, and M. Fiebig, "Spin oscillations in antiferromagnetic NiO triggered by circularly polarized light," *Physical Review Letters*, vol. 105, no. 7, pp. 1–4, 2010.

[58] T. Kampfrath, A. Sell, G. Klatt, A. Pashkin, S. Mährlein, T. Dekorsy, M. Wolf, M. Fiebig, A. Leitenstorfer, and R. Huber, "Coherent terahertz control of antiferromagnetic spin waves," *Nature Photonics*, vol. 5, no. 1, pp. 31–34, 2011.

[59] R. Mikhaylovskiy, E. Hendry, A. Secchi, J. Mentink, M. Eckstein, A. Wu, R. Pisarev, V. Kruglyak, M. Katsnelson, T. Rasing, and A. Kimel, "Ultrafast optical modification of exchange interactions in iron oxides," *Nature Communications*, vol. 6, p. 8190, 2015.

[60] G. Batignani, D. Bossini, N. Di Palo, C. Ferrante, E. Pontecorvo, G. Cerullo, A. Kimel, and T. Scopigno, "Probing ultrafast photo-induced dynamics of the exchange energy in a Heisenberg antiferromagnet," *Nature Photonics*, vol. 9, no. 8, pp. 506–510, 2015.

[61] B. Koopmans, G. Malinowski, F. Dalla Longa, D. Steiauf, M. Fähnle, T. Roth, M. Cinchetti, and M. Aeschlimann, "Explaining the paradoxical diversity of ultrafast laser-induced demagnetization," *Nature Materials*, vol. 9, no. 3, pp. 259–265, 2010.

[62] M. Battiato, K. Carva, and P. M. Oppeneer, "Superdiffusive spin transport as a mechanism of ultrafast demagnetization," *Physical Review Letters*, vol. 105, no. 2, pp. 1–4, 2010.

[63] M. Battiato, K. Carva, and P. M. Oppeneer, "Theory of laser-induced ultrafast superdiffusive spin transport in layered heterostructures," *Physical Review B - Condensed Matter and Materials Physics*, vol. 86, no. 2, pp. 1–16, 2012.

[64] Z. Jin, A. Tkach, F. Casper, V. Spetter, H. Grimm, A. Thomas, T. Kampfrath, M. Bonn, M. Kläui, and D. Turchinovich, "Accessing the fundamentals of magnetotransport in metals with terahertz probes," *Nature Physics*, vol. 11, no. 9, pp. 761–766, 2015.

[65] T. J. Huisman, R. V. Mikhaylovskiy, T. Rasing, A. V. Kimel, A. Tsukamoto, B. De Ronde, L. Ma, W. J. Fan, and S. M. Zhou, "Sub-100-ps dynamics of the anomalous Hall effect at terahertz frequencies," *Physical Review B*, vol. 95, no. 9, pp. 1–8, 2017.

[66] S. Baierl, J. H. Mentink, M. Hohenleutner, L. Braun, T. M. Do, C. Lange, A. Sell, M. Fiebig, G. Woltersdorf, T. Kampfrath, and R. Huber, "Terahertz-Driven Nonlinear Spin Response of Antiferromagnetic Nickel Oxide," *Physical Review Letters*, vol. 117, no. 19, pp. 1–6, 2016.

[67] S. Baierl, M. Hohenleutner, T. Kampfrath, A. K. Zvezdin, A. V. Kimel, R. Huber, and R. V. Mikhaylovskiy, "Nonlinear spin control by terahertz-driven anisotropy fields," *Nature Photonics*, vol. 10, no. 11, pp. 715–718, 2016.

[68] Y. Mukai, H. Hirori, T. Yamamoto, H. Kageyama, and K. Tanaka, "Nonlinear magnetization dynamics of antiferromagnetic spin resonance induced by intense terahertz magnetic field," *New Journal of Physics*, vol. 18, no. 1, 2016.

[69] J. Lu, X. Li, H. Y. Hwang, B. K. Ofori-Okai, T. Kurihara, T. Suemoto, and K. A. Nelson, "Coherent Two-Dimensional Terahertz Magnetic Resonance Spectroscopy of Collective Spin Waves," *Physical Review Letters*, vol. 118, no. 20, pp. 1–6, 2017.

[70] T. Kampfrath, M. Battiato, P. Maldonado, G. Eilers, J. Nötzold, S. Mährlein, V. Zbarsky, F. Freimuth, Y. Mokrousov, S. Blügel, M. Wolf, I. Radu, P. M. Oppeneer, and M. Münzenberg, "Terahertz spin current pulses controlled by magnetic heterostructures," *Nature Nanotechnology*, vol. 8, no. 4, pp. 256–260, 2013.

[71] T. J. Huisman, R. V. Mikhaylovskiy, J. D. Costa, F. Freimuth, E. Paz, J. Ventura, P. P. Freitas, S. Blügel, Y. Mokrousov, T. Rasing, and A. V. Kimel, "Femtosecond control of electric currents at the interfaces of metallic ferromagnetic heterostructures," *Nature Nanotechnology*, vol. 11, no. 5, pp. 455–458, 2015.

[72] T. S. Seifert, S. Jaiswal, J. Barker, S. T. Weber, I. Razdolski, J. Cramer, O. Gueckstock, S. F. Maehrlein, L. Nadvornik, S. Watanabe, C. Ciccarelli, A. Melnikov, G. Jakob, M. Münzenberg, S. T. Goennenwein, G. Woltersdorf, B. Rethfeld, P. W. Brouwer, M. Wolf, M. Kläui, and T. Kampfrath, "Femtosecond formation dynamics of the spin Seebeck effect revealed by terahertz spectroscopy," *Nature Communications*, vol. 9, no. 1, pp. 1–11, 2018.

[73] H. Adachi, K. I. Uchida, E. Saitoh, and S. Maekawa, "Theory of the spin Seebeck effect," *Reports on Progress in Physics*, vol. 76, no. 3, p. 036501, 2013.

[74] M. Schreier, A. Kamra, M. Weiler, J. Xiao, G. E. Bauer, R. Gross, and S. T. Goennenwein, "Magnon, phonon, and electron temperature profiles and the spin Seebeck effect in magnetic insulator/normal metal hybrid structures," *Physical Review B - Condensed Matter and Materials Physics*, vol. 88, no. 9, pp. 1–13, 2013.

[75] P. A. M. Dirac and N. H. D. Bohr, "The quantum theory of the emission and absorption of radiation," *Proc. R. Soc. Lond.*, vol. 114, no. 767, pp. 243–265, 1927.

[76] W. T. Silfvast, "Conditions for Producing a Laser – Population Inversions, Gain, and Gain Saturation," in *Laser Fundamentals*, pp. 225–254, Cambridge University Press, 2013.

[77] U. Keller, "Recent developments in compact ultrafast lasers," *Nature*, vol. 424, no. August, pp. 831–838, 2003.

[78] Y. R. Shen, *The principles of nonlinear optics*. New Yorl: John Wiley & Sons, 1984.

[79] M. Bass, P. A. Franken, F. Ward, and G. Weinreich, "Opical Rectification," *Physical Review Letters*, vol. 9, no. 11, pp. 28–31, 1962.

[80] A. Rice, Y. Jin, X. F. Ma, X. C. Zhang, D. Bliss, J. Larkin, and M. Alexander, "Terahertz optical rectification from ¡110¿ zinc-blende crystals," *Applied Physics Letters*, vol. 64, no. 11, pp. 1324–1326, 1994.

[81] J. Hebling, K.-L. Yeh, M. C. Hoffmann, B. Bartal, and K. A. Nelson, "Generation of high-power terahertz pulses by tilted-pulse-front excitation and their application possibilities," *Journal of the Optical Society of America B*, vol. 25, no. 7, p. B6, 2008.

[82] G. Gallot and D. Grischkowsky, "Electro-optic detection of terahertz radiation," *Journal of the Optical Society of America B*, vol. 16, no. 8, p. 1204, 1999.

[83] P. Kužel, M. A. Khazan, and J. Kroupa, "Spatiotemporal transformations of ultrashort terahertz pulses," *Journal of the Optical Society of America B*, vol. 16, no. 10, p. 1795, 1999.

[84] E. Gamaly, *Femtosecond Laser–Matter Interactions: Theory, Experiments and Applications*. Jenny Stanford Publishing, 2011.

[85] J. J. Quinn and R. A. Ferrell, "Electron self-energy approach to correlation in a degenerate electron gas," *Physical Review*, vol. 112, no. 3, pp. 812–827, 1958.

[86] S. D. Brorson, J. G. Fujimoto, and E. P. Ippen, "Femtosecond electronic heat-transport dynamics in thin gold films," *Physical Review Letters*, vol. 59, no. 17, pp. 1962–1965, 1987.

[87] L. T. M.I. Kaganov, I.M. Lifshitz, "Relaxation between Electrons and the Crystalline Lattice," *Soviet Journal of Experimental and Theoretical Physics*, vol. 4, no. 9, p. 173, 1955.

[88] Z. Y. Wang, D. M. Riffe, Y. S. Lee, and M. C. Downer, "Time-resolved electron-temperature measurement in a highly excited gold target using femtosecond thermionic emission," *Physical Review B*, vol. 50, no. 11, pp. 8016–8019, 1994.

[89] Z. Lin, L. V. Zhigilei, and V. Celli, "Electron-phonon coupling and electron heat capacity of metals under conditions of strong electron-phonon nonequilibrium," *Physical Review B - Condensed Matter and Materials Physics*, vol. 77, no. 7, pp. 1–17, 2008.

[90] B. Koopmans, J. J. Ruigrok, F. Dalla Longa, and W. J. De Jonge, "Unifying ultrafast magnetization dynamics," *Physical Review Letters*, vol. 95, no. 26, pp. 1–4, 2005.

[91] M. Kraub, T. Roth, S. Alebrand, D. Steil, M. Cinchetti, M. Aeschlimann, and H. C. Schneider, "Ultrafast demagnetization of ferromagnetic transition metals: The role of the Coulomb interaction," *Physical Review B - Condensed Matter and Materials Physics*, vol. 80, no. 18, pp. 1–4, 2009.

[92] E. Carpene, E. Mancini, C. Dallera, M. Brenna, E. Puppin, and S. De Silvestri, "Dynamics of electron-magnon interaction and ultrafast demagnetization in thin iron films," *Physical Review B - Condensed Matter and Materials Physics*, vol. 78, no. 17, pp. 1–6, 2008.

[93] H. E. Elsayed-Ali, T. B. Norris, M. A. Pessot, and G. A. Mourou, "Time-resolved observation of electron-phonon relaxation in copper," *Physical Review Letters*, vol. 58, no. 12, pp. 1212–1215, 1987.

[94] R. W. Schoenlein, W. Z. Lin, J. G. Fujimoto, and G. L. Eesley, "Femtosecond studies of nonequilibrium electronic processes in metals," *Physical Review Letters*, vol. 58, no. 16, pp. 1680–1683, 1987.

[95] P. S. Pershan, "Nonlinear optical properties of solids: energy considerations," *Physical Review*, vol. 130, no. 3, pp. 919–929, 1963.

[96] Y. X. Yan, E. B. Gamble, and K. A. Nelson, "Impulsive stimulated scattering: General importance in femtosecond laser pulse interactions with matter, and spectroscopic applications," *The Journal of Chemical Physics*, vol. 83, no. 11, pp. 5391–5399, 1985.

[97] W. J. L. Buyers, T. M. Holden, E. C. Svensson, S. A. Cowley, and M. T. Hutchings, "Excitations in KCoF3 II. Theoretical," *J. Phys. C: Solid St. Phys.*, vol. 4, pp. 2139–2159, 1971.

[98] S. F. Maehrlein, I. Radu, P. Maldonado, A. Paarmann, M. Gensch, A. M. Kalashnikova, R. V. Pisarev, M. Wolf, P. M. Oppeneer, J. Barker, and T. Kampfrath, "Dissecting spin-phonon equilibration in ferrimagnetic insulators by ultrafast lattice excitation," *Science Advances*, vol. 4, no. 7, 2018.

[99] N. Suzuki, T. Isu, and K. Motizuki, "Theoretical study of magnetic susceptibility of orbitally unquenched compound KCoF3," *Solid State Communications*, vol. 23, no. 5, pp. 319–322, 1977.

[100] J. Sinova, S. O. Valenzuela, J. Wunderlich, C. H. Back, and T. Jungwirth, "Spin Hall effect," *Nature Publishing Group*, vol. 11, no. 5, pp. 382–390, 2014.

[101] T. Tanaka, H. Kontani, M. Naito, T. Naito, D. S. Hirashima, K. Yamada, and J. Inoue, "Intrinsic spin Hall effect and orbital Hall effect in 4d and 5d transition metals," *Physical Review B - Condensed Matter and Materials Physics*, vol. 77, no. 16, pp. 1–16, 2008.

[102] H. A. Engel, B. I. Halperin, and E. I. Rashba, "Theory of spin hall conductivity in n-doped GaAs," *Physical Review Letters*, vol. 95, no. 16, pp. 1–4, 2005.

[103] G. Y. Guo, S. Maekawa, and N. Nagaosa, "Enhanced spin hall effect by resonant skew scattering in the orbital-dependent kondo effect," *Physical Review Letters*, vol. 102, no. 3, pp. 1–4, 2009.

[104] N. A. Sinitsyn, A. H. MacDonald, T. Jungwirth, V. K. Dugaev, and J. Sinova, "Anomalous Hall effect in a two-dimensional Dirac band: The link between the Kubo-Streda formula and the semiclassical Boltzmann equation approach," *Physical Review B - Condensed Matter and Materials Physics*, vol. 75, no. 4, pp. 1–17, 2007.

[105] N. Nagaosa, J. Sinova, S. Onoda, A. H. MacDonald, and N. P. Ong, "Anomalous Hall effect," *Reviews of Modern Physics*, vol. 82, no. 2, pp. 1539–1592, 2010.

[106] H. L. Wang, C. H. Du, Y. Pu, R. Adur, P. C. Hammel, and F. Y. Yang, "Scaling of spin hall angle in 3d, 4d, and 5d metals from Y3Fe5 O12 /metal spin pumping," *Physical Review Letters*, vol. 112, no. 19, pp. 1–5, 2014.

[107] K. Uchida, S. Takahashi, K. Harii, J. Ieda, W. Koshibae, K. Ando, S. Maekawa, and E. Saitoh, "Observation of the spin Seebeck effect," *Nature*, vol. 455, no. 7214, pp. 778–781, 2008.

[108] P. A. M. Dirac, "On the theory of quantum mechanics," *Proceedings of the Royal Society of London. Series A,*, vol. 112, no. 762, pp. 661–677, 1926.

[109] W. Heisenberg, "Zur Theorie des Ferromagnetismus," *Zeitschrift fur Physik*, vol. 49, pp. 619–636, 9 1928.

[110] L. Néel, *Influence des fluctuations du champ moléculaire sur les propriétés magnétiques des corps.* PhD thesis, Français, 1932.

[111] L. Neel., "Some New Results on Antiferromagnetism and Ferromagnetism," *Reviews of Modern Physics*, vol. 25, no. 1, pp. 58–63, 1953.

[112] L. Néel, "Antiferromagnetism and ferrimagnetism," *Proceedings of the Physical Society. Section A*, vol. 65, no. 11, pp. 869–885, 1952.

[113] A. Gurevich and G. Melkov, "Magnetization Oscillations and Waves," 1996.

[114] L. D. Landau and E. M. Lifshitz, "On the theory of the dispersion of magnetic permeability in ferromagnetic bodies," *Physikalische Zeitschrift der Sowjetunion*, vol. 8, p. 153, 1935.

[115] T. L. Gilbert, "A phenomenological theory of damping in ferromagnetic materials," *IEEE Transactions on Magnetics*, vol. 40, no. 6, pp. 3443–3449, 2004.

[116] C. Kittel, "On the theory of ferromagnetic resonance absorption," *Physical Review*, vol. 73, no. 2, pp. 155–161, 1948.

[117] C. Ciccarelli, K. M. D. Hals, A. Irvine, V. Novak, Y. Tserkovnyak, H. Kurebayashi, A. Brataas, and A. Ferguson, "Magnonic charge pumping via spin–orbit coupling," *Nature Nanotechnology*, vol. 10, no. 1, pp. 50–54, 2014.

[118] C. Ciccarelli, L. Anderson, V. Tshitoyan, A. J. Ferguson, F. Gerhard, C. Gould, L. W. Molenkamp, J. Gayles, J. Zelezny, L. Smejkal, Z. Yuan, J. Sinova, F. Freimuth, and T. Jungwirth, "Room-temperature spin-orbit torque in NiMnSb," *Nature Physics*, vol. 12, pp. 855–860, 2015.

[119] A. J. Princep, R. A. Ewings, S. Ward, S. Tóth, C. Dubs, D. Prabhakaran, and A. T. Boothroyd, "The full magnon spectrum of yttrium iron garnet," *npj Quantum Materials*, vol. 2, no. 1, pp. 1–5, 2017.

[120] S. M. Rezende, R. L. Rodríguez-Suárez, R. O. Cunha, A. R. Rodrigues, F. L. A. Machado, G. A. Fonseca Guerra, J. C. Lopez Ortiz, and A. Azevedo, "Magnon spin-current theory for the longitudinal spin-Seebeck effect," *Physical Review B - Condensed Matter and Materials Physics*, vol. 89, no. 1, pp. 1–10, 2014.

[121] F. Bloch, "Zur Theorie des Ferromagnetismus," *Zeitschrift fur Physik*, vol. 61, pp. 206–219, 3 1930.

[122] T. Holstein and H. Primakoff, "Field dependence of the intrinsic domain magnetization of a ferromagnet," *Physical Review*, vol. 58, no. 12, pp. 1098–1113, 1940.

[123] D. Bossini, *Femtosecond Optical Excitation of Spins in Antiferromagnetic fluorides An opto-magnetic journey from the center to the edges of the Brillouin zone.* 2016.

[124] R. Cheng, J. Xiao, Q. Niu, and A. Brataas, "Spin pumping and spin-transfer torques in antiferromagnets," *Physical Review Letters*, vol. 113, no. 5, pp. 1–5, 2014.

[125] F. K. Dejene, J. Flipse, and B. J. Van Wees, "Spin-dependent Seebeck coefficients of Ni 80Fe 20 and Co in nanopillar spin valves," *Physical Review B - Condensed Matter and Materials Physics*, vol. 86, no. 2, pp. 1–7, 2012.

[126] K. Uchida, T. Ota, H. Adachi, J. Xiao, T. Nonaka, Y. Kajiwara, G. E. Bauer, S. Maekawa, and E. Saitoh, "Thermal spin pumping and magnon-phonon-mediated spin-Seebeck effect," *Journal of Applied Physics*, vol. 111, no. 10, 2012.

[127] A. Kehlberger, U. Ritzmann, D. Hinzke, E. J. Guo, J. Cramer, G. Jakob, M. C. Onbasli, D. H. Kim, C. A. Ross, M. B. Jungfleisch, B. Hillebrands, U. Nowak, and M. Kläui, "Length Scale of the Spin Seebeck Effect," *Physical Review Letters*, vol. 115, no. 9, pp. 1–5, 2015.

[128] B. L. Giles, Z. Yang, J. S. Jamison, and R. C. Myers, "Long-range pure magnon spin diffusion observed in a nonlocal spin-Seebeck geometry," *Physical Review B - Condensed Matter and Materials Physics*, vol. 92, no. 22, pp. 1–13, 2015.

[129] T. Kikkawa, K. Shen, B. Flebus, R. A. Duine, K. I. Uchida, Z. Qiu, G. E. Bauer, and E. Saitoh, "Magnon polarons in the spin seebeck effect," *Physical Review Letters*, vol. 117, no. 20, pp. 1–6, 2016.

[130] L. J. Cornelissen, K. J. Peters, G. E. Bauer, R. A. Duine, and B. J. Van Wees, "Magnon spin transport driven by the magnon chemical potential in a magnetic insulator," *Physical Review B*, vol. 94, no. 1, pp. 1–16, 2016.

[131] E. J. Guo, J. Cramer, A. Kehlberger, C. A. Ferguson, D. A. MacLaren, G. Jakob, and M. Kläui, "Influence of thickness and interface on the low-temperature enhancement of the spin seebeck effect in YIG films," *Physical Review X*, vol. 6, no. 3, p. 31012, 2016.

[132] T. Kikkawa, K. I. Uchida, S. Daimon, Z. Qiu, Y. Shiomi, and E. Saitoh, "Critical suppression of spin Seebeck effect by magnetic fields," *Physical Review B - Condensed Matter and Materials Physics*, vol. 92, no. 6, pp. 1–9, 2015.

[133] H. Adachi, Y. Yamamoto, and M. Ichioka, "Spin Seebeck effect in a simple ferromagnet near T c: A Ginzburg-Landau approach," *Journal of Physics D: Applied Physics*, vol. 51, no. 14, 2018.

[134] K. Chen, W. Lin, C. L. Chien, and S. Zhang, "Temperature dependence of angular momentum transport across interfaces," *Physical Review B*, vol. 94, no. 5, p. 054413, 2016.

[135] S. Okamoto, "Spin injection and spin transport in paramagnetic insulators," *Physical Review B*, vol. 93, no. 6, p. 064421, 2016.

[136] S. M. Rezende, R. L. Rodríguez-Suárez, and A. Azevedo, "Theory of the spin Seebeck effect in antiferromagnets," *Physical Review B*, vol. 93, no. 1, pp. 1–9, 2016.

[137] A. Migus, A. Antonetti, J. Etchepare, D. Hulin, and A. Orszag, "Femtosecond spectroscopy with high-power tunable optical pulses," *Journal of the Optical Society of America B*, vol. 2, no. 4, p. 584, 1985.

[138] P. C. M. Planken, H.-K. Nienhuys, H. J. Bakker, and T. Wenckebach, "Measurement and calculation of the orientation dependence of terahertz pulse detection in ZnTe," *Journal of the Optical Society of America B*, vol. 18, no. 3, p. 313, 2001.

[139] M. Exter, C. Fattinger, and D. Grischkowsky, "Terahertz time-domain spectroscopy of water vapor.," *Optics letters*, vol. 14, no. 20, pp. 1128–30, 1989.

[140] C. Vicario, B. Monoszlai, C. Lombosi, A. Mareczko, A. Courjaud, J. A. Fülöp, and C. P. Hauri, "Pump pulse width and temperature effects in lithium niobate for efficient THz generation," *Optics Letters*, vol. 38, no. 24, p. 5373, 2013.

[141] J. A. Fülöp, Z. Ollmann, L. Pálfalvi, G. Almási, and J. Hebling, "Towards generation of mJ-level ultrashort THz pulses by optical rectification," *Optics InfoBase Conference Papers*, vol. 19, no. 16, pp. 15090–15097, 2011.

[142] C. A. Werley, S. M. Teo, and K. A. Nelson, "Pulsed laser noise analysis and pump-probe signal detection with a data acquisition card," *Review of Scientific Instruments*, vol. 82, no. 12, 2011.

[143] F. D. J. Brunner, J. A. Johnson, S. Grübel, A. Ferrer, S. L. Johnson, and T. Feurer, "Distortion-free enhancement of terahertz signals measured by electro-optic sampling I Theory," *Journal of the Optical Society of America B*, vol. 31, no. 4, p. 904, 2014.

[144] J. A. Johnson, F. D. J. Brunner, S. Grübel, A. Ferrer, S. L. Johnson, and T. Feurer, "Distortion-free enhancement of terahertz signals measured by electro-optic sampling II Experiment," *Journal of the Optical Society of America B*, vol. 31, no. 5, p. 1035, 2014.

[145] K. Olejník, T. Seifert, Z. Kašpar, V. Novák, P. Wadley, R. P. Campion, M. Baumgartner, P. Gambardella, P. Nemec, J. Wunderlich, J. Sinova, P. Kužel, M. Müller, T. Kampfrath, and T. Jungwirth, "Terahertz electrical writing speed in an antiferromagnetic memory," *Science Advances*, vol. 4, no. 3, pp. 1–9, 2018.

[146] H. Hirori, A. Doi, F. Blanchard, and K. Tanaka, "Single-cycle terahertz pulses with amplitudes exceeding 1 MV/cm generated by optical rectification in LiNbO3," *Applied Physics Letters*, vol. 98, no. 9, pp. 2–5, 2011.

[147] W. R. Huang, S. W. Huang, E. Granados, K. Ravi, K. H. Hong, L. E. Zapata, and F. X. Kärtner, "Highly efficient terahertz pulse generation by optical rectification in stoichiometric and cryo-cooled congruent lithium niobate," *Journal of Modern Optics*, vol. 62, no. 18, pp. 1486–1493, 2015.

[148] B. Monoszlai, C. Vicario, M. Jazbinsek, and C. P. Hauri, "High-energy terahertz pulses from organic crystals: DAST and DSTMS pumped at Ti:sapphire wavelength," *Optics Letters*, vol. 38, no. 23, p. 5106, 2013.

[149] C. Vicario, M. Jazbinsek, A. V. Ovchinnikov, O. V. Chefonov, S. I. Ashitkov, M. B. Agranat, and C. P. Hauri, "High efficiency THz generation in DSTMS, DAST and OH1 pumped by Cr:forsterite laser," *Optics Express*, vol. 23, no. 4, p. 4573, 2015.

[150] M. Savoini, L. Huber, H. Cuppen, E. Abreu, M. Kubli, M. J. Neugebauer, Y. Duan, P. Beaud, J. Xu, T. Rasing, and S. L. Johnson, "THz Generation and Detection by Fluorenone Based Organic Crystals," *ACS Photonics*, vol. 5, no. 3, pp. 671–677, 2018.

[151] D. Meier, D. Reinhardt, M. Van Straaten, C. Klewe, M. Althammer, M. Schreier, S. T. Goennenwein, A. Gupta, M. Schmid, C. H. Back, J. M. Schmalhorst, T. Kuschel, and G. Reiss, "Longitudinal spin Seebeck effect contribution in transverse spin Seebeck effect experiments in Pt/YIG and Pt/NFO," *Nature Communications*, vol. 6, pp. 1–7, 2015.

[152] K. i. Uchida, T. Kikkawa, A. Miura, J. Shiomi, and E. Saitoh, "Quantitative temperature dependence of longitudinal spin seebeck effect at high temperatures," *Physical Review X*, vol. 4, no. 4, pp. 1–9, 2014.

[153] D. Qu, S. Y. Huang, J. Hu, R. Wu, and C. L. Chien, "Intrinsic spin seebeck effect in Au/YIG," *Physical Review Letters*, vol. 110, no. 6, pp. 1–5, 2013.

[154] S. Hoffman, K. Sato, and Y. Tserkovnyak, "Landau-Lifshitz theory of the longitudinal spin Seebeck effect," *Physical Review B - Condensed Matter and Materials Physics*, vol. 88, no. 6, pp. 1–8, 2013.

[155] J. Kimling, G. M. Choi, J. T. Brangham, T. Matalla-Wagner, T. Huebner, T. Kuschel, F. Yang, and D. G. Cahill, "Picosecond Spin Seebeck Effect," *Physical Review Letters*, vol. 118, no. 5, p. 057201, 2017.

[156] T. Seifert, S. Jaiswal, U. Martens, J. Hannegan, L. Braun, P. Maldonado, F. Freimuth, A. Kronenberg, J. Henrizi, I. Radu, E. Beaurepaire, Y. Mokrousov, P. M. Oppeneer, M. Jourdan, G. Jakob, D. Turchinovich, L. M. Hayden, M. Wolf, M. Münzenberg, M. Kläui, and T. Kampfrath, "Efficient metallic spintronic emitters of ultrabroadband terahertz radiation," *Nature Photonics*, vol. 10, no. May, pp. 483–488, 2016.

[157] S. Geller and M. A. Gilleo, "The crystal structure and ferrimagnetism of yttrium-iron garnet, Y3Fe2(FeO4)3," *Journal of Physics and Chemistry of Solids*, vol. 3, no. 1-2, pp. 30–36, 1957.

[158] S. Pütter, S. Geprägs, R. Schlitz, M. Althammer, A. Erb, R. Gross, and S. T. Goennenwein, "Impact of the interface quality of Pt/YIG(111) hybrids on their spin Hall magnetoresistance," *Applied Physics Letters*, vol. 110, no. 1, 2017.

[159] M. B. Jungfleisch, V. Lauer, R. Neb, A. V. Chumak, and B. Hillebrands, "Improvement of the yttrium iron garnet/platinum interface for spin pumping-based applications," *Applied Physics Letters*, vol. 103, no. 2, 2013.

[160] M. H. Nguyen, D. C. Ralph, and R. A. Buhrman, "Spin Torque Study of the Spin Hall Conductivity and Spin Diffusion Length in Platinum Thin Films with Varying Resistivity," *Physical Review Letters*, vol. 116, no. 12, p. 126601, 2016.

[161] S. H. Wemple, S. L. Blank, J. A. Seman, and W. A. Biolsi, "Optical properties of epitaxial iron garnet thin films," *Physical Review B*, vol. 9, no. 5, pp. 2134–2144, 1974.

[162] M. C. Onbasli, L. Beran, M. Zahradník, M. Kucera, R. Antoš, J. Mistrík, G. F. Dionne, M. Veis, and C. A. Ross, "Optical and magneto-optical behavior of Cerium Yttrium Iron Garnet thin films at wavelengths of 200-1770 nm," *Scientific Reports*, vol. 6, no. December 2015, pp. 1–10, 2016.

[163] L. J. Krayer, J. Kim, and J. N. Munday, "Near-perfect absorption throughout the visible using ultra-thin metal films on index-near-zero substrates [Invited]," *Optical Materials Express*, vol. 9, no. 1, p. 330, 2019.

[164] T. S. Seifert, N. M. Tran, O. Gueckstock, S. M. Rouzegar, L. Nadvornik, S. Jaiswal, G. Jakob, V. V. Temnov, M. Münzenberg, M. Wolf, M. Kläui, and T. Kampfrath, "Terahertz spectroscopy for all-optical spintronic characterization of the spin-Hall-effect metals Pt, W and Cu80Ir20," *Journal of Physics D: Applied Physics*, vol. 51, no. 36, 2018.

[165] H. Jin, S. R. Boona, Z. Yang, R. C. Myers, and J. P. Heremans, "Effect of the magnon dispersion on the longitudinal spin Seebeck effect in yttrium iron garnets," *Physical Review B - Condensed Matter and Materials Physics*, vol. 92, no. 5, pp. 1–8, 2015.

[166] E. G. Tveten, A. Brataas, and Y. Tserkovnyak, "Electron-magnon scattering in magnetic heterostructures far out of equilibrium," *Physical Review B - Condensed Matter and Materials Physics*, vol. 92, no. 18, pp. 1–5, 2015.

[167] S. A. Bender and Y. Tserkovnyak, "Interfacial spin and heat transfer between metals and magnetic insulators," *Physical Review B - Condensed Matter and Materials Physics*, vol. 91, no. 14, pp. 1–5, 2015.

[168] S. Anisimov, B. Kapeliovich, and T. Perel'Man, "Electron emission from metal surfaces exposed to ultrashort laser pulses," *Soviet Journal of Experimental and Theoretical Physics*, vol. 39, pp. 776–781, 1974.

[169] C. Kittel, "Introduction to Solid State Physics, 8th edition," 2004.

[170] Y. J. Wu, Y. Gao, and X. M. Chen, "Dielectric relaxations of yttrium iron garnet ceramics over a broad temperature range," *Applied Physics Letters*, vol. 91, no. 9, pp. 1–4, 2007.

[171] E. Sagasta, Y. Omori, M. Isasa, M. Gradhand, L. E. Hueso, Y. Niimi, Y. Otani, and F. Casanova, "Tuning the spin Hall effect of Pt from the moderately dirty to the superclean regime," *Physical Review B*, vol. 94, no. 6, p. 060412(R), 2016.

[172] Y. M. Lu, Y. Choi, C. M. Ortega, X. M. Cheng, J. W. Cai, S. Y. Huang, L. Sun, and C. L. Chien, "Pt magnetic polarization on Y3Fe5O12 and magnetotransport characteristics," *Physical Review Letters*, vol. 110, no. 14, pp. 1–5, 2013.

[173] J. Lindner, C. Rudt, E. Kosubek, P. Poulopoulos, K. Baberschke, P. Blomquist, R. Wappling, and D. L. Mills, "T3/2 Dependence of the Interlayer Exchange Coupling in Ferromagnetic Multilayers," *Physical Review Letters*, vol. 88, no. 16, p. 167206, 2002.

[174] R. V. Pisarev, B. B. Krichevtsov, V. N. Gridnev, V. P. Klin, D. Frohlich, and C. Pahlke-Lerch, "Optical second-harmonic generation in magnetic garnet thin films," *Journal of Physics: Condensed Matter*, vol. 5, no. 45, pp. 8621–8628, 1993.

[175] K. W. Lin, M. Mirza, C. Shueh, H. R. Huang, H. F. Hsu, and J. V. Lierop, "Tailoring interfacial exchange coupling with low-energy ion beam bombardment: Tuning the interface roughness," *Applied Physics Letters*, vol. 100, no. 12, 2012.

[176] N. S. Almeida, D. L. Mills, and M. Teitelman, "Temperature variation of the interfilm exchange in magnetic multilayers: The influence of spin wave interactions," *Physical Review Letters*, vol. 75, no. 4, pp. 733–736, 1995.

[177] Y. Ohnuma, H. Adachi, E. Saitoh, and S. Maekawa, "Spin Seebeck effect in antiferromagnets and compensated ferrimagnets," *Physical Review B - Condensed Matter and Materials Physics*, vol. 87, no. 1, pp. 1–7, 2013.

[178] S. Geprägs, A. Kehlberger, F. D. Coletta, Z. Qiu, E. J. Guo, T. Schulz, C. Mix, S. Meyer, A. Kamra, M. Althammer, H. Huebl, G. Jakob, Y. Ohnuma, H. Adachi, J. Barker, S. Maekawa, G. E. Bauer, E. Saitoh, R. Gross, S. T. Goennenwein, and M. Kläui, "Origin of the spin Seebeck effect in compensated ferrimagnets," *Nature Communications*, vol. 7, no. May 2015, pp. 1–6, 2016.

[179] S. M. Wu, J. E. Pearson, and A. Bhattacharya, "Paramagnetic spin Seebeck effect," *Physical Review Letters*, vol. 114, no. 18, pp. 1–5, 2015.

[180] S. Seki, T. Ideue, M. Kubota, Y. Kozuka, R. Takagi, M. Nakamura, Y. Kaneko, M. Kawasaki, and Y. Tokura, "Thermal Generation of Spin Current in an Antiferromagnet," *Physical Review Letters*, vol. 115, no. 26, p. 266601, 2015.

[181] S. M. Wu, W. Zhang, A. Kc, P. Borisov, J. E. Pearson, J. S. Jiang, D. Lederman, A. Hoffmann, and A. Bhattacharya, "Antiferromagnetic Spin Seebeck Effect," *Physical Review Letters*, vol. 116, no. 9, p. 097204, 2016.

[182] J. Li, Z. Shi, V. H. Ortiz, M. Aldosary, C. Chen, V. Aji, P. Wei, and J. Shi, "Spin Seebeck Effect from Antiferromagnetic Magnons and Critical Spin Fluctuations in Epitaxial FeF2 Films," *Physical Review Letters*, vol. 122, no. 21, p. 217204, 2019.

[183] Y. Yamamoto, M. Ichioka, and H. Adachi, "Spin Seebeck effect in paramagnets and antiferromagnets at elevated temperatures," *Physical Review B*, vol. 100, no. 6, p. 064409, 2019.

[184] K. Hirakawa, T. Hashimoto, and K. Hirakawa, "Magnetic Properties of Potassium Iron Group Fluorides KMF3," *Journal of the Physical Society of Japan*, vol. 15, no. 11, pp. 2063–2068, 1960.

[185] A. Okazaki and Y. Suemune, "The Crystal Structures of KMnF 3 , KFeF 3 , KCoF 3 , KNiF 3 and KCuF 3 above and below their Néel Temperatures," *Journal of the Physical Society of Japan*, vol. 16, no. 4, pp. 671–675, 1961.

[186] M. Safa and B. K. Tanner, "Antiferromagnetic domain wall motion in KNiF3 and KCoF3 observed by X-ray synchrotron topography," *Philosophical Magazine Part B*, vol. 37, no. 6, pp. 739–750, 1978.

[187] T. Tsuda, H. Yasuoka, and T. Miyauchi, "Magnetic Susceptibility of an Antiferromagnetic KCoF3Single Crystal—19F NMR and Static Measurements," *Journal of the Physical Society of Japan*, vol. 45, no. 5, pp. 1551–1558, 1978.

[188] D. Bossini, A. M. Kalashnikova, R. V. Pisarev, T. Rasing, and A. V. Kimel, "Controlling coherent and incoherent spin dynamics by steering the photoinduced energy flow," *Physical Review B - Condensed Matter and Materials Physics*, vol. 89, no. 6, p. 060405(R), 2014.

[189] B. Krichevtsov, P. Markovin, S. Petrov, and R. Pisarev, "Isotropic and anisotropic magnetic refraction of light in the antiferromagnets KNiF3 and RbMnF3," *Zh. Eksp. Teor. Fiz*, vol. 86, no. December 1983, pp. 2262–2272, 1984.

[190] M. P. M. Balkanski, "Infrared Lattice Vibrations of KNiF 3 from Reflection Date at 300 and 90 K," *The Journal of Chemical Physics*, vol. 46, no. 1621, 1967.

[191] W. Lin, K. Chen, S. Zhang, and C. L. Chien, "Enhancement of Thermally In-jected Spin Current through an Antiferromagnetic Insulator," *Physical Review Letters*, vol. 116, no. 18, p. 186601, 2016.

[192] A. Prakash, J. Brangham, F. Yang, and J. P. Heremans, "Spin Seebeck effect through antiferromagnetic NiO," *Physical Review B*, vol. 94, no. 1, pp. 1–5, 2016.

[193] Z. Qiu, J. Li, D. Hou, E. Arenholz, A. T. N'Diaye, A. Tan, K. I. Uchida, K. Sato, S. Okamoto, Y. Tserkovnyak, Z. Q. Qiu, and E. Saitoh, "Spin-current probe for phase transition in an insulator," *Nature Communications*, vol. 7, no. May, p. 12670, 2016.

[194] W. Zhang, M. B. Jungfleisch, W. Jiang, J. E. Pearson, A. Hoffmann, F. Freimuth, and Y. Mokrousov, "Spin hall effects in metallic antiferromag-nets," *Physical Review Letters*, vol. 113, no. 19, p. 196602, 2014.

[195] L. Frangou, S. Oyarzún, S. Auffret, L. Vila, S. Gambarelli, and V. Baltz, "Enhanced Spin Pumping Efficiency in Antiferromagnetic IrMn Thin Films around the Magnetic Phase Transition," *Physical Review Letters*, vol. 116, no. 7, pp. 1–5, 2016.

[196] J. C. Rojas-Sánchez, N. Reyren, P. Laczkowski, W. Savero, J. P. Attané, C. Deranlot, M. Jamet, J. M. George, L. Vila, and H. Jaffrès, "Spin pumping and inverse spin hall effect in platinum: The essential role of spin-memory loss at metallic interfaces," *Physical Review Letters*, vol. 112, no. 10, pp. 1–5, 2014.

[197] M. Haertinger, C. H. Back, J. Lotze, M. Weiler, S. Geprägs, H. Huebl, S. T. Goennenwein, and G. Woltersdorf, "Spin pumping in YIG/Pt bilayers as a function of layer thickness," *Physical Review B - Condensed Matter and Materials Physics*, vol. 92, no. 5, pp. 1–6, 2015.

[198] S. Emori, A. Matyushov, H. M. Jeon, C. J. Babroski, T. Nan, A. M. Belkessam, J. G. Jones, M. E. McConney, G. J. Brown, B. M. Howe, and N. X. Sun, "Spin-orbit torque and spin pumping in YIG/Pt with interfacial insertion layers," *Applied Physics Letters*, vol. 112, no. 18, 2018.

[199] H. Yamaguchi, K. Katsumata, M. Hagiwara, M. Tokunaga, H. Liu, a. Zibold, D. Tanner, and Y. Wang, "Antiferromagnetic resonance in the cubic perovskite KNiF3," *Physical Review B*, vol. 59, no. 9, pp. 6021–6023, 1999.

[200] N. Suzuki and Y. Takaoka, "A mechanism of magnon-phonon interaction in KCoF3," *Solid State Communications*, vol. 21, no. 4, pp. 365–370, 1977.

[201] N. Erum and M. Azhar Iqbal, "Mechanical and magneto-opto-electronic investigation of transition metal based fluoro-perovskites: An ab-initio DFT study," *Solid State Communications*, vol. 264, no. June, pp. 39–48, 2017.

[202] R. M. Dubrovin, N. V. Siverin, P. P. Syrnikov, N. N. Novikova, K. N. Boldyrev, and R. V. Pisarev, "Lattice dynamics and microscopic mechanisms of the spontaneous magnetodielectric effect in the antiferromagnetic fluoroperovskites KCoF3 and RbCoF3," *Physical Review B*, vol. 100, no. 2, pp. 1–10, 2019.

[203] H. Takeuchi, N. Suzuki, and K. Motizuki, "Study of Magnetic Properties of KCoF3 by Dynamical Correlated Effective Field Approximation," *Journal of the Physical Society of Japan*, vol. 49, no. 4, pp. 1283–1290, 1980.

[204] D. M. Juraschek, P. Narang, and N. A. Spaldin, "Phono-magnetic analogs to opto-magnetic effects," no. 0, pp. 1–10, 2019.

[205] H. Jiao and G. E. W. Bauer, "Spin backflow and ac voltage generation by spin pumping and the inverse spin hall effect," *Physical Review Letters*, vol. 110, no. 21, pp. 1–5, 2013.

[206] J. A. Barreda-Argüeso, F. Aguado, J. González, R. Valiente, L. Nataf, M. N. Sanz-Ortiz, and F. Rodríguez, "Crystal-Field Theory Validity Through Local (and Bulk) Compressibilities in CoF2 and KCoF3," *Journal of Physical Chemistry C*, vol. 120, no. 33, pp. 18788–18793, 2016.

[207] S. Casalbuoni, H. Schlarb, B. Schmidt, P. Schmüser, B. Steffen, and A. Winter, "Numerical studies on the electro-optic detection of femtosecond electron bunches," *Physical Review Special Topics - Accelerators and Beams*, vol. 11, no. 7, pp. 1–18, 2008.

[208] T. Löffler, T. Hahn, M. Thomson, F. Jacob, and H. G. Roskos, "Large-area electro-optic ZnTe terahertz emitters," *Optics Express*, vol. 13, no. 14, p. 5353, 2005.

[209] F. Blanchard, L. Razzari, H. Bandulet, G. Sharma, R. Morandotti, J. C. Kieffer, T. Ozaki, M. Reid, H. F. Tiedje, H. K. Haugen, and F. A. Hegmann, "Generation of 1.5 uJ single-cycle terahertz pulses by optical rectification from a large aperture ZnTe crystal," *Optics Express*, vol. 15, no. 20, p. 13212, 2007.

[210] G. Li, R. V. Mikhaylovskiy, K. A. Grishunin, J. D. Costa, T. Rasing, and A. V. Kimel, "Laser induced THz emission from femtosecond photocurrents in Co/ZnO/Pt and Co/Cu/Pt multilayers," *Journal of Physics D: Applied Physics*, vol. 51, no. 13, 2018.

[211] D. Yang, J. Liang, C. Zhou, L. Sun, R. Zheng, S. Luo, Y. Wu, and J. Qi, "Powerful and Tunable THz Emitters Based on the Fe/Pt Magnetic Heterostructure," *Advanced Optical Materials*, vol. 4, no. 12, pp. 1944–1949, 2016.